Benthic Habitat Mapping and Bio-Optical Characterization La Parguera Marine Reserve using Passive and Active Remote Sensing Data

by

William J Hernández-López

A dissertation submitted in partial fulfillment of the requirements for the degree of
DOCTOR OF PHILOSOPHY
in
MARINE SCIENCES
(Biological Oceanography)

UNIVERSITY OF PUERTO RICO
MAYAGÜEZ CAMPUS
2015

Approved by:

_____	_____
Fernando Gilbes Santaella, PhD Member, Graduate Committee	Date
_____	_____
Jorge R. Garcia Sais, PhD Member, Graduate Committee	Date
_____	_____
Roy A. Armstrong, PhD President, Graduate Committee	Date
_____	_____
Pablo Clemente-Colón, PhD Member, Graduate Committee	Date
_____	_____
Ernesto Otero, PhD Chairperson of the Department	Date
_____	_____
Kurt A. Grove, PhD Representative of Graduate Studies	Date

Abstract

Remote sensing techniques are widely useful in the field of oceanography and provide a better understanding of the dynamics of ocean circulation, in monitoring climate change, for navigation and fisheries management, and also help to improve models for weather and climate predictions. Also, information from satellites and airborne sensors can be used to evaluate constituents of natural waters, their optical properties, bottom depth and type, and classification of benthic features in shallow coastal environments. This study addressed the combined used of imagery from passive and active sensors, and field optical data, in an algorithm development for bio-optical characterization and benthic habitat mapping in La Parguera Marine Reserve. High-resolution bathymetry from passive sensors was obtained from a Worldview 2 (WV2) image at a significant spatial resolution (4 meters) and was validated using bathymetric data from an active sensor (LiDAR). An additional analysis was done that evaluated the influence of atmospheric corrections in depth retrievals. The Cloud Shadow Approach (CSA), using a simple band ratio (Band2/Band3) provided the best atmospheric correction with a second order polynomial equation (r^2 = 0.82). This WV2 depth model was evaluated at another site within the image where it successfully retrieved depth values (r^2 = 0.90) proving that high-resolution bathymetry can be obtained when combined with a robust atmospheric correction, even in areas with variable bottom composition. The Airborne Visible Infrared Image Spectrometer (AVIRIS) and WorldView-2 (WV2) sensors were used to derive water optical properties, combined with water depth from LiDAR data to perform a water column correction using Lee's semi-analytical algorithm, and to determine the optical bottom albedo. The values of image-derived absorption (p=0.05, r^2=0.90) and Kd (p=0.05, r^2=0.96) exhibited a strong correlation when compared with *in situ* values. A strong inverse relationship was found between distance from shore to increasing

values of absorption ($p=0.07$, $r^2=0.71$) and this factor explained about 71% of the variation in absorption values for the time-series. For the AVIRIS image, bottom albedo values for sand, seagrass, and coral-gorgonians were in good agreement with *in situ* values for these substrates in both spectral shape and intensity, spectral absorption and reflectance features were only present after the water column correction. LiDAR reflectivity was highly correlated to bottom albedo images from AVIRIS ($r^2 = 0.79$) and WV2 ($r^2 = 0.79$), and this correlation was further improved by removing the depth influence from the LiDAR reflectivity (AVIRIS, $r^2 = 0.95$; WV2, ($r^2 = 0.94$). High-resolution benthic habitat maps were created from AVIRIS and WV2 modeled bottom albedo products from pre-processed imagery (atmospheric and water column corrected) for La Parguera Reserve. An ISODATA classification was performed and the segmented images were classified as coral reefs, seagrass, hardbottom, mixed sand/hardbottom/coral, mud, sand, and sand with benthic algae. The overall accuracy (AVIRIS = 63.55%, WV2 = 64.81%), kappa coefficient (AVIRIS = 55 %, WV2 = 57%), and the tau coefficient (AVIRIS = 59%, WV2 = 60%) were evaluated. No major class differences were found between the AVIRIS and WV2 classification totals, except for coral reefs and sand, where the reduction in coral reefs class totals could be attributed to temporal differences in the images depicting changes in the coral reefs distribution within the reserve. A major contribution of this study was the creation of the first benthic habitat map for La Parguera Reserve that: 1) provided multi/hyperspectral information at this spatial scale (4 square meters), 2) covered the extent of the reserve, and 3) provided a baseline for future development of benthic habitat studies using an objective classification scheme.

Resumen

La información obtenida de sensores colocados sobre satélites y aviones es utilizada en la oceanografía para mejorar la navegación, y el conocimiento sobre la circulación oceánica que redunda en una mejoría a los modelos climatológicos. Estas técnicas de teledetección también nos permiten evaluar los componentes de la columna de agua, las propiedades ópticas, la profundidad y el tipo de fondo, y la clasificación de habitáculos bénticos. Este estudio se enfoca en la fusión de sensores activos y pasivos, datos ópticos de campo, y el desarrollo de algoritmos para la caracterización bio-óptica de las aguas y el tipo de fondo de la Reserva Natural de la Parguera. La imagen del sensor Worldview 2 (WV2) nos permitió obtener un mapa batimétrico a alta resolución que fue validad a su vez con los datos obtenidos de un sensor activo (LiDAR). La aplicación de diferentes modelos de corrección atmosférica nos permitió evaluar cómo afecta esta corrección la derivación de profundidad, donde usando una razón de bandas (Banda 1/Banda 3) con la corrección de "Cloud Shadow Approach" (CSA) pudimos obtener una excelente correlación (r^2 = 0.82). Este modelo fue utilizado en otra sección de la imagen donde se obtuvieron valores de profundidad validados (r^2 = 0.90) lo que indica que aun en zonas de habitáculos profundos y variables, se pueden obtener excelentes resultados seleccionando la mejor corrección atmosférica. Los sensores AVIRIS y WV2 fueron utilizados para corregir la influencia de la columna de agua, basados en la derivación de las propiedades ópticas y valores de profundidad de LiDAR. Esta corrección de columna de agua fue basado en los algoritmos semi-analíticos de Lee y nos permitió determinar el albedo de fondo. Los valores de absorción ($p=0.05$, $r^2=0.90$) y Kd ($p=0.05$, $r^2=0.96$) derivados de imágenes mostraron una excelente correlación con los valores de campo. El factor de distancia de la costa mostro una fuerte relación inversa con los valores de absorción ($p=0.07$, $r^2=0.71$) para la serie de tiempo evaluada.

Los rasgos espectrales de arena, yerbas marinas y corales (gorgóneos) solo fueron observados una vez se eliminó la influencia de la columna de agua en la señal, y sus valores de albedo de fondo fueron muy similares a los medidos *in situ* para esto sustratos. La correlación entre albedo de fondo y reflectividad de LiDAR (AVIRIS, r^2 = 0.79; WV2, r^2 = 0.79) fueron mejorados significativamente después de haber removido la influencia de profundidad (AVIRIS, r^2 = 0.95; WV2, (r^2 = 0.94). Se desarrollaron mapas de hábitats bénticos de alta resolución de los productos de albedo de fondo de las imágenes de AVIRIS y WV2 donde la técnica de ISODATA fue utilizada en las imágenes segmentadas para clasificar entre: arrecifes de coral, fondo duro "hardbottom", mezcla de arena/ fondo duro "hardbottom"/coral, fango, arena, y área con algas bénticas. Los valores de certeza "overall accuracy" (AVIRIS = 63.55%, WV2 = 64.81%), coeficiente kappa (AVIRIS = 55 %, WV2 = 57%), y coeficiente tau (AVIRIS = 59%, WV2 = 60%) fueron evaluados y no se encontró diferencia significativa entre la clasificación de AVIRIS y WV2, excepto en la clases de arrecifes de coral y arena. Esta reducción en la clase de arrecifes de coral se puede atribuir a las diferencia temporales de las imágenes donde se presentan los cambios de este tipo de fondo en la reserva. Una contribución significativa de este estudio fue el desarrollo un mapa béntico para la Reserva de la Parguera donde: se pudo obtener información multi/hiper espectral a una escala significativa (4 metros), que cubriera la extensión total de la reserva, y que proveyera una base objetiva de clasificación para futuros estudios bénticos de la reserva.

COPYRIGHT

In presenting this dissertation in partial fulfillment of the requirements for a Doctor of Philosophy degree at the University of Puerto Rico, I agree that the library shall make its copies freely available for inspection. I therefore authorize the Library of the University of Puerto Rico at Mayaguez to copy my dissertation totally or partially. Each copy must include the title page. I further agree that extensive copying of this dissertation is allowable only for scholarly purposes. It is understood, however, that any copying or publication of this dissertation for commercial purposes, or for financial gain, shall not be allowed without my written permission.

Dedication

To my Family; Iris, Joel David and Luis Antonio

Acknowledgements

My heart is with my family and extended family for their unconditional love and support, especially my father, mother and brothers; these are also you're achievements.

I would like to thank my graduate committee, Dr. Roy A. Armstrong, for his guidance in balancing graduate studies with a professional life, Dr. Fernando Gilbes for his important suggestions throughout my career, Dr. Jorge Garcia and Dr. Pablo Clemente-Colon for their comments and support. Special thanks to the Bio-Optical Oceanography Lab team, past and current members, Dr. Yasmin Detrés, María, Myrna, Suhey, Mariana for their contributions and "life at the lab". A special thanks to Belitza Brocco for her field work and solving the "mysteries" of the bio-optical package. My gratitude goes to the faculty and personnel of the Department of Marine Sciences for their support, especially Mr. Luis Lugo "Vitamina" for his insightful ideas on solving many problems along the way.

My doctoral studies were made possible by the NOAA Cooperative Remote Sensing Science and Technology Center (CREST) program under grant number NA06OAR480162. Special thanks to Dr. Liane Guild (NASA) for the AVIRIS imagery and Digital Globe for the WV2 imagery.

TABLE OF CONTENTS

LIST OF TABLES

LIST OF FIGURES

Pages

1 GENERAL INTRODUCTION

2 HIGH-RESOLUTION BATHYMETRY FROM PASSIVE SENSORS

3 HIGH RESOLUTION BOTTOM ALBEDO AND WATER OPTICAL CHARACTERIZATION OF LA PARGUERA RESERVE FROM ACTIVE AND PASSIVE SENSORS

LIST OF ACRONYMS AND ABBREVIATIONS

AOPs: Apparent Optical Properties
AVIRIS: Airborne Visible/InfraRed Imaging Spectrometer
CASI: Compact Airborne Spectrographic Imager
CSA: Cloud shadow approach
DNs: Digital Numbers
EMR: Electromagnetic Radiation
ENVI: Environment for Visualizing Images
ESRI: Environmental Systems Research Institute
FLAASH: Fast Line-of-Sight Atmospheric Analysis of Spectral Hypercubes
FWHM: Full Width Half Maximum
GOES: Geostationary Operational Environmental Satellite
HSI: Hyperspectral Imagery
IDL: Interactive Data Language
IOPs: Inherent Optical Properties
IR: Infrared
ISODATA: Iterative Self-Organizing Data Analysis Technique
LiDAR: Light Detection And Ranging
MLLW: Mean Lower Low Water
MS: Multispectral
MSI: Multispectral Imagery/Imaging
MPA: Marine Protected Areas
NIR: Near Infrared
NGO: Non-Government Organizations
NOAA: National Oceanic and Atmospheric Administration
PHILLS: Portable Hyperspectral Imager for Low-Light
RMS: Root Mean Square
ROIs: Regions of Interest
Rrs: Remote Sensing Reflectance
SHOALS: Scanning Hydrographic Operational Airborne Lidar Survey
SONAR: SOund Detection And Ranging
SPOT: French: *Satellite Pour l'Observation de la Terre*
SWIR: Shortwave Infrared
TAFKAA: The Algorithm Formerly Known As ATREM
TVU Total Vertical Uncertainty ()
USGS: United States Geological Survey
UTM: Universal Transverse Mercator
UV: Ultraviolet light
VIS: Visible light
WGS-84: World Geodetic System 1984
WV2: WorldView-2

Chapter 1: General Introduction

The coral ecosystems around the world, including those in the United States and the Caribbean are reported to be in decline. Recent broad scale studies indicate that U.S. coral ecosystems have shown dramatic declines of live coral cover during the past three decades, especially those both close to land and in water less than 18 meters deep (Garcia-Sais et al. 2008; Gardner et al. 2003; Menza et al. 2008). These ecosystems are detrimentally affected by human-based and natural factors associated with over-fishing, diseases, bleaching, climate change, urban and tourism-related coastal development, sedimentation, toxic chemical pollution, ship-groundings (Rohmann et al. 2005; Gardner et al. 2003), many of which are expected to be exacerbated by population growth and global warming in the future (Hoegh-Guldberg et al. 2007 and 1999). Puerto Rico and the US Virgin Islands (USVI) have suffered the effects of these stressors on the coral reef ecosystems. The majority of coral reefs around Puerto Rico, along with many other Caribbean reefs are among the most vulnerable in the world because of strong anthropogenic impacts in the area (Warne et al. 2005). A 2005 coral bleaching event and post-bleaching coral mass mortality during 2006 had a dramatic impact on Puerto Rican coral habitats (Garcia-Sais et al. 2005).

The use of marine protected areas (MPAs) for mitigation against adverse effects of overfishing and other anthropogenic impacts is a recent alternative explored by many universities, research centers, government agencies, and non-government organizations (NGO) and represents an innovation for confronting a previous lack of conservation measures (Aguilar-Perera et al. 2006). La Parguera Natural Reserve is a marine protected area located in the southwest coast of Puerto Rico. The reserve encompasses an area of approximately 5,260.91 hectares (13,000 acres), which extends from east to west from Punta Jorobado in Guánica to the Punta Pitahaya in Cabo Rojo and 5.56 kilometers (3 nautical miles) from the coast (Figure 1). The reserve was established in

1979 by the Department of Natural and Environmental Resources of Puerto Rico because of its important marine resources that include coral reefs, seagrass beds, mangrove forest and bioluminescent bays. Its high biodiversity and fisheries potential makes it and important ecological system unique in Puerto Rico.

Remote sensing is primarily concerned with collecting and interpreting information about an object or landscape from a remote vantage point (Purkis and Klemas 2011). Imagery data acquired from satellites are widely useful in the field of oceanography and provide a better understanding of the dynamics of ocean circulation, in monitoring climate change, for navigation and fisheries management, and also help to improve models for weather and climate predictions (Sanford et al. 2011). A more pertinent definition to our study is that of optical remote sensing, which is the use of optical measurements made from aircraft or satellites to obtain information about the constituents of natural waters, their optical properties, or the bottom depth and type (Mobley 2011). Optical remote sensing is also a valuable tool for classification of benthic features in shallow coastal environments. The sensors used can be classified as active or passive. Passive remote sensing utilizes the light that is naturally emitted or reflected by the water body. The most common example of passive remote sensing is the use of sunlight that has been backscattered within the water and returned to the sensor. Active remote sensing means that a signal of known characteristics is sent from the sensor platform--an aircraft or satellite--to the ocean, and the return signal is then detected after a time delay determined by the distance from the platform to the ocean and by the speed of light (Gao 2009).

Optical remote sensing is an important tool utilized for monitoring marine environments. Light interacts with seawater that contains dissolved and particulate matter, with varying

concentrations (both spatially and temporally) throughout the water column (Mobley et al. 1993). As photons travel through water, they interact through scattering and absorption processes with the particles in the water and with the water molecules themselves (Jerlov 1976). To provide a better understating of these interactions, the optical properties of the water column can be divided into two classes: inherent optical properties (IOPs) and apparent optical properties (AOPs) (Preisendorfer 1976). The IOPs depend only upon the medium and are independent of the light field; so as light enters and interacts with the medium it is altered by scattering and absorption (Morel 1974; Smith and Baker 1981). These properties are the absorption coefficient (a), scattering coefficient (b), and the beam attenuation coefficient (c). The AOPs are dependent on both the medium and the directional structure of the light field (Kirk 1984; Mobley et al. 1993). The vertical attenuation coefficient for downward irradiance (K_d) and the irradiance reflectance ($R = E_u/E_d$), are AOPs and their values depend on the composition of water (IOP) and vary to some extent by depth and with solar altitude. Since the AOPs are dependent on the IOPs, knowledge of this relationship is important in determining the optical properties of water (Kirk 1984) and in the interpretation of the radiometric signals over shallow waters from satellite and airborne sensors (Maritorena, et al. 1994). The use of radiances measured from optical sensors allows the analytical or semi-analytical retrieval of shallow-water bathymetry, bottom albedo and optical properties of the water column, and the contribution of each component to the remotely sensed signal (Lee et al. 1999).

Information about shallow water bathymetry is beneficial to scientific research and other activities that require knowledge of ocean depths in a particular coastal location. While most of the research using these optical remote sensed signals has been focused on ocean color research

and obtaining accurate depths, the methods developed has also been applied to determining benthic habitat types. All mapping that uses airborne or satellite remote sensing must account for atmospheric effects; however the biggest challenge for mapping the benthic environment is still removing the attenuation effects of the water column (Collin and Hench 2012).

Several approaches and methods of benthic mapping have been attempted, including using band ratios (Polcyn, et al., 1970; Stumpf, et al., 2003), radiative transfer models (Bierwirth et al. 1993; Philpot 1989; Lyzenga 1978), neural networks (Sandidge and Holyer 1998), and look-up tables (Mobley 2003). Again, while these published methods were primarily focused on obtaining depths, they also provided information on benthic classification. More recently new techniques using inversion and optimization of quasi-analytical or semi-analytical algorithms have been used with hyperspectral imagery to determine water properties and/or depth (Albert and Gege 2006; Brando and Dekker 2003; Morel and Maritorena 2001; Lee et al. 2001 and 1999). The semi-analytical model produced by Lee et al. (1999), has produced significant and accurate results of many constituent concentrations along with depth (Brando et al. 2009).

Advancements in surveying technologies have increased the accuracy of large-scale mapping projects in shallow-water marine environments. Mapping marine habitats and associated species distributions is fundamental in determining the potential for protection, assisting in resource management and assessing anthropogenic impacts. For example, the knowledge of benthic habitats and their spatial distribution is vital for understanding complex coral reefs systems. Benthic habitat maps are important for assessing patterns, identifying area of habitat diversity and determining habitat coverage. The purpose of this study is to develop a high-resolution

benthic habitat map for La Parguera Reserve to provide detailed information on the areal cover and spatial patterns of benthic communities using data fusion from passive and active sensors.

Study Area:

La Parguera Natural Reserve is a marine protected area located in the southwest coast of Puerto Rico and it extends from Punta Pitahaya in the west to Punta Jorobado in the east and from the coastline to the shelf edge (Figure 1). The area of La Parguera is recognized for the exceptional value of its marine resources, which include and extensive coral reef ecosystem, seagrass beds, coastal mangrove fringe and mangroves islands, and two bioluminescent bays (UNESCO 1998).

This section of the insular shelf of La Parguera shelf is a bedrock surface composed primarily of karst, where the limestone surface has been modified by reef growth and sediment deposition since the last glacial low stand (Morelock 1994). A karst surface developed more than 10,000 years ago, when sea level was lower and the limestone surface of the Parguera shelf was exposed to sub aerial erosion (Morelock et al. 1994). The modern bathymetry and sediment patterns are different from east to west along the Parguera insular shelf (Morelock et al. 1977). The shelf is also characterized by an irregular and complex physiography, with submerged patch reefs extending from 1 to 9 meters off the bottom, an emergent reef with a characteristic reef crest, and a well-developed coral reef formation at the border of the shelf (Morelock et al. 1977). The lack of significant rainfall and large rivers in the south-southwest coast, combined with the oligotrophic waters of the northern Caribbean contribute to the high levels of water transparency of the insular shelf and results in an optimization of growth rates and depth extent of coral reefs and seagrass (UNESCO 1998). The average annual rainfall at the Isla Magueyes Station in La

Parguera is 74.52 centimeters. The average water depth is 18-20 meters in the outer and middle shelf, while the shallow inner reef lagoon is less than 6 meter deep.

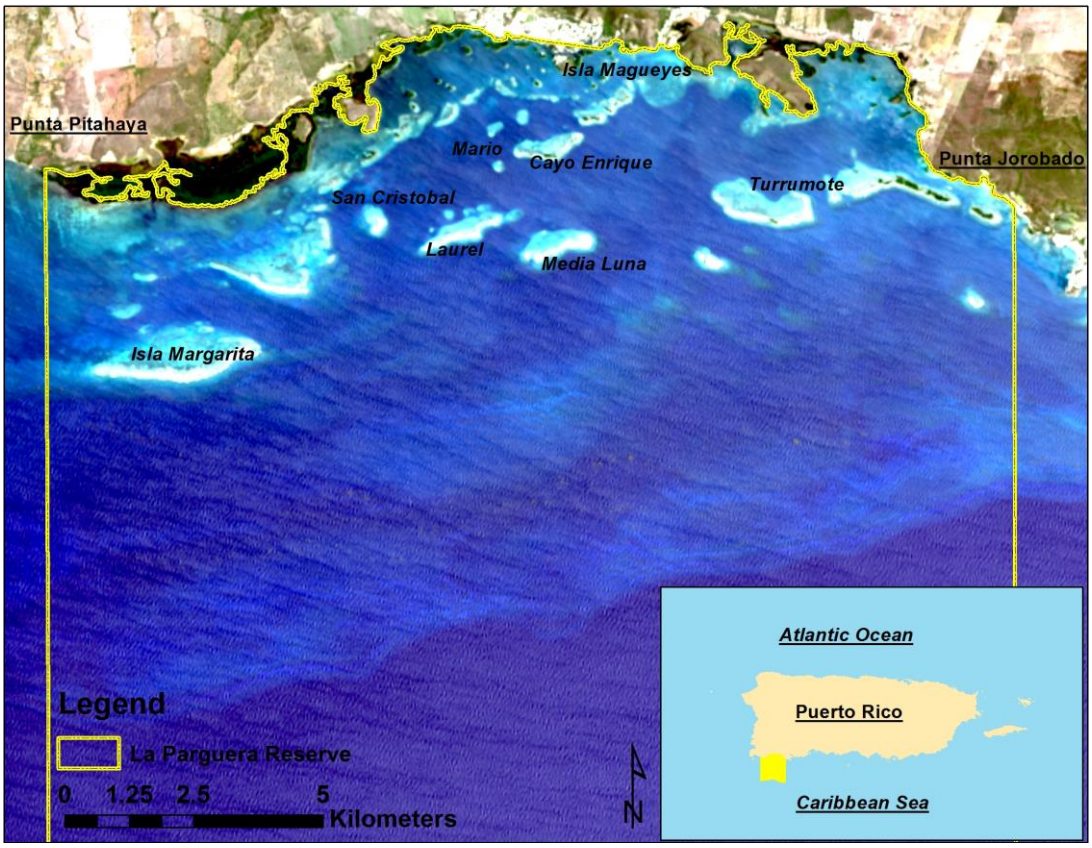

Figure 1: Study area of La Parguera Reserve, southwestern Puerto Rico.

Description of Data sources

AVIRIS image

The Airborne Visible Infrared Imaging Spectrometer (AVIRIS) is a hyperspectral sensor that has 224 contiguous spectral bands from 380 to 2500 nm of which 32 bands are in the visible region (400-700 nm) with a spectral resolution of about 10 nm and a high (~1000:1) signal to noise ratio (Table 1). During December 12-13, 2005, AVIRIS was flown in a grid of overlapping solar azimuth lines over La Parguera aboard NASA's Twin Otter aircraft at an altitude of 3.5 kilometers producing a pixel size of approximately 3.1 meters (Armstrong et al. 2007) An image

was preprocessed for subsequent benthic analysis that included suppressing impacts of the stray-light anomaly, correction of an unexplained edge decay feature, suppression of sun glint and finally the application and atmospheric correction using "The Algorithm Formerly Known As ATREM (Atmospheric REMoval)" or TAFKAA (Lobitz et al. 2008). The final product was an AVIRIS remote sensing reflectance image (Rrs) with 32 bands ideal for studying shallow water environments and estimating water depth (Figure 2).

Table 1: AVIRIS sensor details

Band	Wavelength (nm)	Band	Wavelength (nm)	Band	Wavelength (nm)
1	405	**12**	511	**23**	617
2	414	**13**	520	**24**	626
3	424	**14**	530	**25**	636
4	434	**15**	539	**26**	646
5	443	**16**	549	**27**	655
6	453	**17**	559	**28**	665
7	462	**18**	568	**29**	672
8	472	**19**	578	**30**	682
9	482	**20**	588	**31**	692
10	491	**21**	597	**32**	701
11	501	**22**	607		

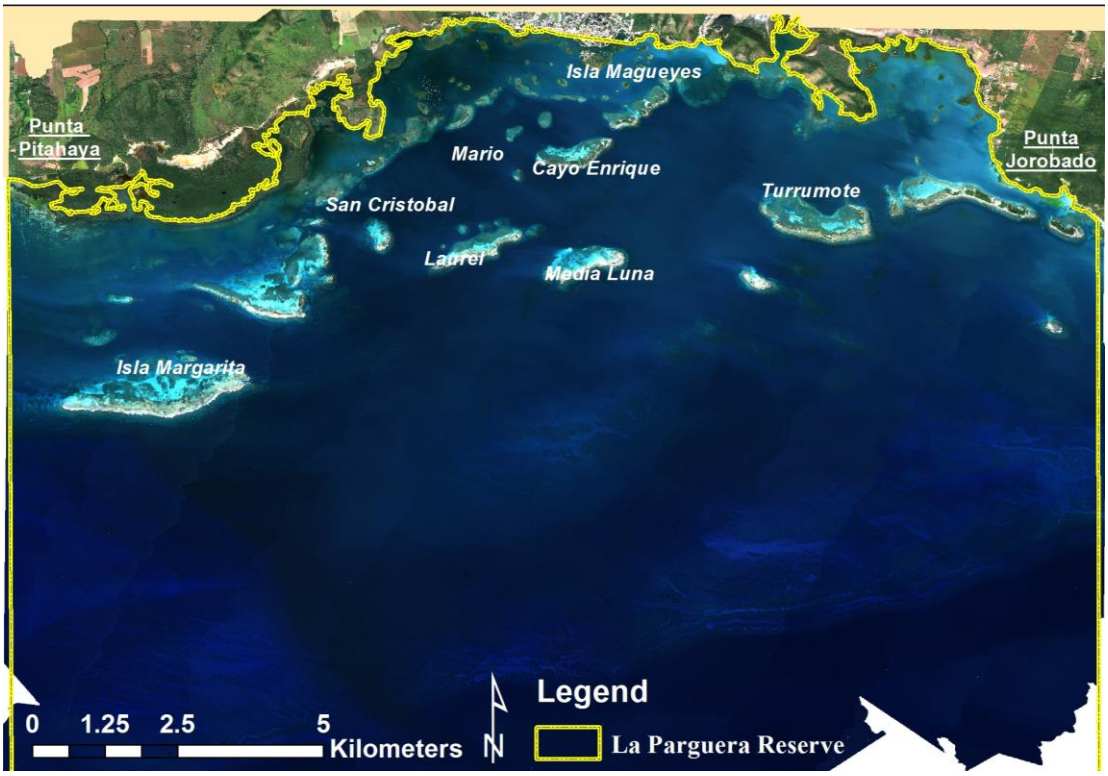

Figure 2: AVIRIS image of La Parguera Reserve.

LiDAR Bathymetric data

LiDAR (Light Detection and Ranging), also known as optical radar or laser radar, is an active remote sensing instrument that transmits high-power pulses of laser light at short intervals over an area and receives the signal reflected from a detected surface (Purkis and Klemas 2011). It has been used extensively for terrain models and application in urban and aquatic environments. In the case of LiDAR for bathymetry, the instrument uses a "green" laser that penetrates the water column to measure the distance from the surface of the water to the bottom (Purkis and Klemas 2011). Water depth is measured from the two-way travel time of a pulse between the water surface and the sea floor. After the surface-reflected and bottom-reflected pulses are identified, water depth is calculated from the time difference between the two pulses (Gao 2009).

LiDAR topographic and bathymetric data were acquired over La Parguera Reserve region between April and May 2006 (Figure 3) for coastal elevations of 50 m above sea level to 70 m water depths using a Laser Airborne Depth Sounder (LADS) Mk II Airborne System (Stephenson and Sinclair 2006). This airborne system uses a 900 Hz Nd: YAG (neodymium-doped yttrium aluminum garnet) laser, which is split by an optical coupler into an infrared (1064 nm) beam and a green (532 nm) beam. The final product (16-bit Geotiff image) produced a 4 x 4 meters bathymetry surface where the soundings were positioned relative to the NAD83 UTM 19 N horizontal coordinate system and to the Mean Lower Low Water (MLLW) vertical tidal coordinate system (Costa et al. 2009). According to Costa et al. (2009), the horizontal accuracy of the dataset is better than ±5 meters, and the vertical accuracy or maximum total vertical uncertainty (TVU) of the dataset is better than ±0.82 meters.

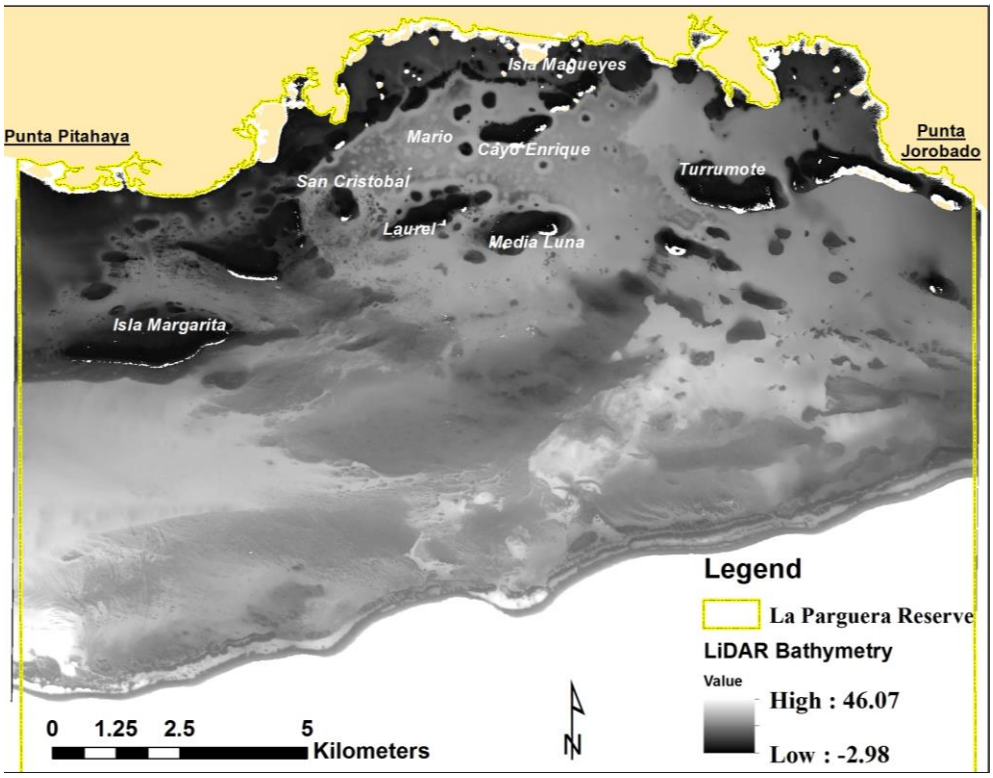

Figure 3: LiDAR bathymetry image, subset of La Parguera Reserve.

LiDAR Reflectivity data

Some of the most advanced LiDAR systems are calibrated to return a reflectance "image" of the seabed using a wavelength of (laser beam) 532 nanometers (Tuell et al. 2005). This intensity image can provide a mapping opportunity to characterize the seabed based on the reflectivity response of the substrate.

The LiDAR reflectivity data were also acquired for the southwest insular shelf of Puerto Rico between April and May 2006 using the LADS Mk II Airborne System (Figure 4). A single reflectivity value was calculated per pulse and the data was run through a Tenix LADS proprietary reflectivity algorithm and the resulting data was imported and gridded at 5 meters (Stephenson 2007). The relative reflectivity is a measure of the reflectance of the seabed in a single wavelength (green/blue, 532nm) and indicates variation in reflectivity across the survey area where bathymetry was acquired. The numerical values for the relative reflectivity are scaled logarithmically to an 8-bit integer range 0 – 255 (Stephenson and Sinclair 2006).

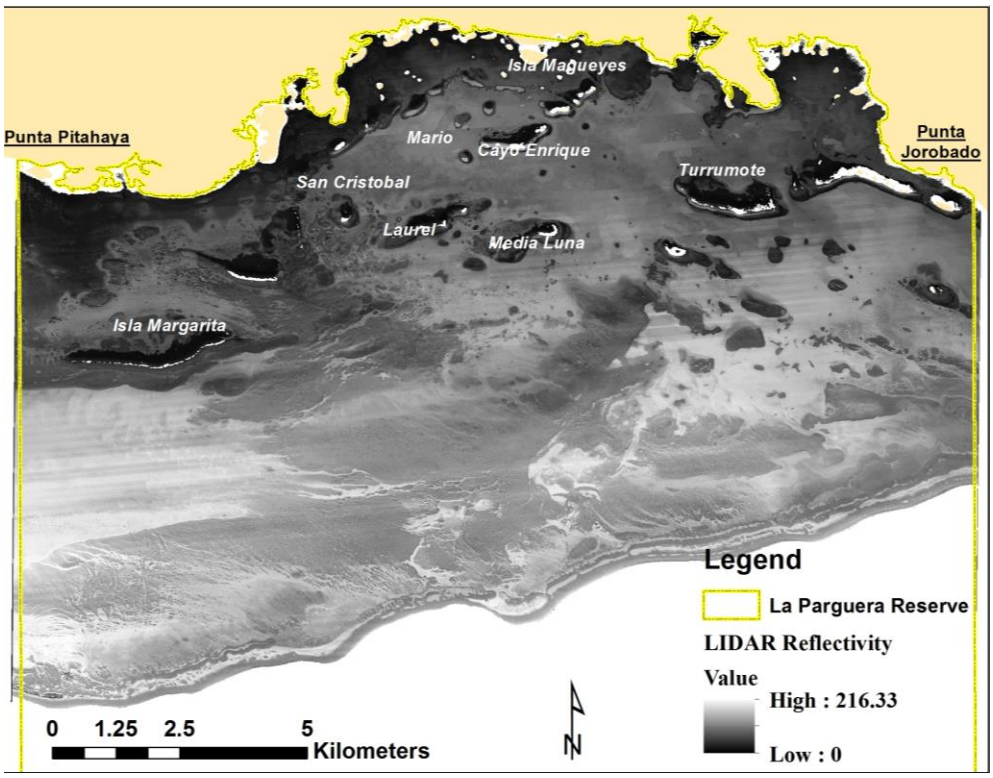

Figure 4: LiDAR reflectivity image, subset of La Parguera Reserve.

WorldView 2 Image

World View 2 (WV2) is the first high-resolution 8-band multispectral commercial satellite operating at an altitude of 770 kilometers with a spatial resolution at nadir of 46 cm in panchromatic mode and 1.84 meters in multispectral mode (Table 2) at nadir. This sensor can collect a 16.4 kilometer swath with 11-bit radiometric resolution. The importance of this sensor for oceanic studies is that it includes five bands in the visible region with a purple "coastal" band (FWHM, 425nm) that provides better water penetration capabilities.

Waveband Number	Wavebands Name	Wavelength (nm)	FWHM (nm)
1	Purple	400-450	425
2	Blue	450-510	480
3	Green	510-580	545
4	Yellow	585-625	605
5	Red	630-690	660
6	"Red Edge"	705-745	725
7	Near Infrared 1	770-895	832.5
8	Near Infrared 2	860-1040	950

Table 2: WorldView 2 sensor details

The image used in this study was acquired over La Parguera on December 4, 2011 (15:25 GMT) without apparent clouds nor "sun glint" present (Figure 5).

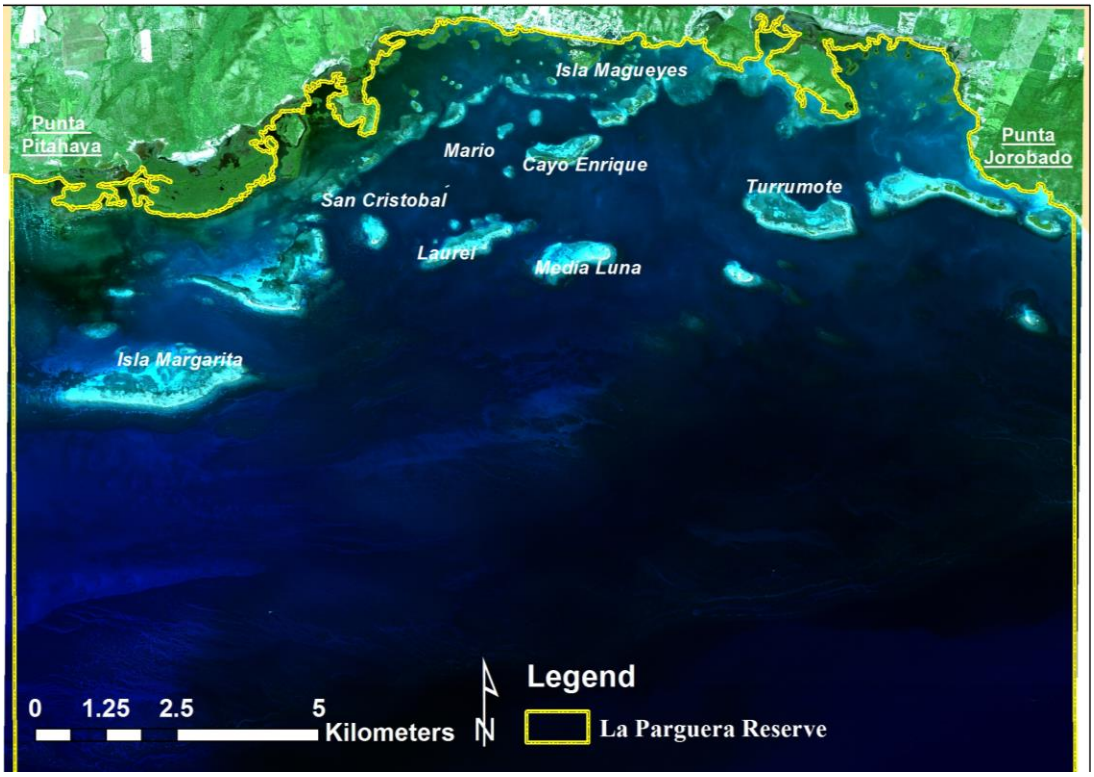

Figure 5: WorldView 2 image, subset of La Parguera Reserve.

Objectives

This study is divided into three efforts each covered by a corresponding chapter. The first one (Chapter 1) titled **High-resolution Bathymetry from Passive Sensors,** focuses on quantitatively testing the capability of a multispectral remote-sensing reflectance model for deriving bottom depths in a shallow water marine environment by comparing model-derived depths to high-resolution bathymetry data. We also analyzed the importance of the atmospheric correction in enhancing bathymetry estimation from passive sensors. The second chapter (Chapter 2), **High Resolution Bottom Albedo and Water Optical Characterization of La Parguera Reserve from Active and Passive sensors** covers the development of the bottom albedo image, including the image preprocessing for the hyperspectral data and the active sensor data. These parameters were used in various bio-optical algorithms to deduce Apparent and Inherent bio-optical properties and bottom albedo to ultimately produce a benthic habitat map. A new baseline bio-optical data and bottom albedo images were developed for the waters of La Parguera Reserve. The third chapter, **Benthic Habitat Map of La Parguera Reserve using Passive and Active Remote Sensing Data**, we developed a high resolution benthic habitat for La Parguera from bottom albedo using passive and active sensor fusion. These maps were focused on characterizing benthic habitats for the total extension of La Parguera Reserve to the shelf edge and in the limits of detection of imagery. Also, a detailed comparison between these benthic habitat maps against previously available maps with emphasis in habitat prediction and validation. This detailed benthic habitat map analysis includes an assessment of spatial patterns and distribution of coral reefs thought out the insular shelf and the optical variability of the waters in the reserve.

References

Aguilar-Perera, Alfonso, Michelle Schärer, and Manuel Valdés-Pizzini. 2006. "Marine Protected Areas in Puerto Rico: Historical and Current Perspectives." *Ocean and Coastal Management* 49: 961–75. doi:10.1016/j.ocecoaman.2006.08.011.

Albert, a, and C Mobley. 2003. "An Analytical Model for Subsurface Irradiance and Remote Sensing Reflectance in Deep and Shallow Case-2 Waters." *Optics Express* 11 (22): 2873–90. doi:10.1364/OE.11.002873.

Albert, Andreas, and Peter Gege. 2006. "Inversion of Irradiance and Remote Sensing Reflectance in Shallow Water between 400 and 800 Nm for Calculations of Water and Bottom Properties." *Applied Optics* 45 (10): 2331–43. doi:10.1364/AO.45.002331.

Bierwirth, P N, T J Lee, and R V Burne. 1993. "Shallow Sea-Floor Reflectance and Water Depth Derived by Unmixing Multispectral Imagery." *Photogrammetric Engineering and Remote Sensing* 59: 331–38.

Brando, V E, and a G Dekker. 2003. "Satellite Hyperspectral Remote Sensing for Estimating Estuarine and Coastal Water Quality." *IEEE Transactions on Geoscience and Remote Sensing* 41 (6): 1378–87. doi:10.1109/TGRS.2003.812907.

Brando, Vittorio E., Janet M. Anstee, Magnus Wettle, Arnold G. Dekker, Stuart R. Phinn, and Chris Roelfsema. 2009. "A Physics Based Retrieval and Quality Assessment of Bathymetry from Suboptimal Hyperspectral Data." *Remote Sensing of Environment* 113: 755–70. doi:10.1016/j.rse.2008.12.003.

Collin, Antoine, and James L. Hench. 2012. "Towards Deeper Measurements of Tropical Reefscape Structure Using the WorldView-2 Spaceborne Sensor." *Remote Sensing* 4: 1425–47. doi:10.3390/rs4051425.

Costa, B. M., T. a. Battista, and S. J. Pittman. 2009. "Comparative Evaluation of Airborne LiDAR and Ship-Based Multibeam SoNAR Bathymetry and Intensity for Mapping Coral Reef Ecosystems." *Remote Sensing of Environment* 113 (5). Elsevier Inc.: 1082–1100. doi:10.1016/j.rse.2009.01.015.

Gao, J. 2009. "Bathymetric Mapping by Means of Remote Sensing: Methods, Accuracy and Limitations." *Progress in Physical Geography* 33 (1): 103–16. doi:10.1177/0309133309105657.

Garcia-Sais, Jorge, Richard Appeldoorn, Tim Battista, Laurie Bauer, Andy Bruckner, Chris Caldow, Lisamarie Carrubba, et al. 2008. "The State of Coral Reef Ecosystems of Puerto Rico." *State of the Coral Reef Ecosystems of the United States 2008*, 75–116.

Garcia-Sais, Jr. 2005. “Inventory and Atlas of Corals and Coral Reefs, with Emphasis on Deep-Water Coral Reefs from the US Caribbean EEZ.” *Caribbean Fisheries Manage Ment*, 218.

Gardner, Toby a, Isabelle M Côté, Jennifer a Gill, Alastair Grant, and Andrew R Watkinson. 2003. “Long-Term Region-Wide Declines in Caribbean Corals.” *Science (New York, N.Y.)* 301 (2003): 958–60. doi:10.1126/science.1086050.

Hoegh-Guldberg, O, P J Mumby, a J Hooten, R S Steneck, P Greenfield, E Gomez, C D Harvell, et al. 2007. “Coral Reefs under Rapid Climate Change and Ocean Acidification.” *Science (New York, N.Y.)* 318 (2007): 1737–42. doi:10.1126/science.1152509.

Hoegh-Guldberg, Ove. 1999. “Climate Change, Coral Bleaching and the Future of the World’s Coral Reefs.” *Marine and Freshwater Research* 50: 839. doi:10.1071/MF99078.

Jerlov, NG. 1976. *Marine Optics*. 2nd ed. Amsterdam: Elsevier Scientific Publishing Company.

Kirk, J. T. O. 1984. “Dependence of Relationship between Inherent and Apparent Optical Properties of Water on Solar Altitude.” *Limnology and Oceanography* 29 (2): 350–56. doi:10.4319/lo.1984.29.2.0350.

Lee, Z, K L Carder, C D Mobley, R G Steward, and J S Patch. 1999. “Hyperspectral Remote Sensing for Shallow Waters. 2. Deriving Bottom Depths and Water Properties by Optimization.” *Applied Optics* 38 (18): 3831–43. doi:10.1364/AO.38.003831.

Lee, Zhongping, Kendall L. Carder, Robert F. Chen, and Thomas G. Peacock. 2001. “Properties of the Water Column and Bottom Derived from Airborne Visible Infrared Imaging Spectrometer (AVIRIS) Data.” *Journal of Geophysical Research* 106: 11639. doi:10.1029/2000JC000554.

Lobitz, B, L Guild, and R Armstrong. 2008. “Pre-Processing 2005 AVIRIS Data for Coral Reef Analysis.” *... International Coral Reef ...*, no. 17: 7–11. http://www.nova.edu/ncri/11icrs/proceedings/files/m17-10.pdf.

Lyzenga, D R. 1978. “Passive Remote Sensing Techniques for Mapping Water Depth and Bottom Features.” *Applied Optics* 17: 379–83. doi:10.1364/AO.17.000379.

Maritorena, Stéphane, André Morel, and Bernard Gentili. 1994. “Diffuse Reflectance of Oceanic Shallow Waters: Influence of Water Depth and Bottom Albedo.” *Limnology and Oceanography* 39 (7): 1689–1703. doi:10.4319/lo.1994.39.7.1689.

Menza, C, M Kendall, and S Hile. 2008. “The Deeper We Go the Less We Know.” *International Journal of Tropical Biology* 56 (Supple (May): 11–24.

Mobley, C D, B Gentili, H R Gordon, Z Jin, G W Kattawar, A Morel, P Reinersman, K Stamnes, and R H Stavn. 1993. “Comparison of Numerical Models for Computing Underwater Light Fields.” *Applied Optics* 32: 7484–7504. doi:10.1364/AO.32.007484.

Mobley, Curtis D. 2011. “Fast Light Calculations for Ocean Ecosystem and Inverse Models.” *Optics Express* 19 (20): 18927. doi:10.1364/OE.19.018927.

Morel, Andre. 1974. “Optical Properties of Pure Water and Pure Sea Water.” *Optical Aspects of Oceanography*. papers2://publication/uuid/B25019FC-9ED0-45D6-881A-6BE952393296.

Morel, André, and Stéphane Maritorena. 2001. “Bio-Optical Properties of Oceanic Waters: A Reappraisal.” *Journal of Geophysical Research* 106: 7163. doi:10.1029/2000JC000319.

Morelock, J., W Schneiderman, and N Bryant. 1977. “Shelf Reefs, Southwestern Puerto Rico.” *Studies in Geology* 4: 17–25.

Morelock, Jack, Elizabeth a Winget, and Carlos Goenaga. 1994. *Geologic Maps of the Southwestern Puerto Rico Parguera To Guanica Insular Shelf*.

Philpot, W D. 1989. “Bathymetric Mapping with Passive Multispectral Imagery.” *Applied Optics* 28 (8): 1569–78. doi:10.1364/AO.28.001569.

Polcyn, F. C., W. L Brown, and I. J. Sattinger. 1970. *The measurement of water depth by remote sensing techniques*. Ann Arbor, Michigan.

Preisendorfer, Rudolph W. 1976. *Hydrologic Optics Introduction Volume 1*. Honolulu, Hawaii.

Purkis, Samuel and Klemas, Victor. 2011. *Remote Sensing and Global Environmental Change*. First. Wiley-Blackwell.

Rohmann, S. O., J. J. Hayes, R. C. Newhall, M. E. Monaco, and R. W. Grigg. 2005. “The Area of Potential Shallow-Water Tropical and Subtropical Coral Ecosystems in the United States.” *Coral Reefs* 24: 370–83. doi:10.1007/s00338-005-0014-4.

Sandidge, Juanita C., and Ronald J. Holyer. 1998. “Coastal Bathymetry from Hyperspectral Observations of Water Radiance.” *Remote Sensing of Environment* 65: 341–52. doi:10.1016/S0034-4257(98)00043-1.

Sanford, Thomas B., Kathryn A. Kelly, and David M. Farmer. 2011. “Sensing the Ocean.” *Physics Today* 64: 24–28. doi:10.1063/1.3554313.

Smith, R C, and K S Baker. 1981. “Optical Properties of the Clearest Natural Waters (200--800\,nm).” *Appl. Opt.* 20 (1): 177–84. doi:10.4319/lo.2007.52.1.0217.

Stephenson, Darren. 2007. “Relative Reflectivity: Descriptive Report” 2007.

Stephenson, Darren and Sinclair, Mark. 2006. “Hydrographic Lidar: Data Acquisition and Processing Report.”

Stumpf, Richard P, Kristine Holderied, and Mark Sinclair. 2003. "Determination of Water Depth with High-Resolution Satellite Imagery over Variable Bottom Types." *Limonology And Oceanography* 48: 547–56. doi:10.4319/lo.2003.48.1_part_2.0547.

Tuell, G. H., J. Y. Park, J. Aitken, V. Ramnath, V. Feygels, and Y. Kopelivich. 2005. "Fusion of SHOALS Bathymetric Lidar and Passive Spectral Data for Shallow Water Rapid Environmental Assessment." *Oceans 2005 - Europe* 2: 1046–51. doi:10.1109/OCEANSE.2005.1513202.

UNESCO. 1998. *CARICOMP – Caribbean Coral Reef, Seagrass and Mangrove Sites Coastal Region and Small Island Papers 3, La Parguera Puerto Rico. UNESCO.* Paris, France. http://www.unesco.org/csi/pub/papers/garciab.htm.

Warne, A.G., Webb, R.M.T., and Larsen, M.C. 2005. *Water , Sediment , and Nutrient Discharge Characteristics of Rivers in Puerto Rico and Their Potential Influence on Coral Reefs*.

Chapter 2: High-resolution bathymetry from passive sensors.

Abstract

The use of satellite sensors or airborne sensors in shallow waters is complicated by the combined atmospheric, water, and bottom signals. Accurate determination of water depth is important both for the purpose of monitoring underwater topography and movement of deposited sediments, and for producing nautical charts in support of navigation. A Worldview 2 (WV2) image was used to produce a bathymetric map with a significant spatial resolution (4 meters). It was validated using bathymetric data from an active sensor (LiDAR). Additional analysis was conducted to evaluate the influence of atmospheric corrections in depth retrievals, and the Dark Substract, Fast Line-of-Sight Atmospheric Analysis of Spectral Hypercubes (FLAASH) and the Cloud Shadow Approach (CSA) atmospheric corrections were tested. The CSA method using a simple band ratio (Band2/Band3) provided the best performance. A second order polynomial equation explained 82% of the model values ($r^2 = 0.82$). The WV2 depth model was evaluated in another site within the image, where it successfully retrieved depth values with a coefficient of determination (r^2) of 0.90 for all the depth values sampled, and an r^2 of 0.70, for depths in the range of 20 meters RMSE of 1.43 meters. These results confirmed that passive sensors can be used to retrieve high-resolution bathymetry when combined with a robust atmospheric correction even in areas with variable bottom composition.

1. Introduction

Accurate determination of water depth is important both for the purpose of monitoring underwater topography and movement of deposited sediments, and for producing nautical charts in support of navigation (Gao 2009). Water depth information is fundamental in discriminating and characterizing coral reef habitats, and also allows estimation of bottom albedo, which can improve benthic habitat mapping (Mumby and Harborne 1999). The use of satellite sensors or airborne sensors in shallow waters is complicated by the combined atmospheric, water, and bottom signals. This includes variations due to water column scattering and absorption due to dissolved and suspended materials such as sediments, chlorophyll, and colored dissolved organic matter. Some of these limitations have been overcome by the introduction of high-resolution multispectral sensors that use light reflected from the seafloor to extract benthic information (Arnone et al. 2006; McIntyre et al. 2006).

Previous researchers have mapped water depth but, in many cases, the methods that were used required the input of known depth values (Lyzenga 1978), or assumptions that a pair of spectral bands can be identified such that the ratio of the reflectance in these two bands was the same for all the bottom types (Philpot, 1989). The limitations and validity of obtaining water depth from passive sensors was demonstrated by Maritorena et al. (1994). Lyzenga et al. (2006) further enhanced the methodology using multiple linear regressions, which required knowing the optical properties of the water at the time of image acquisition.

Stumpf et al. (2003) expanded on the strategy developed by Lyzenga (1981) of the blue/green spectral bands for depth estimates by reducing the number of parameters that needed to be estimated. The ratio transform proposed by Stumpf et al. (2003) assumed that depth-driven

change is significantly larger than the corresponding benthic albedo-driven change. These authors used the ratio transform with two IKONOS satellite sensor wavebands, characterized by differential water attenuation.

Mishra et al. (2005) estimated water depth for each pixel based on a site-specific polynomial model, using high-resolution multispectral IKONOS data in a site near Roatan Island, Honduras. A ratio of wavebands (blue and green) were identified that were constant for all bottom types, and it was found that the correlation coefficient between actual depth and estimated depth was 0.942, with an RMS error of 2.711 m. Based on this approach the model overestimates depths beyond 21 m.

Conger et al. (2006) used QuickBird satellite multispectral sensor imagery and LiDAR Scanning Hydrographic Operational Airborne Lidar Survey (SHOALS) data to develop a simple technique to decorrelate remote sensing color band data from depth in optically shallow water and generating depth invariant bands while maintaining relative spectral information. The World View 2 sensor was used by Kerr (2011) to identify an optimal model for estimating bathymetry within a near-shore coral reef system based on six water-penetrating bands. The accuracy of the depth estimation models was quantified using LiDAR SHOALS data that overlapped the study area offshore of Key Largo in the northern Florida Keys National Marine Sanctuary. The model used was based on the theory by Lyzenga (1978) (using blue/green ratios) and improved with the model from Stumpf et al. (2003) using a ratio of the blue/green spectral bands for depth estimates. This study demonstrated that improving the Stumpf model by including a greater number of band-ratios provided by the WV2 sensor provided a better solution for optically-derived bathymetry.

Collin and Hench (2012) presented other approach in which water depth was retrieved from the World View 2 imagery based on different band combinations from all bands (including 5 visible bands) provided by the sensor. This built on the Stumpf et al. (2003) method, enhanced the digital depth models and increased the range of depth estimation by testing different atmospheric corrections and spatial resolutions.

Hyperspectral sensors have been used to derive properties of the water column and bottom, which includes bottom albedo and water depths. The AVIRIS hyperspectral sensor was used to obtain water depth, as well as other properties based on model-derived image optimization techniques (Lee et al. 1999 and 2001). The results suggested that the model and methods work well for extracting subsurface water properties and demonstrated that the model-derived depths agree with depths measured from 0–4.6 m. The AVIRIS sensor was also used in deriving bottom depths in a shallow water marine environment utilizing a remote sensing reflectance model and comparing the model-derived depths to high-resolution LiDAR bathymetry data (McIntyre et al. 2006).

A different approach was used by Mishra et al. (2007) In this study, a site-specific algorithm was developed for mapping high-resolution bathymetry using the remote sensing reflectance derived from a hyperspectral sensor corrected for atmospheric effects. The method is based on the assumption that the use of two bands allows separation of variations in depth from variations in bottom albedo. This method also compensates implicitly for variable bottom types and the per-pixel bathymetric knowledge was used to eliminate the change in reflectance that is attributable

to variable depth and water column attenuation effects, while deriving bottom albedo (Mishra et al. 2007)

The present work has similarities as well as differences in the methods utilized from previous remote sensing-derived bathymetry approaches. This study presents the first high-resolution large scale water depth map for La Parguera Reserve derived from passive sensors. This bathymetric map was developed to a significant spatial resolution (4 meters) and was validated using bathymetric data from an active sensor (LiDAR). The project includes an analysis of methods and sensors to derive optimum bathymetry values from passive sensors and the influence of atmospheric corrections in depth retrievals that could also be implemented throughout the Caribbean and elsewhere.

2. Methods and Materials

2.1 Image Preprocessing

Image data preprocessing included data resampling, radiometric corrections to transform data from at sensor radiance to remote sensing reflectance, and atmospheric corrections to remove the contribution of the atmosphere to the signal.

2.1.1 LiDAR SHOALS image processing

Data processing for the LiDAR image was done using Exelis ENVI 5.0 image-processing software. The LiDAR image was evaluated for data gaps and a subset of the image was made based on the La Parguera Reserve polygon shown in Chapter 1-Figure 1. The co-registration was done were the LiDAR image was the base image for the other co-registrations. A total of 40 points were used as ground control points for the registration and the total RMSE for the co-registration was 0.5 meters.

2.1.2 WorldView 2

The WorldView 2 (WV2) image was radiometrically corrected before any additional processing was performed. This radiometric correction used the WorldView Radiance calibration routine in ENVI 5.0, which converts relative radiance into absolute radiance in units of ($\mu W /cm^2 *nm*sr$) based on the calibration factor for each band. The WV2 image was evaluated for data gaps and a subset of the image was made based on the La Parguera Reserve polygon. The original spatial resolution of the WV2 image was 1.84 meters, so the image was resampled to 4 meters to match the spatial resolution of the LiDAR image. The WV2 image was warped for the co-registration with the LiDAR image and both were set to the coordinate system World Geodetic Survey 84

(WGS-84). A total of 40 points were used as ground control points for the registration and the total RMSE for the co-registration was 0.5 meters.

2.2 Ancillary data

The images were corrected for fluctuations in tide readings and these were measured at the Magueyes Island Tide Station (Station ID 9759110) in La Parguera, Lajas, Puerto Rico (NOAA, Tide and Currents, 2005). The WV2 image was acquired on December 4, 2011 (15:25 GMT) with the tide reading for this station at 0.249 meters above mean low level water (MLLW) (15:24 GMT) (NOAA, Tide and Currents, 2011). The LiDAR SHOALS bathymetry data was processed and corrected for errors in position and tidal changes (Stephenson and Sinclair 2006).

2.3 Atmospheric corrections

An important step in multispectral and hyperspectral remote sensing of ocean targets is to correct for atmospheric effects. To analytically derive water and/or bottom properties from any satellite ocean color data, the first step is to get high-quality spectral remote sensing reflectance (Rrs) that contains water and/or bottom information (Lee et al. 2007). There are several methods for atmospheric correction currently available for both multispectral and hyperspectral imagery. To account for some of the atmospheric variability we applied two types of corrections to our imagery; a simple atmospheric correction (i.e. Dark Pixel Subtraction) and two complex atmospheric corrections (i.e. FLAASH, CSA). With this approach we then further evaluated the influence of the atmospheric correction in bathymetry retrievals.

2.3.1 Dark Pixel Subtraction

The Dark Pixel Subtraction or Dark Subtraction Routine removes the dark noise from the image. It is based on the assumption that dark objects reflect no light; any value greater than zero must result from atmospheric scattering. The scattering is removed by subtracting this value from every pixel in the band by Band Minima or User Values for each band. The Band Minima approach was used over an area of deep oceanic pixels was selected and a dark subtraction was performed on the WV2 image.

2.3.2 FLAASH

The Fast Line-of-Sight Atmospheric Analysis of Spectral Hypercubes (FLAASH) is a first-principles atmospheric correction tool that corrects wavelengths in the visible through near-infrared and shortwave infrared regions and it is based on the MODTRAN4 radiation transfer code (Matthew et al. 2002). It can be used in multispectral and hyperspectral imagery and basically consist of defining the tropical atmosphere over a maritime area and solve the radiative transfer equation. One of the limitations of FLAASH is that requires that the image contains bands in appropriate wavelength positions for water vapor and aerosol retrieval corrections. For the WV2 image, these bands were not available for this correction to be applied with the longest wavelength available centered at 950nm. Still, the FLAASH atmospheric correction was evaluated for the WV2 image.

2.3.3 Cloud-Shadow Approach (CSA)

The Cloud Shadow Approach (CSA) is a practical image-driven method for correcting the effects of atmosphere and obtains remote sensing reflectance from the image. This technique was

originally developed by (Reinersman et al. 1998) and in this updated approach by Lee et al. (2007), the atmospheric radiance (La) is calculated from a pair of sun and shadow pixels, where the product of (t) transmittance and downwelling irradiance (*Ed)* is estimated using the reflected radiance from the top of clouds (Gregg and Carder 1990). One advantage of this image driven approach is that all radiance come from the same sensor and is collected simultaneously.

For this application of the CSA we used a modified approach from Lee et al. (2007). Since the image for the selected study area had no clouds, we used the shadow of a tall building in our study area to obtain the sun-shadow pixels. To calculate the reflectance we collected *in situ* spectra of a homogenous area on the rooftop of the building using a field spectroradiometer (GER 1500) within the sun-shadow pixels selected. For the Ed sky/ Ed total ratio we used the EKO Tracker STR-22 Multiple Radiometers instrument at the Bio-Optical Oceanography Laboratory in Isla Magueyes, which collects irradiance from direct and diffuse solar radiation and had data for the exact image day/time acquisition. The final product is an atmospheric corrected WV2 image with values of remote sensing reflectance (Rrs, sr^{-1}).

2.4 Bathymetry Retrieval

In the water column, the spectral signal undergoes selective exponential attenuation in the visible region as mediated by absorption and scattering processes (Kirk 2011). There have been different approaches to map water depth based on the use of wavebands or combinations of wavebands. Our approach was focused on deriving depth using band combinations (band ratios) to maximize the use of visible bands available from WV2. This approach used a simple blue/green band ratio for the WV2 image. The technique was also used to evaluate the influence of the atmospheric correction in bathymetry retrievals. The selected band combinations were calibrated using LiDAR SHOALS to derive bathymetry.

2.4.1 Depth estimated from Band Ratios

The bands selected were based in visible bands in the blue/green region that provide better water penetration for successful bathymetry retrieval. This approach assumes that a pair of wave bands can be identified and that the ratio of the reflectance in these two bands was the same for all bottom types within a given scene (Philpot 1989). All 5 visible WV2 bands were evaluated but, only combinations with band 1, band 2, and band 3 were finally selected for the estimation of bathymetry.

Once we established the best band pairs from the imagery, a simple band ratio was calculated for the selected pairs for each sensor (i.e. Band 1/ Band 2). According to Mishra et al. (2007) wavebands (blue and green) have different water absorptions, one band will have arithmetically lesser values than the other while changes in bottom albedo affects both bands similarly. Also, as depth increases, radiance of the band with higher absorption (green) decreased proportionally faster than the band with lower absorption (blue); and the radiance ratio of the blue to the green increased (Gordon and Brown 1974).

2.4.2 Ground-truth from LiDAR SHOALS

To establish a relationship between bottom depth from WV2 band ratios and depth from LiDAR SHOALS bathymetry, a random sample was used to extract the values from both images. This random sample consisted of 5000 points and accounted for all bottom types and depths across the images. These random points were constrained to the La Parguera Reserve Boundary and used as ground-truth data (Figure 1).

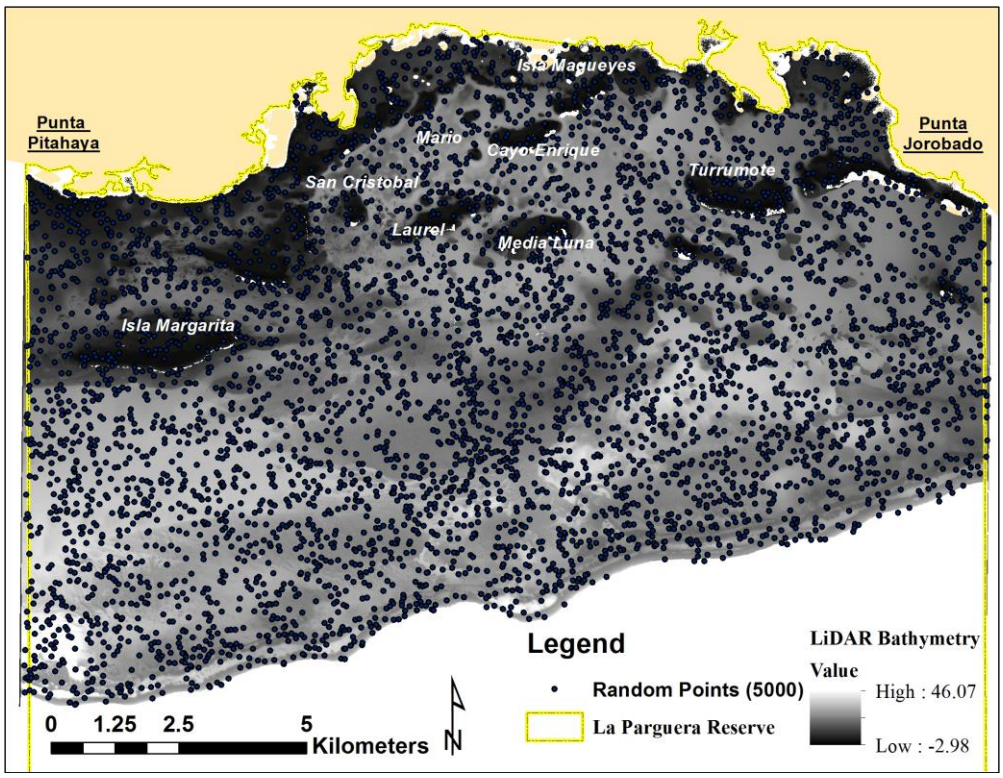

Figure 1: LIDAR SHOALS random points selected for La Parguera Reserve.

3. Results

3.1 Atmospheric corrections

After the atmospheric corrections were applied to the WV2 image, we evaluated above water spectra for several areas in our study site (Figure 2). Qualitative interpretation of Figure 7 suggest that the CSA and Dark Subtract atmospheric corrections performed better in maintaining the spectral curves for the substrate (ex. mangroves) than the image without atmospheric correction and the FLAASH atmospheric correction.

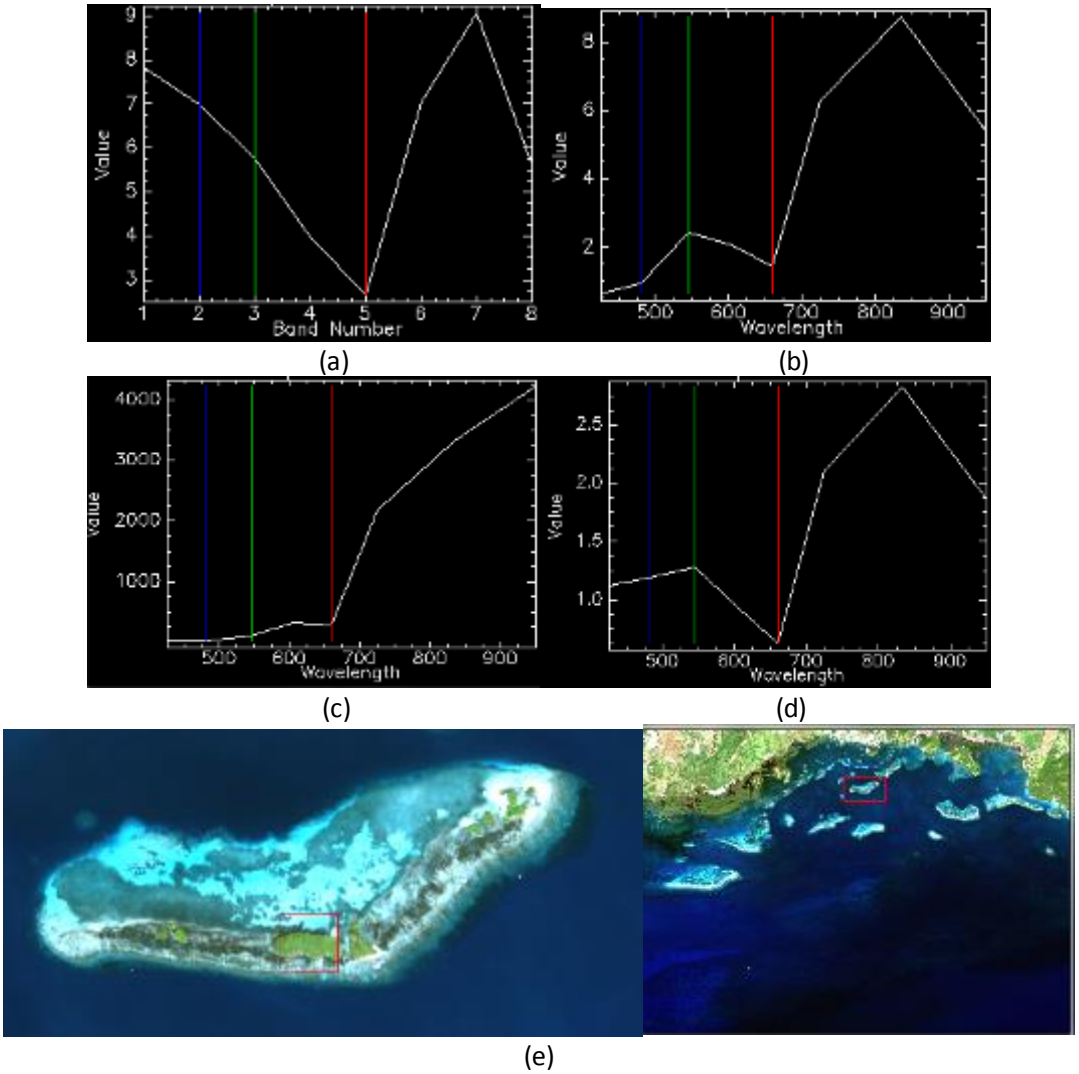

Figure 2: (Top) WV2 image above water spectra for mangroves from (a) no atmospheric correction, (b) dark subtract atmospheric correction, (c) FLAASH atmospheric correction, (d) CSA atmospheric correction. Cayo Enrique area location in La Parguera Reserve (e).

To evaluate the atmospheric influence in the remote sensed signal, radiance values of water over different bottom types were analyzed before and after the atmospheric correction. These bottom types include seagrass, sand, corals, mud and deepwater (Figure 3). The results after the atmospheric correction show that sand had the highest values when compared to other substrates (seagrass, mud). The atmospheric influence for all substrates was estimated at 83% and the "coastal blue", blue and green bands were found to have the higher values after atmospheric correction, while the near infrared values were all reduced to near zero.

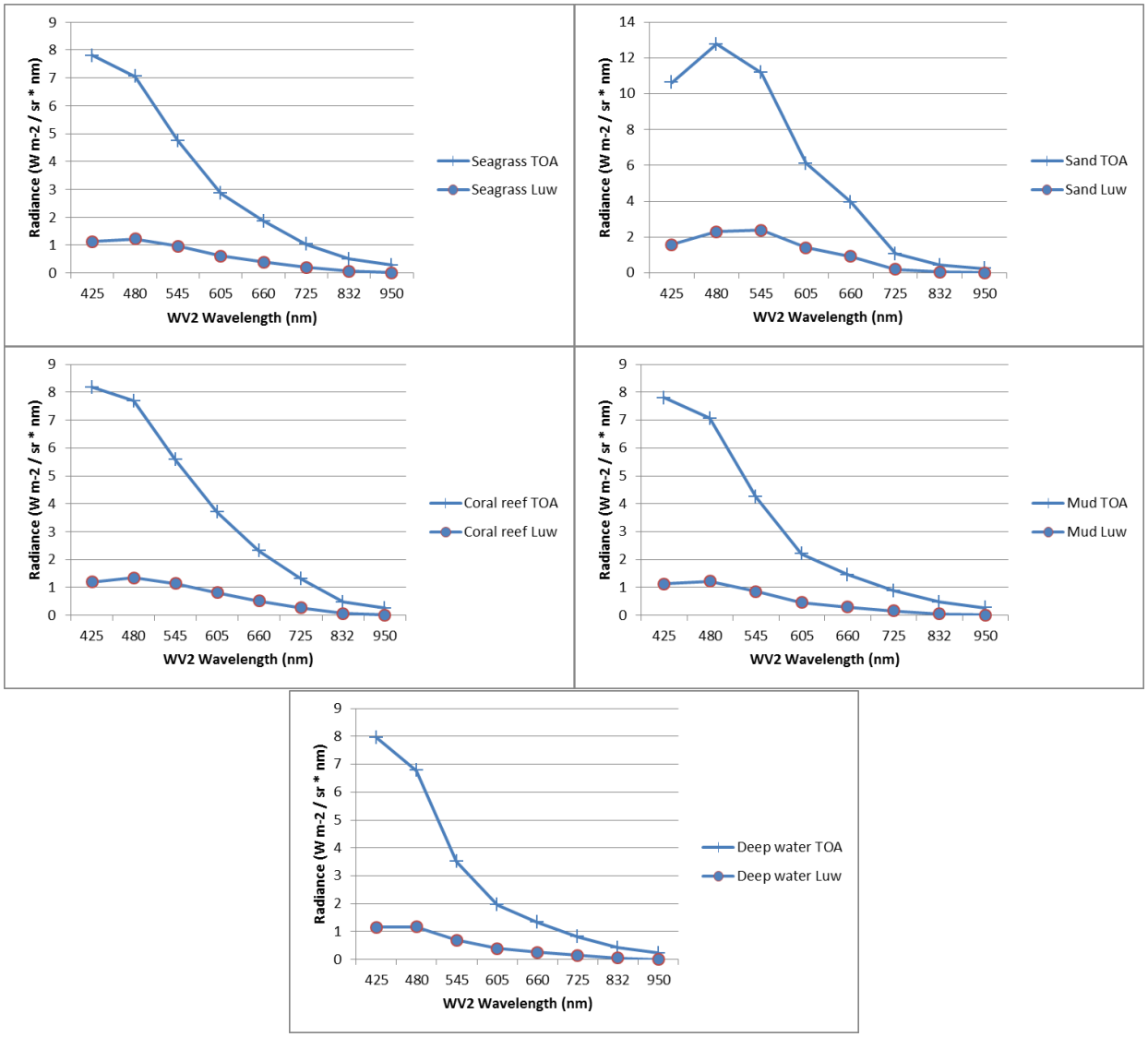

Figure 3: Comparison of top of atmosphere (TOA) and water leaving radiances (Luw) derived from WV2 image over different substrates that include seagrass, sand, coral reef, mud and deep water. Notice the scale in the y-axis in the sand graph.

3.2 LiDAR depths

LiDAR bathymetry data for the study area ranged from 0 to 46.07 meters. The inner shelf area can be distinguished by its complex physiography of submerged patch and emergent reefs, inshore cays, and mud and seagrass plains and depths ranging from 0 to 20 meters. The mid and outer shelfs have a wider range of depths ranging from 10 to 47 meters, with the deeper areas located in the southwest area of the reserve (>30 meters) near the shelf edge. This area is characterized by extensive coral reef development, especially near the shelf edge, where depth can range from approximately 12 to 35 meters. The average depth is approximately 16.06 meters for the selected areas (Figure 4).

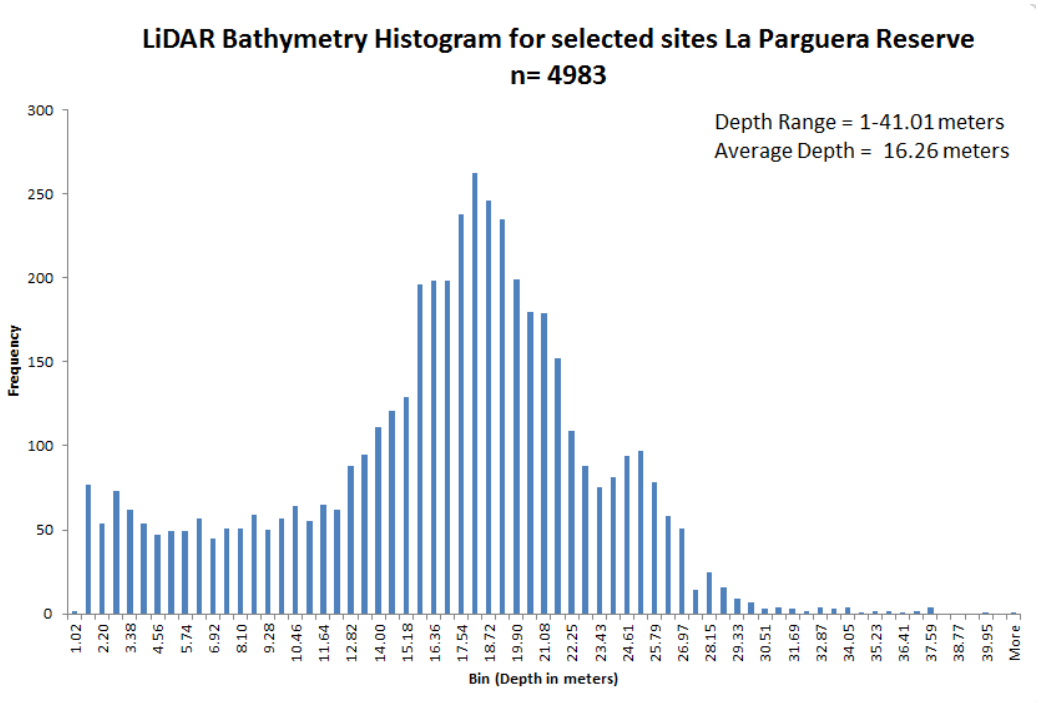

Figure 4: LiDAR SHOALS depth histogram for the selected points in La Parguera Reserve.

3.3 Simple Band Ratios

Different band ratios were developed to determine the best ratio to retrieve bathymetry from each sensor. The band selection was based in selecting bands in the blue/green region that provided the best water penetration for successful bathymetry retrieval.

3.3.1 WV2

Based on this approach 3, 2 band ratios (B1/B2, B1/B3, B2/B3) from WV2 visible bands were selected for six depth ranges. A Pearson-product moment relationship was developed to examine the performance of band ratios for different atmospheric corrections (Table 1).

	WV2 2 (n=3 band ratios)			
	No Atmospheric Correction	Dark Subtract	FLAASH	Cloud Shadow
Average	0.371	0.466	0.218	0.792
Median	0.378	0.456	0.234	0.855
Maximum	0.599	0.772	0.417	0.875
Minimum	0.122	0.228	0.005	0.645

Table 1: A Pearson-product moment relationship (r) values for the 3 best band ratio combination (b1/b2, b1/b3, b2/b3) for the different atmospheric corrections when compared to LiDAR SHOALS per pixel values.

WV2 Sensor									
		No Atmospheric Correction		Dark Subtract		FLAASH		Cloud Shadow	
Depth	**Band Ratio**	**R**	**R^2**	**R**	**R^2**	**R**	**R^2**	**R**	**R^2**
25-35m	B1/B2	0.247	0.061	0.382	0.146	0.005	0.00002	0.269	0.073
	B1/B3	0.393	0.154	0.479	0.229	0.417	0.174	0.418	0.175
	B2/B3	0.193	0.037	0.347	0.121	0.252	0.063	0.233	0.054
20-30m	B1/B2	0.122	0.015	0.310	0.096	0.087	0.008	0.142	0.020
	B1/B3	0.526	0.277	0.561	0.315	0.321	0.103	0.562	0.316
	B2/B3	0.489	0.239	0.563	0.318	0.380	0.145	0.515	0.265
15-25m	B1/B2	0.175	0.031	0.315	0.099	0.046	0.002	0.182	0.033
	B1/B3	0.411	0.169	0.498	0.248	0.217	0.047	0.471	0.222
	B2/B3	0.460	0.212	0.522	0.272	0.275	0.076	0.526	0.276
10-20m	B1/B2	0.204	0.042	0.228	0.052	0.088	0.008	0.209	0.044
	B1/B3	0.294	0.086	0.366	0.134	0.156	0.024	0.348	0.121
	B2/B3	0.316	0.100	0.376	0.141	0.161	0.026	0.395	0.156
5-15m	B1/B2	0.364	0.132	0.434	0.188	0.210	0.044	0.401	0.161
	B1/B3	0.504	0.254	0.682	0.465	0.259	0.067	0.639	0.408
	B2/B3	0.538	0.289	0.652	0.425	0.252	0.063	0.724	0.524
0-10m	B1/B2	0.312	0.098	0.311	0.097	0.187	0.035	0.427	0.182
	B1/B3	0.532	0.283	0.772	0.596	0.300	0.090	0.759	0.576
	B2/B3	0.592	0.350	0.600	0.359	0.309	0.095	0.851	0.723

Table 2: A Pearson-product moment relationship (r) values and coefficient of determination (r^2) for six depth ranges for the different atmospheric corrections. The performance of each band ratio on (b1/b2, b1/b3, b2/b3) was evaluated when compared with LiDAR SHOALS per pixel values.

The data were divided in six depth ranges to evaluate the influence of depth in the band ratio (Table 2). The best overall correlation was from band ratio B2/B3 of WV2 with the CSA atmospheric correction for the depth range of 0-10 meters ($r = 0.851$, $r^2 = 0.723$). The best performance for the image with no atmospheric correction was the band ratio B2/B3 for the 0-10 meters depth ($r = 0.592$, $r^2 = 0.350$). For the dark subtract atmospheric correction the band ratio B1/B3 provided the best performance and was for the depth range of 0-10 meters ($r = 0.772$, $r^2 = 0.596$). For the atmospheric correction FLAASH, the best performance for WV2 was the band ratio B1/B3 for the 25-35 meters depth band ($r = 0.417$, $r^2 = 0.174$).

The band ratios were also evaluated including all sampled points and depth ranges and the performance for the no atmospheric correction were B1/B2= 0.038, B1/B3=0.482, B2/B3=0.603; for dark subtract correction were B1/B2=0.689, B1/B3=0.863, B2/B3=0.845; for the FLAASH atmospheric correction were B1/B2= 0.285, B1/B3=0.454, B2/B3=0.463, and for the CSA atmospheric correction were B1/B2= 0.644, B1/B3=0.855, B2/B3=0.875.

Based on the Pearson-product moment relationship developed to examine the performance of band ratio for different atmospheric corrections, we selected the best models to determine an equation of best fit for the relationship. For the band ratio with no atmospheric correction the equation of best fit was a second order polynomial ($r^2 = 0.654$), for the dark subtract atmospheric correction was a lineal equation ($r^2 = 0.744$), for the FLAASH atmospheric correction the best fit was an exponential equation ($r^2 = 0.481$), and for the CSA atmospheric correction the best fit was a second order polynomial ($r^2 = 0.823$) (Figure 5).

After the selection of the best band ratio and the best model for the relationship a site validation was done to evaluate the model performance in retrieving depth for other locations within the WV2 image. The model selected was the B2/B3 ratio from CSA with a second order polynomial equation ($y = -0.0006x^2 + 0.0359x + 1.1498$). A random sample of 10,000 points was collected for the validation area and values of the WV2 Depth Model and LiDAR SHOALS were obtained.

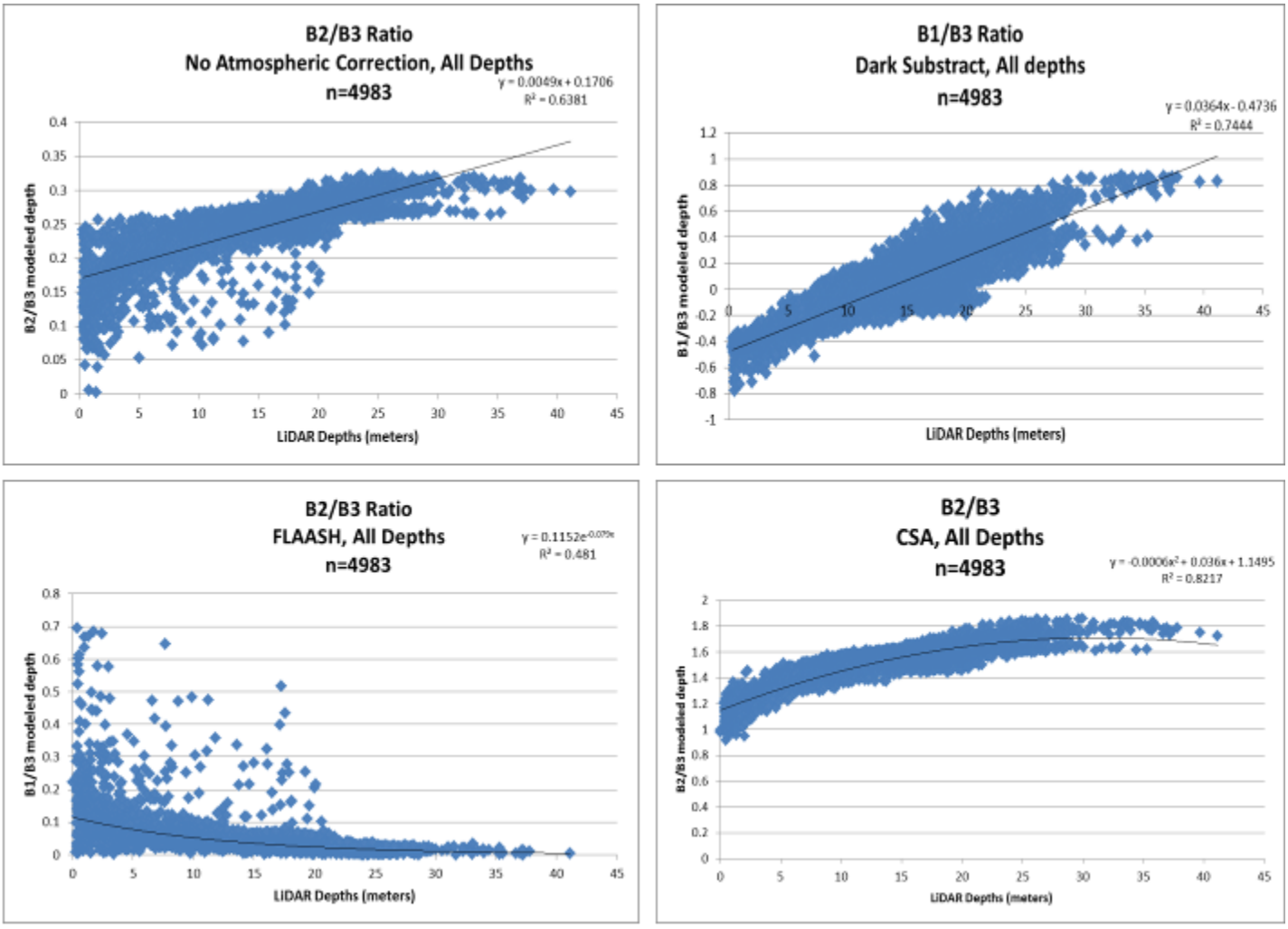

Figure 5: Coefficient of determination and best models to determine an equation of best fit for the relationship between the band ratios of WV2 image and LiDAR SHOALS data. The correlations presented are for the no atmospheric correction (top-left), the dark subtract atmospheric correction (top-right), the FLAASH atmospheric correction (Bottom-left), and the CSA atmospheric correction (bottom-right).

This model was applied to the image and analyzed for accuracy in depth estimation when compared with LiDAR depths. We also evaluated the influence of the atmospheric correction in the bathymetry retrievals.

4. Discussion

The water depth models tested here provided information on the importance of the atmospheric correction used in high resolution imagery analysis. The data followed the results supported by Collin et al. (2012) were the relation between modeled and actual depths varied as a function of the atmospheric correction. This empirical model using regression-based modelling is able to take into account the local set of conditions of the study area, and the atmospheric effects on the electromagnetic waves path in its structure (Baban 1993).

4.1 WV2 depth model

For the WV2, the cloud shadow atmospheric correction provided the best results for all models tested (B1/B2, B1/B3, B2/B3) including all the depth values and depth ranges that were analyzed (r=0.875). Both the cloud shadow and the dark subtract corrected values (r = 0.772) show an improvement from the values of no atmospheric correction (r = 0.592), confirming that the atmospheric correction is an essential radiometric step in the image analysis process (Lyzenga et al. 2006). As expected with bathymetry models from passive sensors (Gordon and Morel 1983), the shallower values from the depth band of 0-10 meters provide the best correlation between modeled and actual values (Table 2). This correlation presented a gradual decrease with increasing depth, and for the depth range 25-35 meters, these values were significantly reduced. However, for this maximum depth range the correlation was improved from 0.397 from the no

atmospheric correction, to 0.479 and 0.418 in the dark subtract correction and cloud shadow corrections, respectively.

For the dark subtract the best model used the combination of the "coastal" band (425 nanometers) with the green band (B1/B3=0.863) for all depth values. The use of the "coastal" band in combination with the green band outperformed the traditional band combination that other very high resolution sensors provide (i.e., QuickBird, IKONOS) where the blue band is centered at 480 nanometers. For the cloud shadow atmospheric correction the best model used the combination of the blue and the green bands (B2/B3=0.823) for all depth values.

The coefficient of determination was obtained and an equation of "best fit" was applied to our depth models. The model with the cloud shadow atmospheric correction provide the best performance with a second order polynomial equation where it explains 82% of the model values (r^2 = 0.823). The results were also analyzed for each of the depth ranges and explains that from an original r^2 = 0.732 at 0-10 meters, the values decrease to r^2 = 0.532 at 5-15 meters, and to r^2 = 0.162 at 10-20 meters, suggesting that the model performance is reduced for values deeper than 15 meters depth range.

For the band ratio with no atmospheric correction the equation of best fit was a linear (r^2 =0.638), and for the FLAASH atmospheric correction the best fit was an exponential equation (r^2 =0.481) (Figure 5). The scatterplot for the FLAASH atmospheric correction show the values dispersed from the exponential model for all depths up to the 23 meters depth band. A present limitation of the FLAASH model for atmospheric correction is that the WV2 imagery does not provide the bands for the water vapor and aerosols models (Collin and Hench 2012).

4.1.1 WV2 model validation

The model from the B2/B3 ratio from CSA with a second order polynomial equation ($y = -0.0006x^2 + 0.0359x + 1.1498$) was applied to another location within the WV2 image (Figure 6) This model was applied to the image and analyzed for accuracy of the model in depth estimation when compared with LiDAR depths.

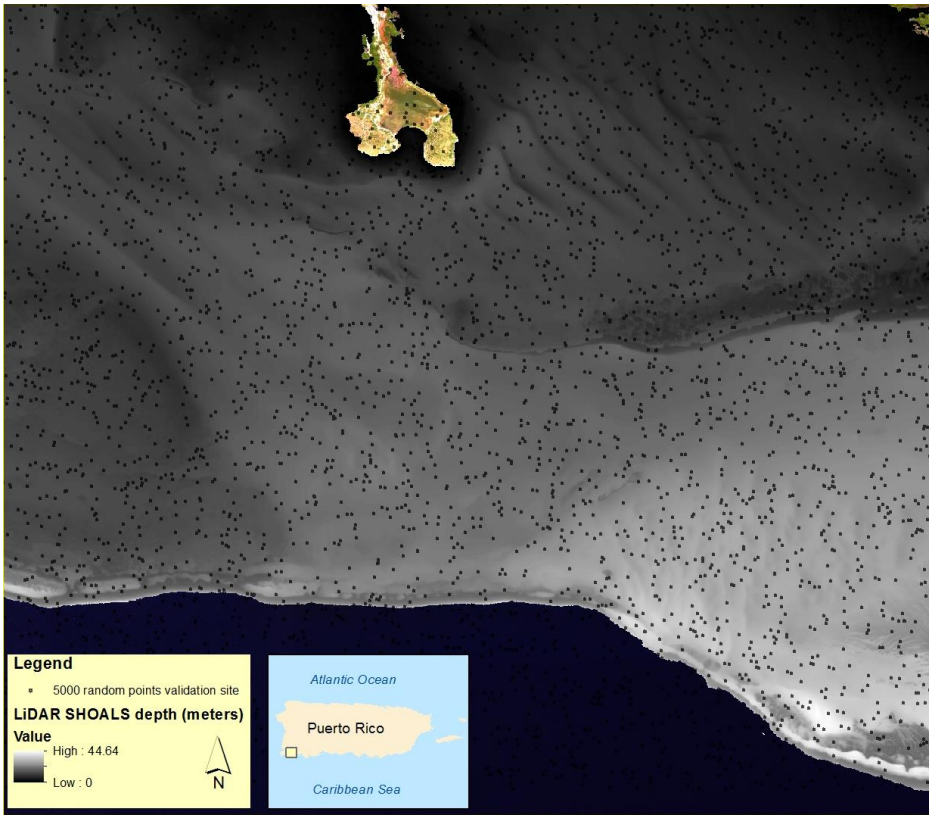

Figure 6: Model validation site within the WV2 image off southwestern Puerto Rico.

This site validation area analyzed shows an average depth of 15.69 meters with a depth range from 1 to 43.33 meters (Figure 7).

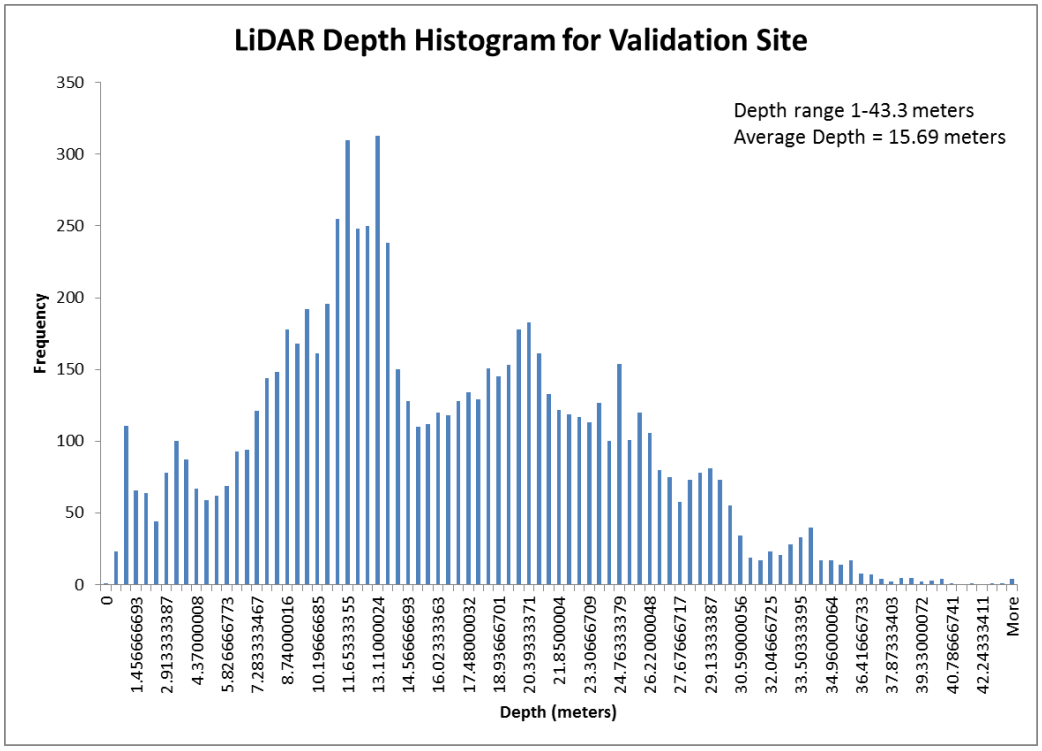

Figure 7: LiDAR SHOALS depth histogram for the selected points in the site validation area Southwestern Puerto Rico.

The values collected from WV2 Depth Model and LiDAR SHOALS were linearized and then plotted to validate the model performance in estimating depth (Figure 8). The coefficient of determination (r^2) was 0.90 for all the depth values sampled. The values were also analyzed to determine the model performance by depth range (Table 3). The WV2 depth model successfully retrieved depth values with an $r^2 = 0.70$ of the depth values to a depth range of 20 meters. Also, of the total values considered (n=8110), 69% of these were between the depth range of 1-20 meters (n=5600). The aggregated Root Mean Square Error (RMSE) for the validation values of the WV2 depth model was 1.56 meters. These values of RMSE increase from 1.26 meters for the 0-10 meters depth range to 1.78 meters for the 25-35 meters depth range. As a final product this equation was applied to the WV2 image to obtain depth for all pixels within the image (Figure 14).

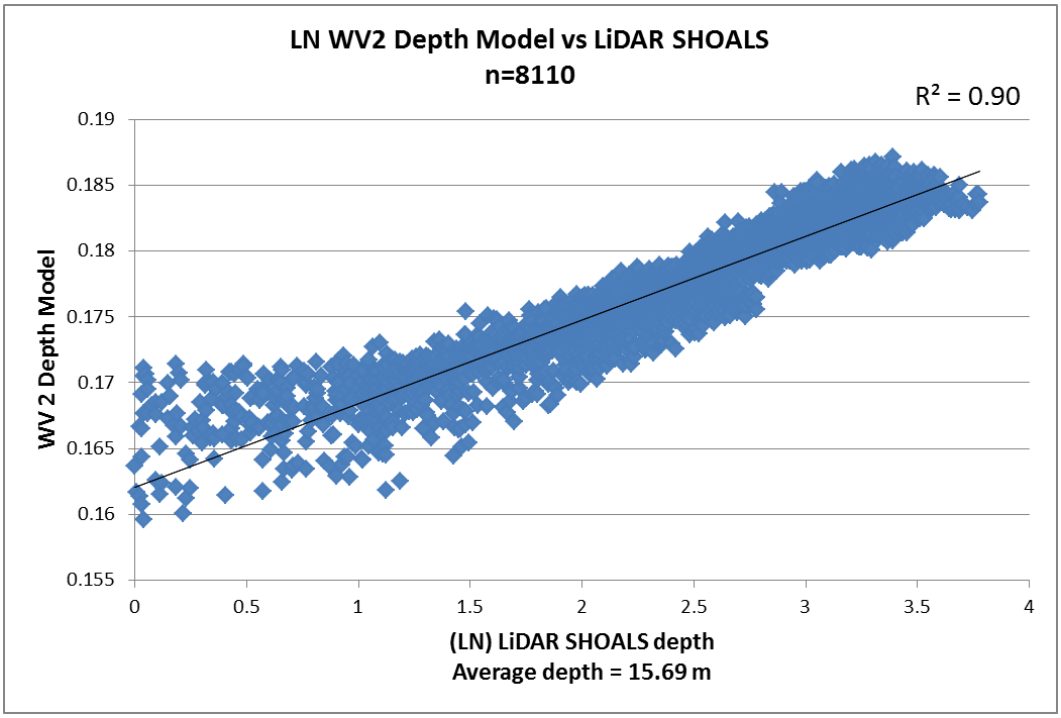

Figure 8: Correlation between values of the WV2 Depth Model and the LiDAR SHOALS depth (meters) linearized.

WV2 Depth Model vs LiDAR SHOALS					
Depth range	**R**	**R^2**	**N**	**Average Error**	**RMSE**
1-10m	0.850	0.723	1921	1.58	1.26
5-15m	0.835	0.698	3591	2.16	1.47
10-20m	0.832	0.692	3672	2.47	1.57
15-25m	0.665	0.443	2760	2.80	1.67
20-30m	0.429	0.184	2180	3.00	1.73
25-35m	0.262	0.068	1101	3.16	1.78
All depths	0.949	0.900	8110	2.43	1.56

Table 3: A Pearson-product moment relationship (r) values, coefficient of determination (r^2), average error and the Root Mean Square Error (RMSE) for six depth ranges for the WV2 depth model for validation.

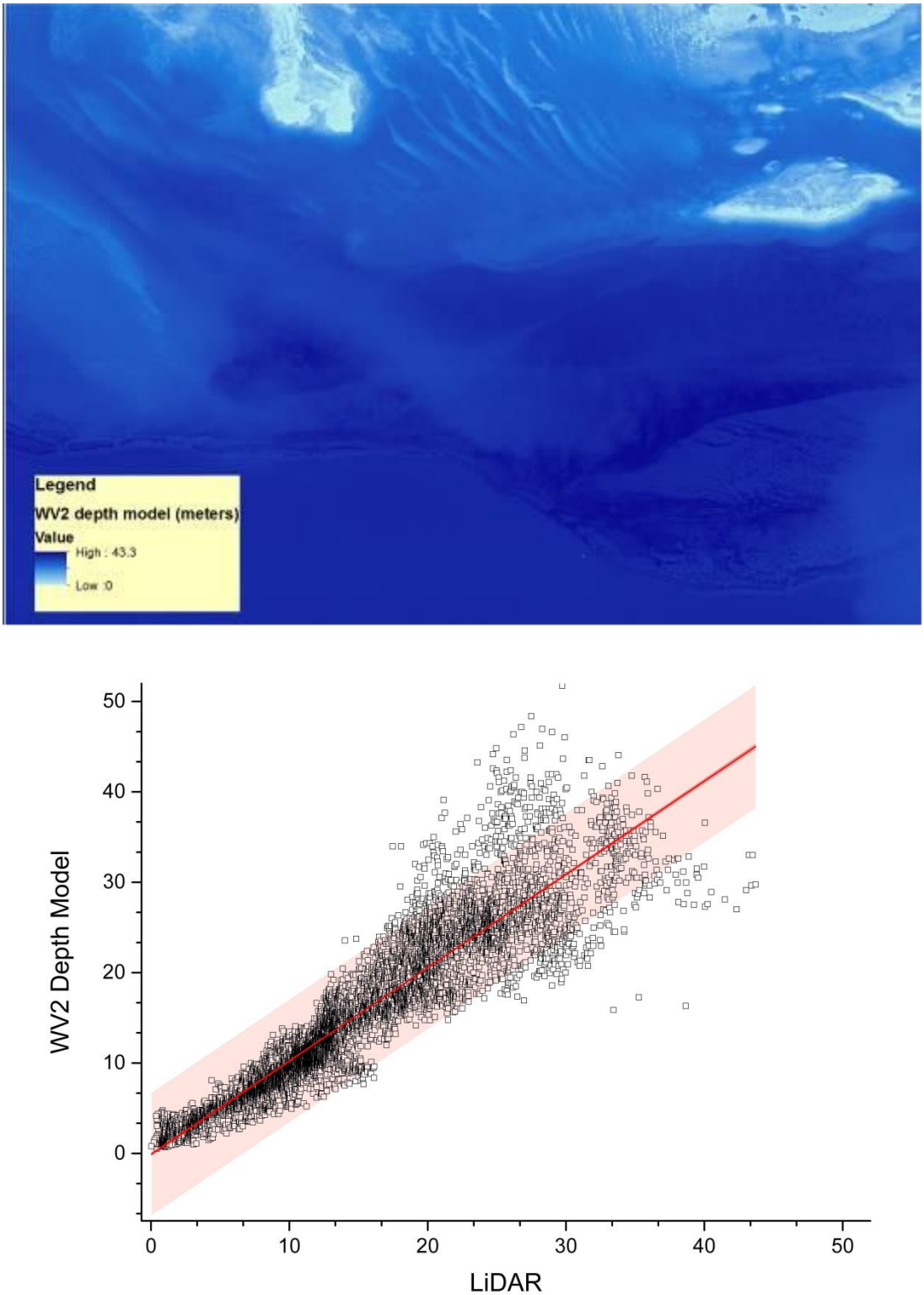

Figure 9: (Top) Per pixel depth estimation based on WV2 depth model for validation site within the WV2 image off southwestern Puerto Rico. (Bottom) Depth values for WV2 Depth Model and LiDAR Depths with 95% confidence and prediction bands. Note values dispersion after 20 meter depth.

Previous attempts for deriving depth in the study area were mainly produced with active sensors (e.g. SoNAR, LiDAR) where the final product was focused in coral reef mapping using Side Scan SoNAR (Prada et al. 2008), comparison of active sensors (LiDAR and multibeam SoNAR) for coral reef mapping (Costa et al. 2009), or to develop morphometrics from LiDAR to predict the diversity and abundance of fish and corals (Pittman et al. 2009).

The sensible depth is affected by the wavelength of the solar radiation used and by water clarity (Gao 2009). Torres-Madronero et al. (2009) performed a fusion of an AISA hyperspectral airborne camera and LiDAR SHOALS data using Lee's bio-optical model (Lee et al. 1999) to derived depths and other water and bottom optical properties from Cayo Enrique, located within our the study area of La Parguera Reserve. The use of Lee's bio-optical model for the depth estimation only retrieved values effectively to a depth of 6 meters. This was the only study that uses passive sensors to derive bottom depth in our study area. Some of the differences with our study worth noting are that Lee's only focused on a small offshore cay within the reserve; the use of Lee's bio-optical algorithm to derive depths; and the methods did not take into account the influence of atmospheric corrections in depth retrievals.

Other researchers have reported various depth ranges and values using band ratios. Coastal bathymetry was detected by McIntyre et al. (2006) using AVIRIS and multibeam SoNAR with an RMSE of 7.83 meters with depth most accurate from 10–14 meters. Lyzenga et al. (2006) reported an aggregate RMSE of 2.3 meters from a set of IKONOS images over a variety of conditions with an individual RMSE that varied from 1.65 to 2.31 meters. These areas were shallow areas with very high water clarity which contrast significantly with our study area.

Bathymetric data was evaluated by Mishra et al. (2005 and 2007) on a site specific model, using IKONOS and AISA images in Roatan Island, Honduras. This approach was the same used for our WV2 depth model and the polynomial model was found to provide the best correlation (R^2) of actual depth and estimated depth (Figure 5). The coefficient of determination for IKONOS image was 0.942 with an RMS error of 2.71 m. For the AISA image, the coefficient of determination was 0.943 with an RMS error of 2.873 m. Similar to our results, both the IKONOS and the AISA image the model overestimated depths beyond 20 meters.

Collin and Hench (2012) used WV2 to retrieve depth using Stumpf et al. (2003) model with various band combinations and reported an increase in depth penetration of 10 meters for their study area. Their model combination of purple, green, red and NIR2 (WV2 bands: 1,3,5,7) provided the greatest agreement with ground-truthing at actual 39 m (r = 0.7), 30 m (r = 0.65) and 1 m (r = 0.85). In accordance with our results, the analytical atmospheric correction (FLAASH) provided poorer results than no atmospheric correction and dark subtract correction.

The WV2 and tide charts depth with CSA atmospheric correction were used with a linear band algorithm modified from Lyzenga depth model and obtained a normalized RMSE of 0.229 meters for the waters of Singapore (Bramante et al. 2006). However, the maximum depth reached was only 2 meters, while for our study area; these depths exceeded the 20 meters. A dark subtract and sun glint correction were performed using a blue/green model from a WV2 image and LiDAR SHOALS for the waters of Florida and obtained a RMSE of 1.07 meters (Kerr 2010). As is the case with our imagery, this study presented the importance of atmospheric correction methods and deglinting should be applied to WV2 imagery prior to the development

of bathymetry maps in order to increase the accuracy of the final products. Additionally these methods, to an extent, reduce the errors in the data from the atmospheric influence to the reflectance values.

5. Conclusions

This study presents the first broad scale bathymetry map for La Parguera Reserve derived from a passive sensor and validated with an active sensor. Also, it provides a comprehensive evaluation of the different atmospheric corrections and the influence in the water depth retrievals. This study confirms that atmospheric correction methods should be applied to WV2 imagery prior to the development of bathymetric maps in order to increase the accuracy of the final product (Gao 2009; Kerr 2010; Collin and Hench 2012). Additionally, the selection of the atmospheric correction methods is extremely important in the performance of the depth model, even for simple blue/green ratios, and can be determinant based on the final product that will be developed from the imagery (i.e. benthic habitat map, depth retrievals).

In our case the best model was the one that use the Cloud Shadow Approach with a band 2/band 3 combination for the study area of La Parguera Reserve. This atmospheric correction proved successful even when it was modified due to cloud absence in the scene. Also, the use of simple band ratios provided the first high resolution bathymetry map for La Parguera Reserve from passive sensors. Using these methods, high resolution bathymetry can be obtained from passive sensor with minimum processing and leveraging from the information contained in the imagery. The dark subtract correction provided the second best results and proved to be an excellent first approximate for the correction of the atmospheric influence.

The WV2 depth model was based on the LiDAR SHOALS bathymetry an assumed these values as certain. According to Costa et al. (2009) the pixels with the largest depth differences (that were greater than the maximum allowable vertical error) occurred primarily along the shelf edge in water deeper than 35 meters, which corresponds approximately to the maximum limit of our model.

The WV2 depth model successfully retrieved depth values with a $r^2 = 0.70$ of the depth values to a depth range of 20 meters and the aggregated RMSE for that depth range was 1.43 meters. These results are a significant improvement when compared with other investigators using the same sensor, however, for depths >20 m the estimation error of the model increased noticeably as expected with passive sensors and a heterogeneous bottom composition. The availability of several WV2 bands in the visible region provides the opportunity to test different band combinations to retrieve bathymetry that when combined with a robust atmospheric correction allows meaningful depth to be retrieved even in areas with variable bottom composition.

6. References

Arnone, Robert, Marcel Babin, Andrew H Barnard, Emmanuel Boss, Jennifer P Cannizzaro, Kendall L Carder, F Robert Chen, et al. 2006. "Reports of the International Ocean-Colour Coordinating Group Remote Sensing of Inherent Optical Properties : Fundamentals , Tests of Algorithms , and Applications." *IOCCG Report 5* 5 (5): 126. doi:10.1006/jmbi.1998.2073.

Baban, Serwan M. J. 1993. "The Evaluation of Different Algorithms for Bathymetric Charting of Lakes Using Landsat Imagery." *International Journal of Remote Sensing*. doi:10.1080/01431169308954035.

Bramante, James F, Durairaju Kumaran Raju, and Sin Tsai Min. 2006. "Derivation of Bathymetry from Multispectral Imagery in the Highly Turbid Waters of Singapore ' S South Islands : A Comparative Study Background Atmospheric Correction." *Science*, 1–21.

Collin, Antoine, and James L. Hench. 2012. "Towards Deeper Measurements of Tropical Reefscape Structure Using the WorldView-2 Spaceborne Sensor." *Remote Sensing* 4: 1425–47. doi:10.3390/rs4051425.

Conger, Christopher L., Eric J. Hochberg, Charles H. Fletcher, and Marlin J. Atkinson. 2006. "Decorrelating Remote Sensing Color Bands from Bathymetry in Optically Shallow Waters." *IEEE Transactions on Geoscience and Remote Sensing* 44 (6): 1655–60. doi:10.1109/TGRS.2006.870405.

Costa, B. M., T. a. Battista, and S. J. Pittman. 2009. "Comparative Evaluation of Airborne LiDAR and Ship-Based Multibeam SoNAR Bathymetry and Intensity for Mapping Coral Reef Ecosystems." *Remote Sensing of Environment* 113 (5). Elsevier Inc.: 1082–1100. doi:10.1016/j.rse.2009.01.015.

Gao, J. 2009. "Bathymetric Mapping by Means of Remote Sensing: Methods, Accuracy and Limitations." *Progress in Physical Geography* 33 (1): 103–16. doi:10.1177/0309133309105657.

Gordon, H R, and O B Brown. 1974. "Influence of Bottom Depth and Albedo on the Diffuse Reflectance of a Flat Homogeneous Ocean." *Applied Optics* 13 (9): 2153–59. doi:10.1364/AO.13.002153.

Gordon, H. R., and A. Morel. 1983. "Remote Assessment of Ocean Color for Interpretation of Satellite Visible Imagery." *A Review of Lecture Notes on Coastal and Estuarine Studies Springer-Verlag New York*, 113 , New York.

Gregg, Watson W., and K. L. Carder. 1990. "A Simple Spectral Solar Irradiance Model for Cloudless Maritime Atmospheres." *Limnology and Oceanography* 35 (December): 1657–75. doi:10.4319/lo.1990.35.8.1657.

Kerr, Jeremy M. 2011. "Worldview-02 Offers New Capabilities for the Monitoring of Threatened Coral Reefs." *Dimensions and Directions of Geospatial Industry*, 18–21.

Kirk, J.T.O. 2011. "Light and Photosynthesis in Aquatic Ecosystems" Book (Third Edition): 638.

Lee, Z, K L Carder, C D Mobley, R G Steward, and J S Patch. 1999. "Hyperspectral Remote Sensing for Shallow Waters. 2. Deriving Bottom Depths and Water Properties by Optimization." *Applied Optics* 38 (18): 3831–43. doi:10.1364/AO.38.003831.

Lee, Zhongping, Kendall L. Carder, Robert F. Chen, and Thomas G. Peacock. 2001. "Properties of the Water Column and Bottom Derived from Airborne Visible Infrared Imaging Spectrometer (AVIRIS) Data." *Journal of Geophysical Research* 106: 11639. doi:10.1029/2000JC000554.

Lee, Zhongping, Brandon Casey, Robert Arnone, Alan Weidemann, Rost Parsons, Marcos J. Montes, Bo-Cai Gao, Wesley Goode, Curtiss Davis, and Julie Dye. 2007. "Water and Bottom Properties of a Coastal Environment Derived from Hyperion Data Measured from the EO-1 Spacecraft Platform." *Journal of Applied Remote Sensing* 1 (December): 011502. doi:10.1117/1.2822610.

Lyzenga, D R. 1978. "Passive Remote Sensing Techniques for Mapping Water Depth and Bottom Features." *Applied Optics* 17: 379–83. doi:10.1364/AO.17.000379.

Lyzenga, David R., Norman P. Malinas, and Fred J. Tanis. 2006. "Multispectral Bathymetry Using a Simple Physically Based Algorithm." *IEEE Transactions on Geoscience and Remote Sensing* 44 (8): 2251–59. doi:10.1109/TGRS.2006.872909.

Maritorena, Stéphane, André Morel, and Bernard Gentili. 1994. "Diffuse Reflectance of Oceanic Shallow Waters: Influence of Water Depth and Bottom Albedo." *Limnology and Oceanography* 39 (7): 1689–1703. doi:10.4319/lo.1994.39.7.1689.

Matthew, M.W., S.M. Adler-Golden, A. Berk, G. Felde, G.P. Anderson, D. Gorodetzky, S. Paswaters, and M. Shippert. 2002. "Atmospheric Correction of Spectral Imagery: Evaluation of the FLAASH Algorithm with AVIRIS Data." *Applied Imagery Pattern Recognition Workshop, 2002. Proceedings.* doi:10.1109/AIPR.2002.1182270.

McIntyre, Michelle L., David F. Naar, Kendall L. Carder, Brian T. Donahue, and David J. Mallinson. 2006. "Coastal Bathymetry from Hyperspectral Remote Sensing Data: Comparisons with High Resolution Multibeam Bathymetry." *Marine Geophysical Researches* 27: 129–36. doi:10.1007/s11001-005-0266-y.

Mishra, Deepak R, Sunil Narumalani, Donald Rundquist, and Merlin Lawson. 2005. "High-Resolution Ocean Color Remote Sensing of Benthic Habitats : A Case Study at the Roatan High-Resolution Ocean Color Remote Sensing of Benthic Habitats : A Case Study at." *Papers in the Earth and Atmospheric Sciences*, no. Paper 129.

Mishra, Deepak R., Sunil Narumalani, Donald Rundquist, Merlin Lawson, and R. Perk. 2007. "Enhancing the Detection and Classification of Coral Reef and Associated Benthic Habitats: A Hyperspectral Remote Sensing Approach." *Journal of Geophysical Research* 112. doi:10.1029/2006JC003892.

Mumby, P J, and a R Harborne. 1999. "Development of a Systematic Classification Scheme of Marine Habitats to Facilitate Regional …." *Biol Conserv* 88: 155–63.

NOAA, (2005). National Oceanic and Atmospheric Administration, National Ocean Service, Center for Operational Oceanographic Products and Services. Tides and Currents. Isla Magueyes Station.
http://tidesandcurrents.noaa.gov/waterlevels.html?id=9759110&timezone=GMT&units=standard&datum=MLLW&bdate=20051201&edate=20051231

NOAA, (2011). National Oceanic and Atmospheric Administration, National Ocean Service, Center for Operational Oceanographic Products and Services. Tides and Currents. Isla Magueyes Station.
http://tidesandcurrents.noaa.gov/waterlevels.html?id=9759110&timezone=GMT&units=standard&datum=MLLW&bdate=20111203&edate=20111206

Philpot, W D. 1989. "Bathymetric Mapping with Passive Multispectral Imagery." *Applied Optics* 28 (8): 1569–78. doi:10.1364/AO.28.001569.

Pittman, Simon J., Bryan M. Costa, and Tim a. Battista. 2009. "Using Lidar Bathymetry and Boosted Regression Trees to Predict the Diversity and Abundance of Fish and Corals." *Journal of Coastal Research* 10053 (2007): 27–38. doi:10.2112/SI53-004.1.

Prada, M. C., R. S. Appeldoorn, and J. a. Rivera. 2008. "The Effects of Minimum Map Unit in Coral Reefs Maps Generated from High Resolution Side Scan Sonar Mosaics." *Coral Reefs* 27: 297–310. doi:10.1007/s00338-007-0328-5.

Reinersman, P N, K L Carder, and F I Chen. 1998. "Satellite-Sensor Calibration Verification with the Cloud-Shadow Method." *Applied Optics* 37: 5541–49. doi:10.1364/AO.37.005541.

Stephenson, Darren and Sinclair, Mark. 2006. "Hydrographic Lidar: Data Acquisition and Processing Report."

Stumpf, Richard P, Kristine Holderied, and Mark Sinclair. 2003. "Determination of Water Depth with High-Resolution Satellite Imagery over Variable Bottom Types." *Limonology And Oceanography* 48: 547–56. doi:10.4319/lo.2003.48.1_part_2.0547.

Torres-Madronero, Maria C., Miguel Velez-Reyes, and James a. Goodman. 2009. "Fusion of Hyperspectral Imagery and Bathymetry Information for Inversion of Bioptical Models" 7473: 74730I – 74730I – 11. doi:10.1117/12.835896.

Chapter 3: High-Resolution Bottom Albedo and Water Optical Characterization of La Parguera Reserve from Active and Passive sensors.

Abstract:

The information retrieved from ocean color remote sensing can provide vital information of biological and biogeochemical processes in the oceans, including management of marine resources. The use of radiances measured by these sensors allows the analytical or semi-analytical retrieval of shallow-water bathymetry, bottom albedo and optical properties of the water column, and their contribution of each component to the remotely sensed signal. The Airborne Visible Infrared Image Spectrometer (AVIRIS) and WorldView-2 (WV2) sensors were used to derive water optical properties for La Parguera Reserve, southwestern Puerto Rico. These images were also combined with water depth from LiDAR data in order to perform a water column correction using Lee's semi-analytical algorithm, and to determine the optical bottom albedo. Additional field data was collected for absorption, backscattering and the coefficient of determination of downwelling irradiance (Kd). The values of image-derived absorption ($p=0.05$, $r^2=0.90$) and Kd ($p=0.05$, $r^2=0.96$) exhibited a strong correlation when compared with *in situ* values. A strong inverse relationship was found between distance from shore to increasing values of absorption ($p=0.07$, $r^2=0.71$) and this factor explained about 71% of the variation in absorption values for the time-series. For the AVIRIS image, bottom albedo values for sand, seagrass, and coral-gorgonians were in good agreement with *in situ* values for these substrates in both spectral shape and magnitude, and spectral absorption and reflectance features were only present after the water column correction. The LiDAR reflectivity was highly correlated to bottom albedo images from AVIRIS ($r^2 = 0.79$) and WV2 ($r^2 = 0.79$), and this correlation was further improved by removing the depth influence from the LiDAR reflectivity (AVIRIS, $r^2 =$

0.95; WV2, (r^2 = 0.94). This study represented the first integration of these algorithms to high resolution hyperspectral and multispectral imagery, correlated to a comprehensive time series of bio-optical properties, to develop bottom albedo images for La Parguera Reserve.

1. Introduction

The information retrieved from ocean color remote sensing can provide vital information of biological and biogeochemical processes in the oceans, and has many other applications including management of marine resources (Arnone et al. 2006). Coral reefs are one of the world's most biologically diverse ecosystems and can act as biological indicators of global climate change (Holden and LeDrew 2000; Eakin et al. 2010; McManus and Polsenberg 2004) that can be leveraged using remote sensing approaches (Mumby and Harborne, 1999). In recent years, studies on coral ecosystems by remote sensing have increased considerably, because of a greater availability of orbital and airborne sensors with very high spatial resolution in both multispectral (IKONOS and WorldView-2) (Purkis 2005; Collin and Hench 2012; Bramante et al. 2006), and hyperspectral (AVIRIS, AISA, CASI, and PHILLS) (Lee et al. 2001; Hochberg et al. 2003; Goodman et al. 2008; Mishra et al. 2007).

The signals measured by an airborne sensor represents a complex combination of absorption and scattering features from the atmosphere, spectral interactions at the air-water interface, absorption and scattering from the water column and reflectance from the benthic surface (Lobitz et al. 2008). The inherent optical properties (IOP) of water such as absorption and backscattering coefficients are the main physical agents governing the magnitude and spectral composition of the backscattered flux from the ocean surface (Maritorena 1996). This complexity complicates

retrievals of bottom depth and albedo by variations in water depth, bottom type and water attenuation by water column constituents (chlorophyll, suspended sediments, and color dissolved organic matter (Lee et al. 2001).

Several approaches have been developed to retrieve both the Apparent and Inherent Optical Properties (AOP/IOP) from the remotely sensed signal. The water upwelling radiance depends physically on the IOPs and solar input and this relationship for subsurface irradiance reflectance was first derived from radiative transfer calculations by Gordon and Brown (1974) and Morel and Prieur (1977). A proportionality factor *f/Q (sr-1)* was included that explained how the water reflectance is proportional to the backscattering coefficient and inversely proportional to the absorption coefficient. The R_{rs} is the remote sensing reflectance above the surface, the $Lu(0^-)/Ed(0^-)$ is the ratio of upwelling radiance to downwelling irradiance just below the surface, f/Q is the proportionality factor, and b_b/a is the ratio of backscattering to absorption (Equation 3-1).

$$R_{rs} = Lu(0^-)/Ed(0^-) = (f/Q)(b_b/a) \quad (3\text{-}1)$$

This proportionality factor varies from 0.084 to 0.15 sr-1 for nadir-viewing radiances, and depends how the backscattered light relates to the backscattering coefficient (Morel and Gentili 1993; Lee et al. 2001). The absorption and backscattering coefficients also provides complementary information on the water composition, since the first is affected by the presence of both suspended and dissolved material in water, while the later represents the concentration (to first order) of organic and inorganic suspended particles, and bubbles (Arnone et al. 2006).

The use of radiances measured by these passive sensors allows the analytical or semi-analytical retrieval of shallow-water bathymetry, bottom albedo and optical properties of the water column, and their contribution of each component to the remotely sensed signal (Lee et al., 1999). Algorithms have been used extensively to correct these limitations of the attenuation caused by water to the spectral signal (Maritorena 1996; Mumby et al. 1997; Holden and LeDrew 2000; Mishra et al. 2007). These models (e.g., Hydrolight) allow corrections of attenuation of light in seawater, by treating the benthic habitat as a lambertian surface at a known depth, but they are specifically designed for analysis and modeling of a single spectrum and not for full-image, per-pixel correction of hyperspectral data (Lee et al. 2001; Hochberg et al. 2003; Goodman et al. 2008; Mishra et al. 2007). These semi-analytical approaches are based on simple approximations of the remote sensing reflectance, and they use the relationship between the oceanic constituents and the IOPs upon which to base the inversion (Gordon 1989; Morel 1988).

The advancement of airborne laser bathymetry technology (i.e. LiDAR) has allowed the transformation of reflectivity and depth derived from these sensors into classified images of bottom types (Collins, et al. 2007). Traditionally, LiDAR was used primarily to derived depth (Gao 2009), but a reflectivity product can be extracted by integrating the entire waveform (Collins et al. 2007). This reflectivity product can then be processed (Stephenson and Sinclair 2006), analyzed using multivariate statistics to delineate benthic features (Collin et al. 2011), evaluated for shape and amplitude of the LiDAR waveforms to extract the attenuation of the water and the bottom reflectivity (Wang and Philpot 2007) and fused with passive hyperspectral data (Tuell et al. 2005).

Data fusion techniques combine data from multiple sensors and related information, to achieve improved accuracies and more specific inferences than could be achieved by the use of a single

sensor alone (Hall and Llinas 1997). Active sensors like LiDAR, has been used primarily for high-resolution bathymetry and recently for estimation of bottom composition (Wang and Philpot 2007). Fusion of hyperspectral and LiDAR data has been used in land cover classification taking advantage of both the high resolution spectral signature captured by the hyperspectral spectrometer and the detailed sampling of the spatial information by the LiDAR system (Torres-Madronero et al. 2009).

In marine and coastal environments, several examples present the fusion of active and passive sensors data and products. Lee (2003) showed the use of multiple sensors by combining pseudoreflectance derived from SHOALS data to classify sea bottom, which was then fused with an AVIRIS image classification. This fusion was done both at the pixel-level (i.e. data-level), and at the decision-level, combining the benthic classifications derived from the water-corrected AVIRIS and SHOALS datasets, using the Dempster-Shafer evidence combination approach. Tuell et al. (2005) described a process to invert radiative transfer model from hyperspectral image using the depth, reflectance and attenuation parameter derived from SHOALS data as initialization parameters for the inversion.

Results presented by Torres-Madronero et al. (2009) with simulated and real hyperspectral imagery showed significant improvement in accuracy of bottom abundances that can be retrieved by the incorporation of high resolution LiDAR bathymetry, by providing an additional constraint on the inversion algorithms. NOAA used Exelis ENVI software to extract and fuse information from sonar, LiDAR and optical imagery so that sea floor depths and habitats could be determined (Exelis Visual Information Solutions 2011).

The purpose of this study was to derive water optical properties from an AVIRIS hyperspectral image and a WV2 multispectral image, combined with water depth from LiDAR data in order to determine the optical bottom albedo and ultimately to map the spatial distribution of benthic habitats for shallow ocean waters in southwestern Puerto Rico. These water optical properties were validated with *in situ* measurements and a correlation was established with the LiDAR intensity image. The LiDAR intensity image was used to determine bottom albedo.

1.1 Objectives

The purpose of this study was to develop a high-resolution bottom albedo map of La Parguera Reserve from active and passive sensors that includes the characterization of the inherent and apparent optical properties, and the application of a water column correction to the sensor data.

The specific objectives are to:

1. Analytically derive bottom albedo using AVIRIS and WV2 data, after an atmospheric and water column correction using high-resolution bathymetry.
2. Validation of IOP/AOP and bottom albedo derived analytically from the AVIRIS and WV2 image with *in situ* IOP/AOP and bottom albedo.
3. Development of a relationship between bottom albedo and LiDAR intensity data (reflectivity).

2. Methods and Materials

2.1 Image Preprocessing

The imagery and data were preprocessed first to enable spatial correlations before further analysis. These corrections included data resampling, radiometric corrections to transform data from at sensor radiance to remote sensing reflectance, and atmospheric corrections to determine the contribution of the atmosphere to the signal.

2.1.1 AVIRIS

Data preprocessing was done using the Exelis ENVI 5.0 computer program. The AVIRIS image was evaluated for data gaps and a subset of the image was made based on the La Parguera Reserve polygon. The original spatial resolution of the AVIRIS image was 3.1 meters, so the image was resampled to 4 meters to match the spatial resolution of the LiDAR bathymetry image. Describe the date, flying altitude, platform and other details of the AVIRIS data used.

2.1.2 LiDAR SHOALS bathymetry image

Data processing for the LiDAR image was done using Exelis ENVI 5.0 computer program. The LiDAR image was evaluated for data gaps and a subset of the image was made based on the La Parguera Reserve polygon. The co-registration was done using the LiDAR image as a base map for the other co-registrations. A total of 40 points were used as ground control points for the registration and the total RMSE for the co-registration was 0.5 meters.

2.1.3 LiDAR SHOALS reflectivity image

Data processing for the LiDAR reflectivity image was done using Exelis ENVI 5.0 computer program. A subset of the image was created using the La Parguera Reserve polygon. The

AVIRIS image was used as the base image for the co-registration with the LiDAR reflectivity image and both were set to the coordinate system NAD 1983 State Plane Puerto Rico USVI (FIPS 5200). A total of 40 points were used as ground control points for the registration and the LiDAR reflectivity image was warped to match the AVIRIS image. The total RMSE for the co-registration was 0.5 meters.

2.2 Ancillary data

The images were corrected for fluctuations in tide readings and these were measured at the Magueyes Island Tide Station (Station ID 9759110) in La Parguera, Lajas, Puerto Rico (NOAA, Tide and Currents, 2005). The WV2 imagery was captured in December 4, 2011 (15:25 GMT) and tide reading for this station was 0.249 meters at MLLW (15:24 GMT) (NOAA, Tide and Currents, 2011). The LiDAR SHOALS bathymetry data was processed and corrected for errors in position and tidal changes (Stephenson and Sinclair 2006).

2.3 Atmospheric corrections

An essential step in multispectral and hyperspectral remote sensing of ocean water is to correct for atmospheric effects. To analytically derive water and/or bottom properties from any satellite ocean-color data, the first step is to get high-quality spectral remote-sensing reflectance (Rrs) that contains water and/or bottom information (Lee et al. 2007). There are several methods for atmospheric correction currently available for both multispectral and hyperspectral imagery. For the AVIRIS image the atmospheric correction, TAFKAA was used. Additional preprocessing was applied to the image for suppressing the impacts of the stray-light anomaly, correction of an

unexplained edge decay feature, suppression of sun glint (Lobitz et al. 2008). The WV2 image was atmospherically corrected using the Cloud Shadow Approach (CSA) (Lee et al. 2007).

2.4 Bottom albedo and water column optical properties from AVIRIS and WV2 image

The signals measured by an airborne sensor represents a complex combination of absorption and scattering features from the atmosphere, spectral interactions at the air-water interface, absorption and scattering from the water column and reflectance from the benthic surface albedo (Lobitz et al. 2008). Previous investigators used AVIRIS imagery and other airborne spectral sensors to obtain water column properties based on their spectral response (Lee et al. 1999; Lee et al. 2001; Lee 2003; Mishra et al. 2007). Several methods were used to derive water optical properties from the AVIRIS and WV2 images and water depth from the LiDAR data in order to determine the optical bottom albedo. The individual parameters were calculated based on various methods and models described below.

2.4.1 Inherent Optical Properties (IOP)

2.4.1.1 Absorption

The absorption obtained through inversion is the total absorption coefficient, a_{tot}, namely, the sum ($a_w + a_p + a_y$) of the absorption coefficients by water, particles, and dissolved yellow substance, respectively (Morel et al. 2007).

The total absorption $a_{tot}(\lambda)$ can be derived by modification from Mishra et al. (2007) to the equation from Austin and Petzold (1986) as:

$$a_{tot}(\lambda) = M(\lambda)[a(485) - a_w(485)] + a_w(\lambda), \quad (3\text{-}2)$$

where M is a statistically derived coefficient taken from Austin and Petzold (1986), $a(485)$ is the total absorption coefficient at 485nm and $a_w(485)$ is the pure water absorption coefficient at 485nm (Pope and Fry 1997).

To obtain the $a(485)$, we rewrite Equation 3-2 to:

$$a(485) = [a(440) - a_w(440)] / M(440) + a_w(485) \quad (3\text{-}3)$$

The $a(440)$ used in Equation 3-3 can be empirically determined over deep water using the following approximation by Lee et al. (1998):

$$a(440) = 10^{-0.619-19.69\ (\log_{10}[Rrs(485)/Rrs(560)])\ +0.0790\ (\log_{10}[Rrs(485)/Rrs(560)])2} \quad (3\text{-}4)$$

where Rrs(485) and Rrs(560) are the remote sensing reflectance at 485 nm and 560 nm, respectively.

2.4.1.2 Backscattering

The total backscattering coefficient (b_b) can be expressed as the backscattering from particles (b_{bp}) plus the backscattering of the water molecules (b_{bw}) (Morel 1974).

$$b_b(\lambda) = b_{bp}(\lambda) + b_{bw}(\lambda) \quad (3\text{-}5)$$

The values of scattering of pure seawater were obtained from the term presented by Twardowski et al. (2007), where the scattering values of pure seawater from Buiteveld et al. (1994) were

increased by 30% to compensate for the salinity enhancement on scattering (Morel 1974). These values are considered the best estimates of pure seawater scattering (Twardowski et al. 2007). These were computed for each wavelength to obtain the backscattering coefficient (half of the scattering coefficient) for optically pure seawater (Morel 1974).

The backscattering coefficient was expressed to approximate the backscattering produced by particles in the form proposed by Morel (1988),

$$b_b(\lambda) = b_{bp}(660)\ (660/\ \lambda)^{\eta} + b_{bw}(\lambda) \qquad (3\text{-}6)$$

where the backscattering of particle is evaluated at 660nm, and η is a coefficient which the values range from 0.00 to 3.00 for ocean particles. The values selected for this coastal study was 0.5, because we considered this a Case-1 waters (Mishra et al. 2007).

To obtain the $b_{bp}(660)$ we used band 28 (664nm) of the AVIRIS image with the assumptions of no bottom influence's to the upwelling signal, absorption is dominated by water molecules, and relatively clear deep water (Mishra et al. 2007; Morel and Gentili 1993). Based on this assumptions, $b_{bp}(660)$ can be expressed as:

$$b_{bp}(660) \approx (a_w(660) / 0.05)\ \mathrm{Rrs}\ (660) \qquad (3\text{-}7)$$

where a_w is the pure water absorption coefficient at 660nm (Pope and Fry 1997).

2.4.2 Water column correction and Bottom albedo

2.4.2.1 Bottom albedo

The biggest challenge for mapping the benthic environment is removing the attenuation effects of the water column (Lee 2003). Remote sensing reflectance (Rrs) is an apparent optical property that it is defined as the ratio of water leaving radiance (Lw) to downwelling irradiance (E_d), and it is controlled by the absorption and scattering properties of the constituents in the water column [$R_{rs}^{w}(\lambda)$] and the bottom albedo [$R_{rs}^{b}(\lambda)$].

$$R_{rs}(\lambda) = R_{rs}^{w}(\lambda) + R_{rs}^{b}(\lambda) \quad (3\text{-}8)$$

These terms were approximated by Lee et al. (1994, 1998, 1999) in terms of the IOP influence in the R_{rs};

$$R_{rs}^{w}(\lambda) \approx 0.05[b_b(\lambda) / a(\lambda) + b_b(\lambda)] \left[1 - e^{-3.2[a(\lambda) + bb(\lambda)]Z}\right] \quad (3\text{-}9)$$

$$R_{rs}^{b}(\lambda) \approx 0.173\, \rho(\lambda)\, e^{[-2.7a(\lambda) + bb(\lambda)]Z} \quad (3\text{-}10)$$

where z is the depth of the water in meters taken from the LiDAR image and $\rho(\lambda)$ is the bottom albedo.

A 100 x 100 pixel window was created that represented deep water pixels (Figure 1). These deep water pixels values were used in the models to derive absorption and backscattering coefficients and represents optically deep areas with little upwelling signal in the visible bands. Modeled values of $a(\lambda)$ and $b_b(\lambda)$ were derived for each AVIRIS and WV2 bands and were assumed to be constant for the entire scene. The bands used in the models, 485nm, 560nm, and 660nm, represent the AVIRIS band 9 (482nm), band 17 (559nm) and band 28 (664nm), while the WV2

bands used were band 2 (480nm), band 3 (555nm) and band 5 (665nm). The water optical parameters and water depth were used to derive the influence of the water column and the bottom albedo image using image processing techniques in Exelis ENVI 5.0 software.

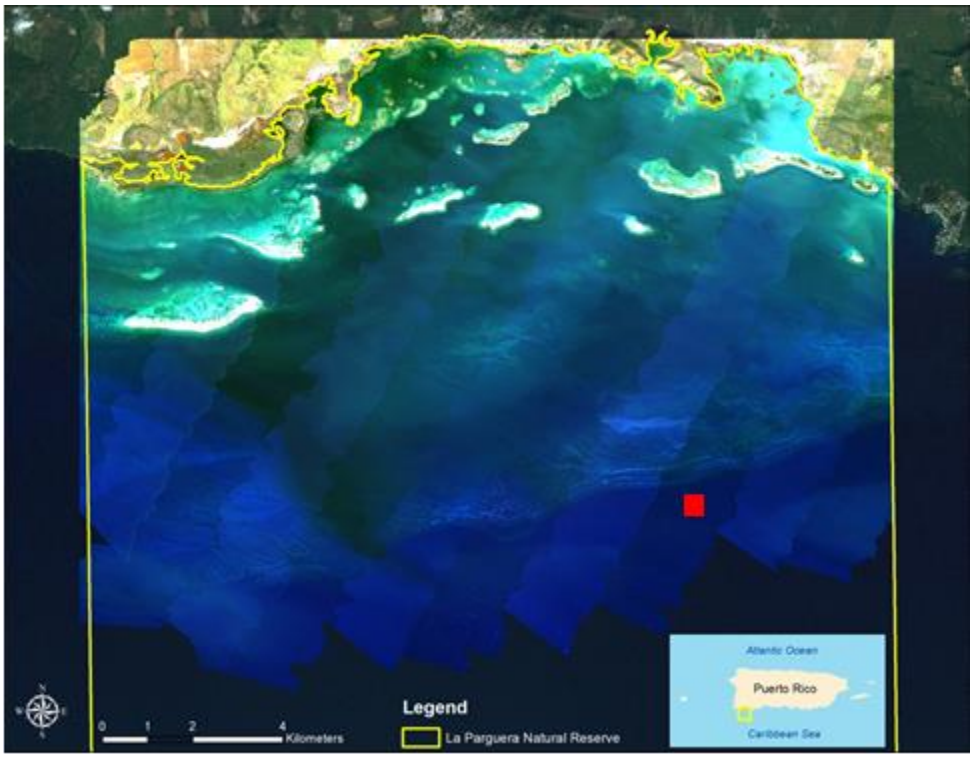

Figure 1: AVIRIS image of the study area of La Parguera Reserve, southwestern Puerto Rico that includes the 100x100 pixel window (red box).

2.4.2.2 Image derived Kd

The diffuse attenuation $K_d(\lambda)$ is an important apparent optical property (AOP) that provides information about the attenuation of the spectral downwelling solar irradiance $E_d(z,\lambda)$ with depth z in water (Suresh et al. 2012). *In situ* K_d values were obtained for different sites during the AVIRIS mission (Guild et al. 2008). $K_d(\lambda)$ can be modeled as a function of the inherent optical properties, absorption and backscattering, and dependent on the solar zenith angle (Kirk 2011).

According to Lee et al. (2007) the K_d can be modeled using the radiative transfer equations given as:

$$K_d = m_o\, a(\lambda) + m_1\, [1-m_2\, e^{-m_3 a(\lambda)}]\; b_b(\lambda) \qquad (3\text{-}11)$$

Where m_0, m_1, m_2, m_3 are modeled using Hydrolight software and the values depend on depth and solar zenith and the values of absorption and backscattering. These imaged derived values were compared to the *in situ* values and were used to estimate bottom albedo. The solar zenith angle was estimated at 45 degrees based on the AVIRIS mission. The absorption and backscattering values were modeled from the AVIRIS and WV2 image (Equation 3-2 and 3-6, respectively), while the coefficients in the model were derived from Hydrolight simulations for Case-1 waters (m_0=0.005, m_1=4.18, m_2=0.52) (Lee et al. 2007).

2.4.2.3 Bottom albedo

The imagery products from the water column correction were evaluated to obtain images that contain only information from the bottom substrate. The above water Rrs spectra in shallow waters contains information of the interactions of photons with the water column constituents and the upwelling radiance from the benthic habitats (Maritorena et al. 1994; Mishra et al. 2007). According to Purkis (2005), if the apparent optical properties and thickness of the water column are known, it is possible to retrieve values of substrate reflectance from a reflectance measurement made on the water surface given the water depth, the attenuation coefficient and the reflectance of optically deep water. The equation for bottom reflectance (R_b) is:

$$R_b = (1/0.54\; R_{rs\,(z=a)} - (1- e^{-2kz})R_w) / e^{-2kz} \qquad (3\text{-}12)$$

where z is the water depth, k is the spectral attenuation coefficient and R_w is the reflectance of optically deep water. The substrate reflectance (R_b) was derived using 1) the high-resolution depth values provided by the LiDAR bathymetry, and 2) the attenuation coefficients collected *in situ* during the AVIRIS mission for selected sites in La Parguera Reserve. Values for attenuation coefficients were derived from the AVIRIS image using the techniques presented in section *2.4.2.2* (Image-derived K_d) of this document. These derived values were compared with the *in situ* values of the attenuation coefficient and used to estimate bottom reflectance for La Parguera Reserve using image processing techniques in Exelis ENVI 5.0 software.

2.4.2.4 LiDAR Reflectivity Albedo

The use of LiDAR have been extended from bathymetric data for nautical charting applications, to enhancing the data with complementary datasets, such as reflectivity (Costa et al. 2009). This reflectivity pulse value is a measure of the amount of energy reflected from the seabed for each individual laser pulse at the wavelength of the laser (532nm, green/blue). This reflectivity value, is the ratio between the received energy normalized for the modeling losses through the water-column at the water/air interface, and the transmitted energy (Collins et al. 2007).

The LiDAR reflectivity for La Parguera Reserve was processed to create an 8-bit, 5×5 meter raster surface (Costa et al. 2009). Since only the raster surface was available for analysis, this surface was compared with bottom albedo derived from AVIRIS and WV2 images after water column correction, and no waveform analysis of the pulse was performed. This fusion analysis at the pixel level helped to determine which bands of bottom albedo from AVIRIS and WV2 were correlated to the LiDAR reflectivity.

2.4.3 In situ values of R_{rs}, IOP's and K_d

2.4.3.1 Kd

Water column light attenuation coefficients (Kd) were calculated from the average of three to five spectra from a Spectralon reference panel at three depths using a GER 1500 (Spectra Vista Corp.) handheld spectroradiometer in an underwater housing and were collected for different bottom types that coincided with passing of the AVIRIS sensor over our study area (Guild et al. 2008). These values were compared with the water column corrected spectra (R_{rs}) obtained from the AVIRIS and WV2 image.

2.4.3.2 IOP's

The *in situ* values of the IOP's were obtained during various bio-optical missions that include some sites in our study area collected monthly from October 2007 to September 2009. These data were collected throughout different seasons to account for temporal variability (Armstrong et al. 2012). The absorption coefficients were obtained using an AC-9 (WetLabs) that measure the beam attenuation coefficient, c (λ), and absorption coefficient, a (λ), in nine wavelengths. The backscattering (b_b) was measured at six wavelengths using the Hydroscat 6 (Hobi Labs) instrument. These measurements were compared with values derived from the AVIRIS and WV2 images.

2.4.3.3 Additional Field Data

Bottom albedo values and benthic habitats of the study area were also identified in various field campaigns in 2013 and 2014. The data collected included upwelling radiance and downwelling irradiance obtained using the OCR-507 submersible radiometers (Satlantic), surface remote

sensing reflectance (GER 1500), inherent optical properties (absorption, scattering and beam attenuation) by AC-9 (WetLabs) and HydroScat-6 (Hobi Labs), and a CTD sensor (Seabird). Benthic habitats were identified using a high resolution Delta Vision HD underwater camera with DVR Additional drop camera samplings were used for accuracy assessment and ground validation of the benthic habitats maps.

3. Results

3.1 Image preprocessing

The original images were pre-processed and the final products consisted of AVIRIS and WV2 atmospherically corrected and co-registered images.

3.2 Bottom albedo and water column optical properties.

3.2.1 Absorption and Backscattering

Absorption and backscattering were derived using the equation described in sections *2.4.1.1 and 2.4.1.*2 using equations 3-2 and 3-5, respectively. The deep-water pixels previously selected from the AVIRIS and WV2 images were used in the models to derive these coefficients (Table 1).

(a) World View 2						
Band	**λ, m^{-1}**	**a (λ), m^{-1}**	**a_w (λ), m^{-1}**	**b_b (λ), m^{-1}**	**b_{bw} (λ), m^{-1}**	**M (λ)**
1	425	0.3011	0.0048	0.0057	0.0053	1.6550
2	480	0.2088	0.0127	0.0034	0.0033	1.0955
3	545	0.1602	0.0511	0.0028	0.0020	0.6094
4	605	0.0347	0.2577	0.0024	0.0013	0.4983
5	660	0.0541	0.4100	0.0021	0.0009	0.7301

(b) AVIRIS						
Band	**λ, m^{-1}**	**a (λ), m^{-1}**	**a_w (λ), m^{-1}**	**b_b (λ), m^{-1}**	**b_{bw} (λ), m^{-1}**	**M (λ)**
1	405	0.3506	0.00530	0.0049	0.0033	1.7463
2	414	0.3628	0.00444	0.0045	0.0029	1.7312
3	424	0.3474	0.00478	0.0043	0.0027	1.6550
4	434	0.3292	0.00530	0.0040	0.0024	1.5648
5	443	0.3107	0.00696	0.0038	0.0022	1.4673
6	453	0.2918	0.00969	0.0036	0.0020	1.3627
7	462	0.2808	0.01005	0.0036	0.0020	1.3077
8	472	0.2589	0.0109	0.0034	0.0018	1.1982
9	482	0.2399	0.0131	0.0032	0.0016	1.0955
10	491	0.2220	0.0150	0.0031	0.0015	1.00
11	501	0.2092	0.0204	0.0030	0.0014	0.9118
12	511	0.2045	0.0325	0.0028	0.0012	0.8310
13	520	0.1978	0.0409	0.0028	0.0012	0.7578
14	530	0.1867	0.0434	0.0027	0.0011	0.6924

15	539	0.1789	0.0474	0.0026	0.0010	0.6350
16	549	0.1778	0.0565	0.0025	0.0009	0.5860
17	559	0.1749	0.0619	0.0024	0.0008	0.5457
18	568	0.1737	0.0672	0.0023	0.0007	0.5146
19	578	0.1858	0.0836	0.0023	0.0007	0.4935
20	588	0.2222	0.1220	0.0023	0.0007	0.4840
21	597	0.2940	0.1925	0.0023	0.0007	0.4903
22	607	0.3660	0.2629	0.0022	0.0006	0.4983
23	617	0.3788	0.2707	0.0021	0.0005	0.5223
24	626	0.4005	0.2834	0.0021	0.0005	0.5659
25	636	0.4395	0.3012	0.0021	0.0005	0.6683
26	646	0.4740	0.325	0.0021	0.0005	0.7201
27	655	0.5226	0.371	0.0020	0.0004	0.7323
28	665	0.5781	0.429	0.0004	0.0004	0.7205
29	672	0.5931	0.448	0.0004	0.0004	0.7008
30	682	0.6073	0.478	0.0004	0.0004	0.6245
31	692	0.6395	0.538	0.0004	0.0004	0.4901
32	701	0.6838	0.624	0.0004	0.0004	0.2891

Table 1: Absorption and backscattering coefficients derived from the WV2 (a) and the AVIRIS image (b) (100x100 pixel window). Absorption of pure water [$a_w(\lambda)$] derived from Pope and Fry (1997); the backscattering coefficient of pure seawater [$b_{bw}(\lambda)$] is half the scattering coefficient. The scattering coefficients for optically pure seawater were the values proposed by Buiteveld et al. (1994), increased by a factor of 1.30 to account for the presence of salt (Morel et al. 2007; Twardowski et al. 2007). M is a statistically derived coefficient taken from Austin and Petzold (1986).

Apparent Optical Properties were collected during a monthly field campaigns from May 2007 to August 2009 for selected sites in La Parguera Reserve (Figure 2). These values were obtained from the ac-9 and the HydroScat-6 sensors using the bio-optical package and compared to the values obtained from the AVIRIS image. The stations have variable bottom types with depth ranging from 1.5 to 18 meters (Figure 2, derived from Armstrong et al. 2012).

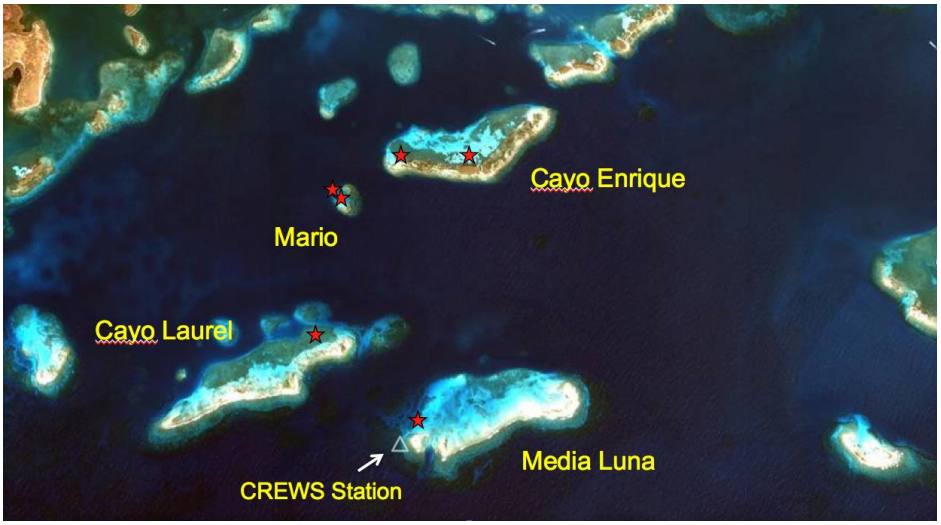

Station	Reef	Bottom Type	Depth (m)	Distance from shore (km)
1	Media Luna	Sand/Coral	3.0	3.9
2	Laurel	Seagrass	2.0	3.3
3	Mario Shallow	Sand/Coral	4.5	2.3
4	Mario Deep	Mud	18.0	2.3
5	Enrique West	Seagrass	2.0	2.1
6	Enrique East	Sand	1.5	2.1

Figure 2: Selected sites for field campaign to collect IOP/AOP in La Parguera Reserve. The sites location (red star) and the ICON CREWS station (triangle) is included for reference. The associated table presents site description parameters.

Figure 3 shows the values of (a) absorption and (c) attenuation that were obtained from the ac-9 instrument for the selected stations, the values of (b) scattering were derived from b = c-a, and the values of backscattering (b_b) were obtained from the HydroScat-6 sensor for the selected stations.

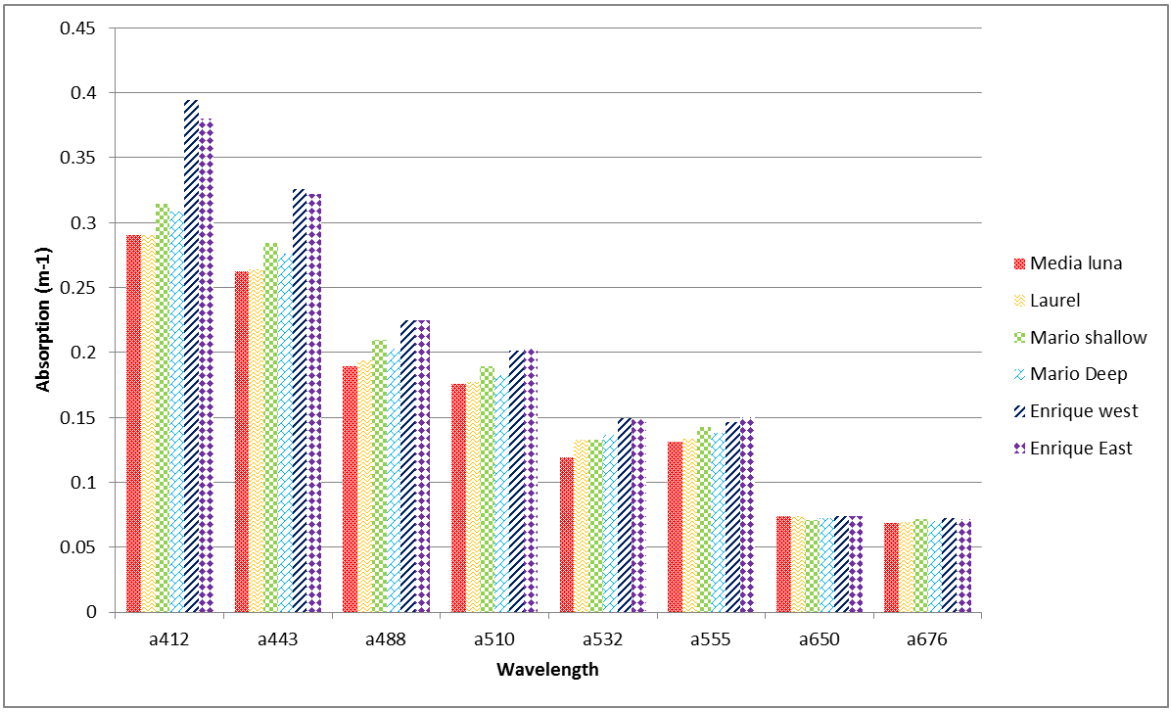
0.45
0.4
0.35
0.3
0.25
0.2
0.15
0.1
0.05
0
Absorption (m-1)
a412
a443
a488
a510
a532
a555
a650
a676
Wavelength
Media luna
Laurel
Mario shallow
Mario Deep
Enrique west
Enrique East

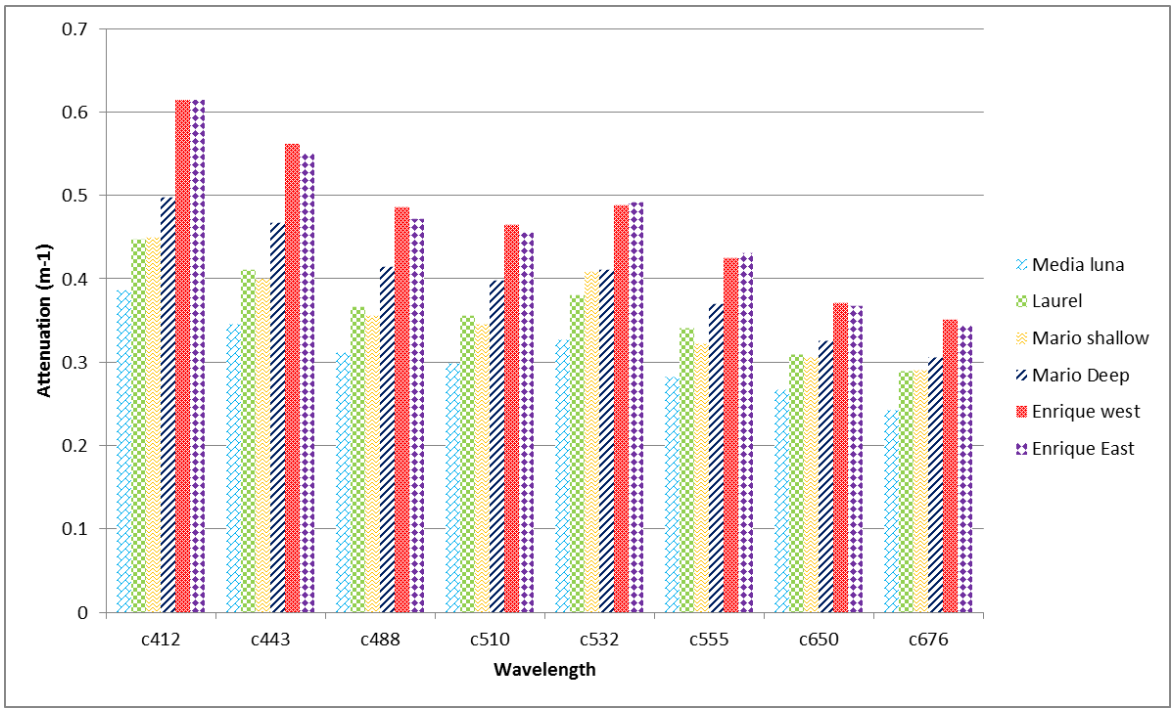
0.7
0.6
0.5
0.4
0.3
0.2
0.1
0
Attenuation (m-1)
c412
c443
c488
c510
c532
c555
c650
c676
Wavelength
Media luna
Laurel
Mario shallow
Mario Deep
Enrique west
Enrique East

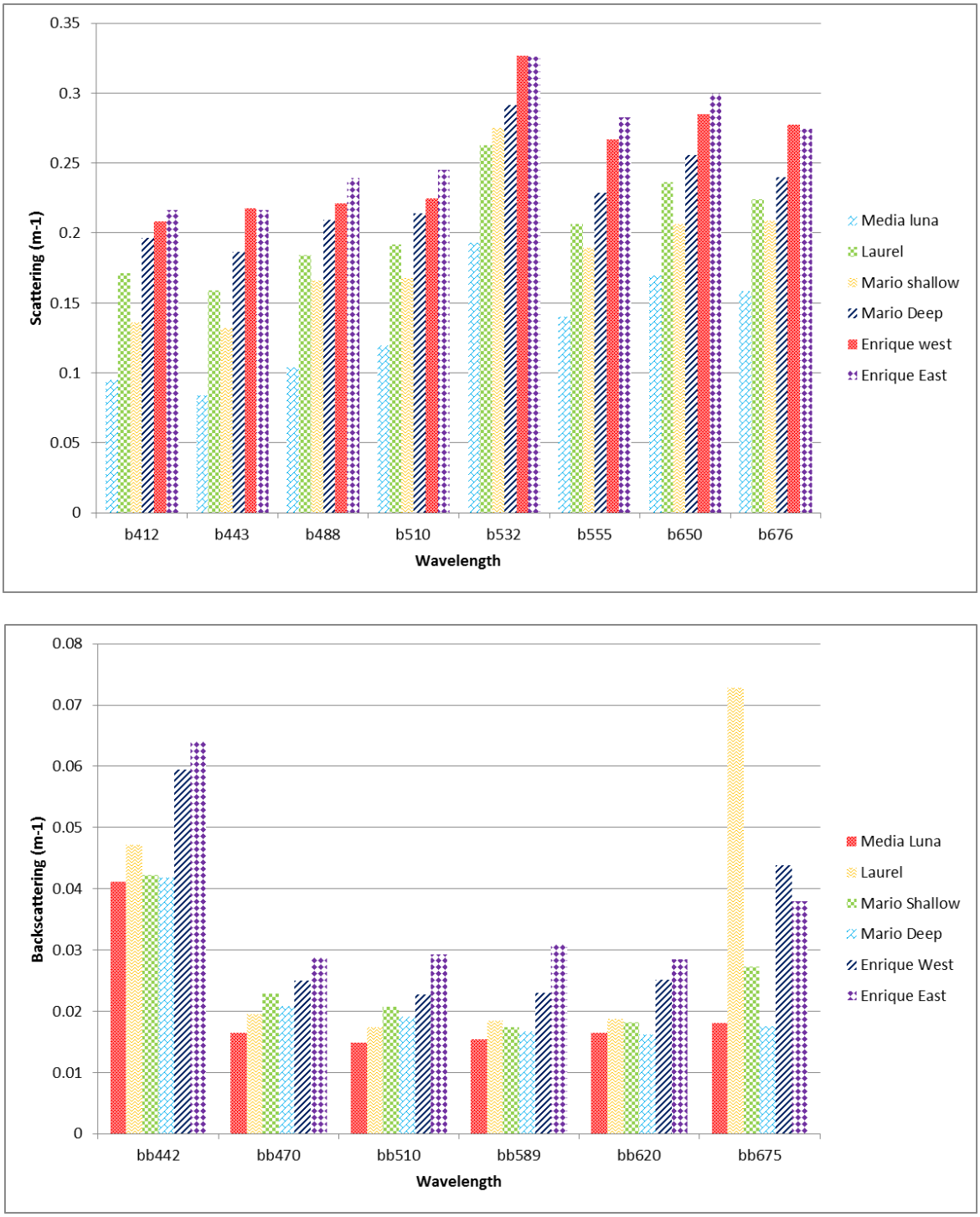

Figure 3: Median values of absorption (a), scattering (b) and attenuation (c) collected using the ac-9 instrument. The median values of backscattering (d) were collected using the hydroscat-6.The x-axis shows the different wavelengths collected (nanometers) by the instruments.

These *in situ* values were compared to the modeled derived values obtained from the AVIRIS and WV2 images. Only values of (a) absorption and (b_b) backscattering were derived from the image. The values were matched to the nearest AVIRIS and WV2 spectral channels (Figure 4).

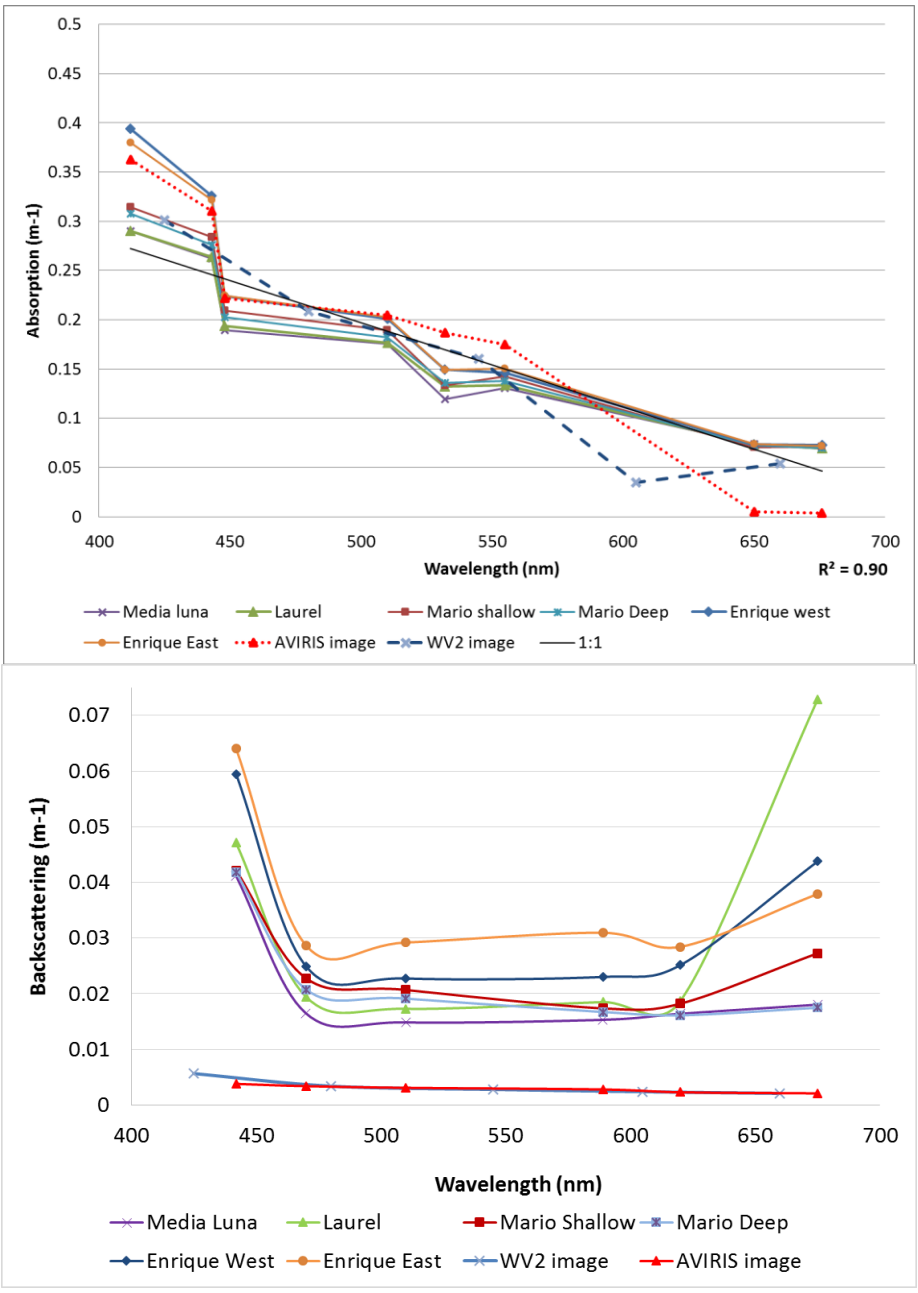

Figure 4: Comparison of absorption (λ) values (Top), and backscattering b_b (λ) values (Bottom) modeled from AVIRIS image (red-solid line) and WV2 image (blue-dash line). These modeled values were compared with in situ values for selected sites in La Parguera Reserve during bio-optical sampling campaign. In situ values are median monthly values obtained from May 2007 to August 2009 bio-optical sampling.

Another factor that influences the backscattering value is the presence of inorganic particles and CDOM from re-suspension of bottom sediments, nutrient input and wave action (Morel 1974; Twardowski et al. 2007). The Hydroscat-6 provided both (b_{bp}) and (b_{bw}) so each component was evaluated individually to quantify the contribution of particles for each station based on depth, substrate and distance from shore (Figure 5).

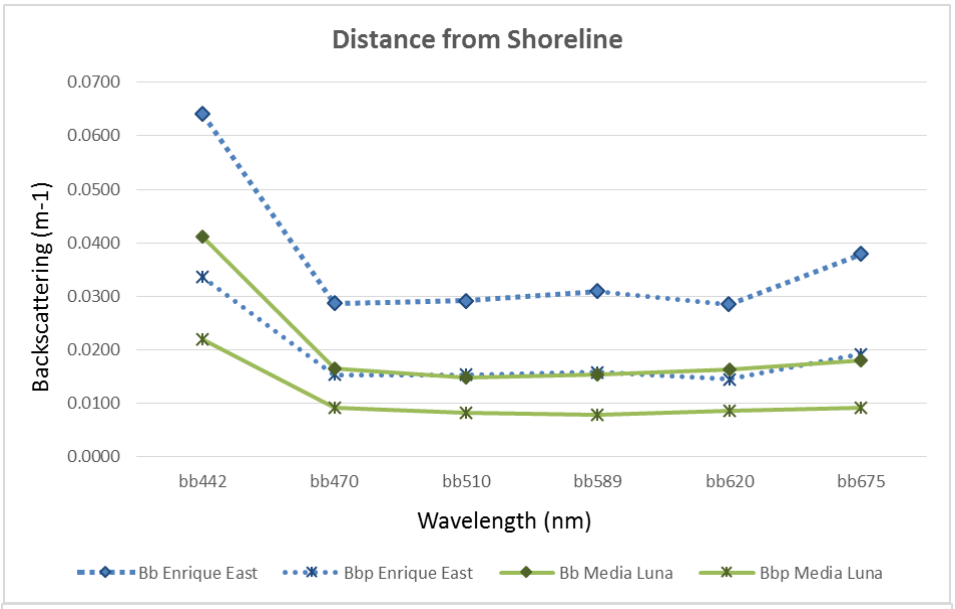

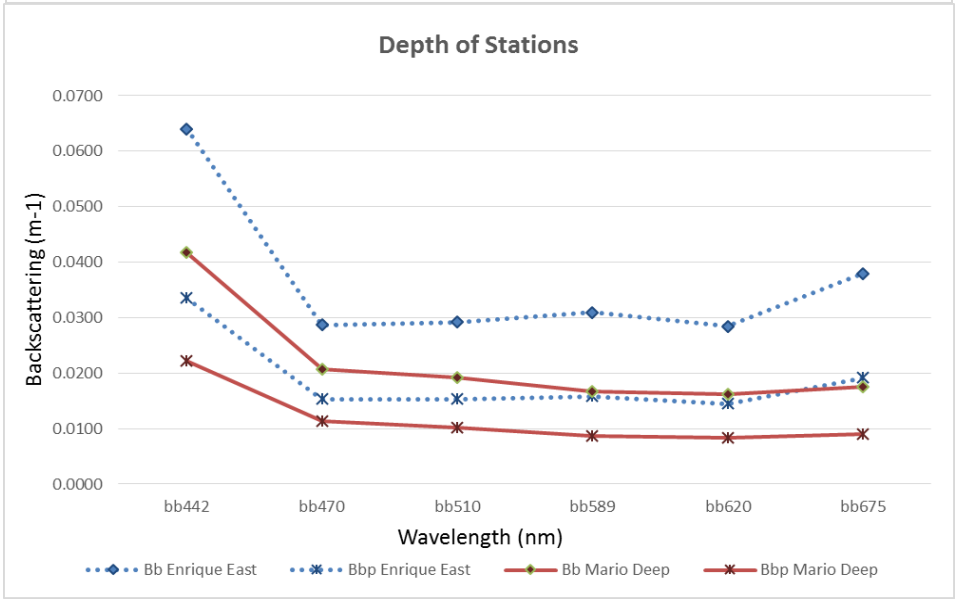

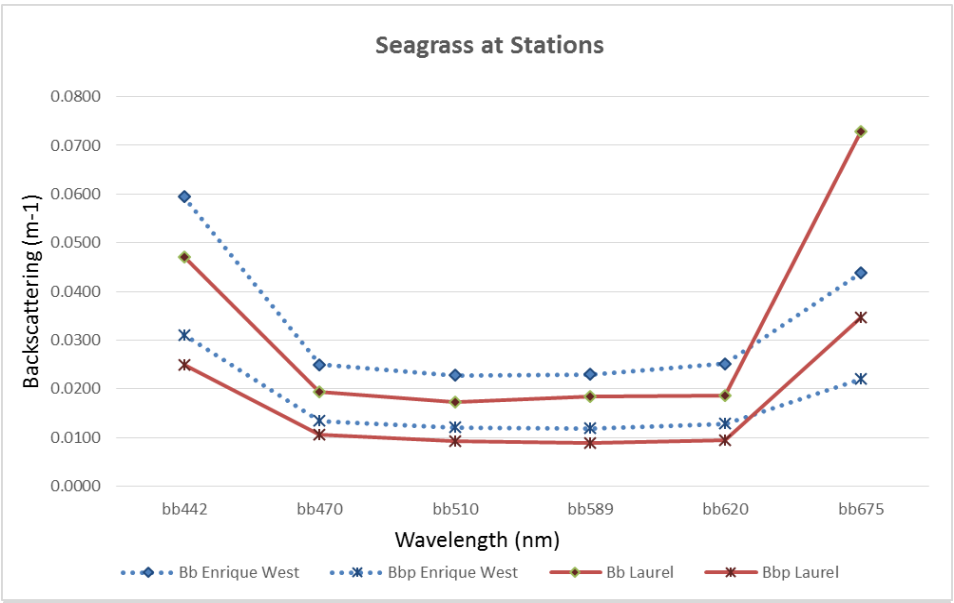

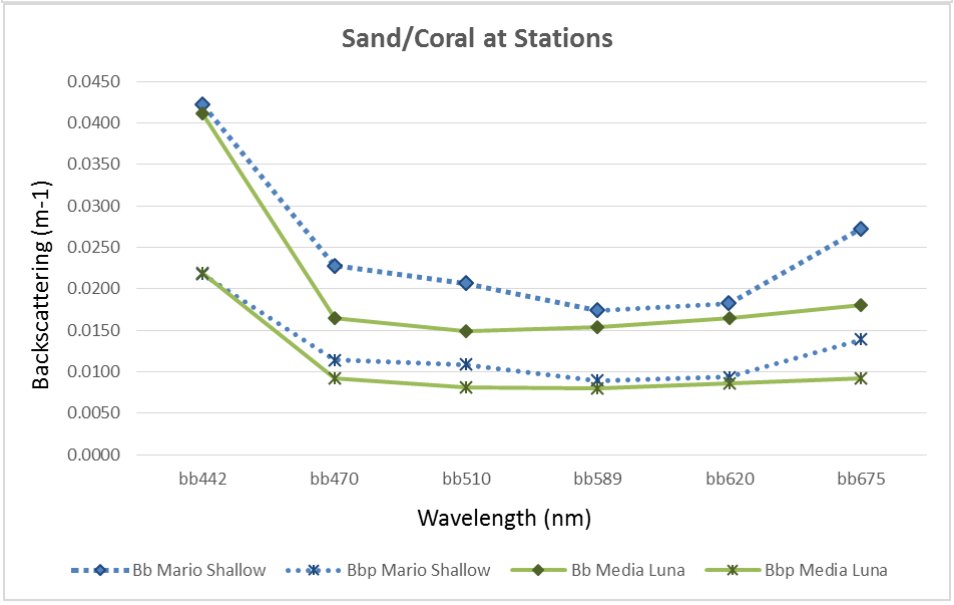

Figure 5: Evaluation of total backscattering (b_b) and backscattering of particles (b_{bp}) for distance from shore, depth of stations and substrate. For distance from shoreline (a), the farthest (Station 1: Media Luna = 3.9 km) and closest (Station 6: Enrique East = 2.1 km). For the depth of stations (b) the deepest (Station 4: Mario Deep = 18 m) and the shallower (Station 6: Enrique East = 1.5 m). For the stations with the benthic cover of seagrass (c), Station 2: Laurel and Station 5: Enrique West. For the stations with the benthic cover of sand/coral (d), Station 1: Media Luna and Station 3: Mario Shallow.

3.2.2 Precipitation Data

The precipitation data were collected from the Integrated Coral Observing Network /Coral Reef Early Warning System (ICON/CREWS) located in the Media Luna cay in La Parguera Reserve. The data includes the monthly summaries of precipitation during the field campaigns (Table 2).

Precipitation Data ICON CREWS			
Month	**Precipitation (mm)**	**Month**	**Precipitation (mm)**
May-07	77.31	Aug-08	220.31
Jun-07	63.91	Sep-08	529.16
Jul-07	47.2	Oct-08	128.55
Aug-07	161.59	Nov-08	149.24
Sep-07	42.63	Dec-08	62.50
Oct-07	128.55	Jan-09	94.87
Nov-07	**0.99**	Feb-09	64.65
Dec-07	**0.95**	Mar-09	58.29
Jan-08	**N/A**	Apr-09	96.42
Feb-08	**N/A**	May-09	152.88
Mar-08	**N/A**	Jun-09	86.94
Apr-08	**0.23**	Jul-09	250.92
May-08	**0.41**	Aug-09	90.06
Jun-08	**0.93**	Sep-09	134.93
Jul-08	**0.26**		

*Table 2: Monthly summary of precipitation from the ICON/CREWS Station located at Media Luna cay in La Parguera Reserve. Note that values in **bold** are not reliable due to missing values, malfunctions or data not available.*

3.2.3 Attenuation Coefficients *(K_d)*

The values of K_d were derived from the AVIRIS image using the methods described by Lee et al. (2007) (Section *2.4.3.3 Image derived K_d)* and compared with the *in situ* values (Figure 6). The absorption and backscattering values were obtained from Table 1 and derived from the AVIRIS image, while the coefficients in the model were derived from Hydrolight simulations (Lee et al. 2007). The image-derived Kd was also evaluated with the deepest station sampled (Figure 7).

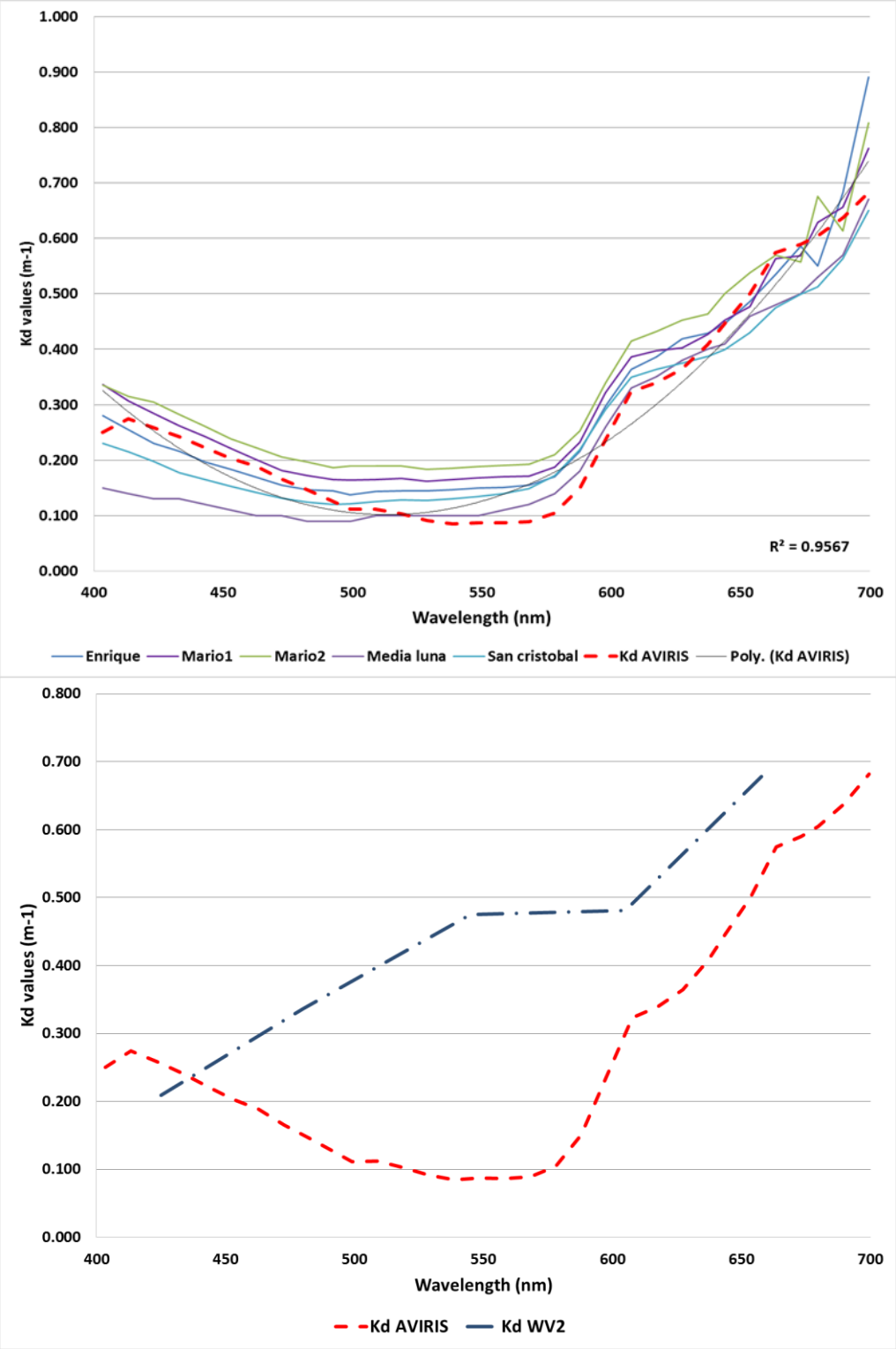

Figure 6: (Top) Comparison of $K_d(\lambda)$ values derived from AVIRIS image (red-dash line) with in situ values for selected sites in La Parguera Reserve. The r^2 is only for AVIRIS image derived Kd. (Bottom) Comparison of $K_d(\lambda)$ values derived from AVIRIS image (red-dash line) and WV2 image (blue- dash-point line).

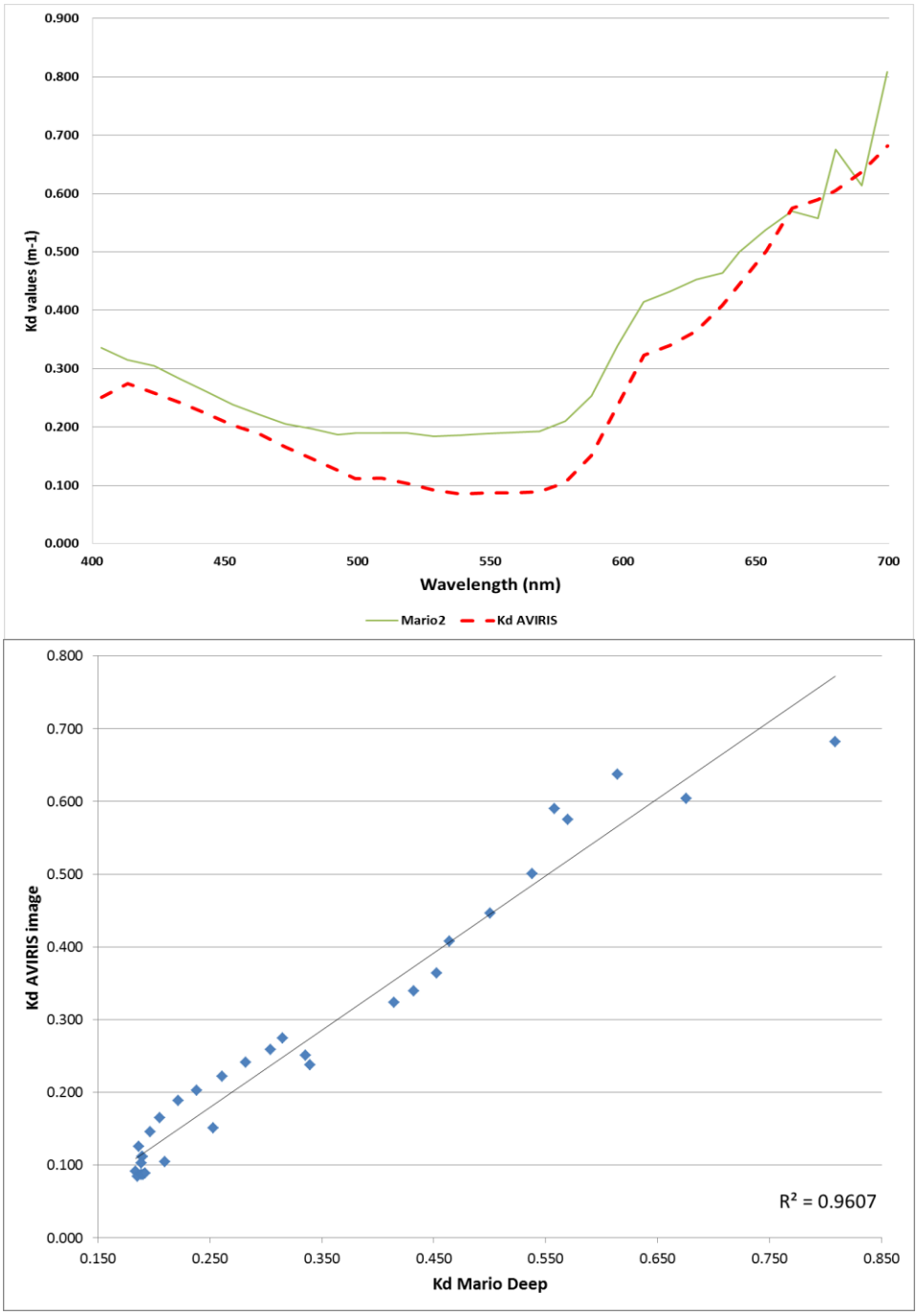

Figure 7: (Top) Comparison of $K_d(\lambda)$ values derived from AVIRIS image (red-dash line) with Mario 2 (18m deepest station) in La Parguera Reserve. (Bottom) Correlation between $K_d(\lambda)$ values derived from AVIRIS image and $K_d(\lambda)$ in situ values from Mario Deep Station (18 meters depth) that coincided with the sensor image collection.

A maximum depth exists for which a submerged bottom can be detected by optical remote sensing, which according to Gordon and McCluney (1975), in optically deep waters is called Z90. This Z90 (first optical depth) is the effective penetration depth of imagery which 90% of the total radiance originates, or depth is approximately: Z90=~ 2.3/Kd (Kirk 2011).

The Kd values were derived from the imagery, so Z90 provided the effective penetration depth of the signal spectrally for each band in the AVIRIS image. This also provided the limits of the water column corrections depending on the depth of the substrate. The first optical depth was calculated for the AVIRIS image and the WV2 image (Figure 8).

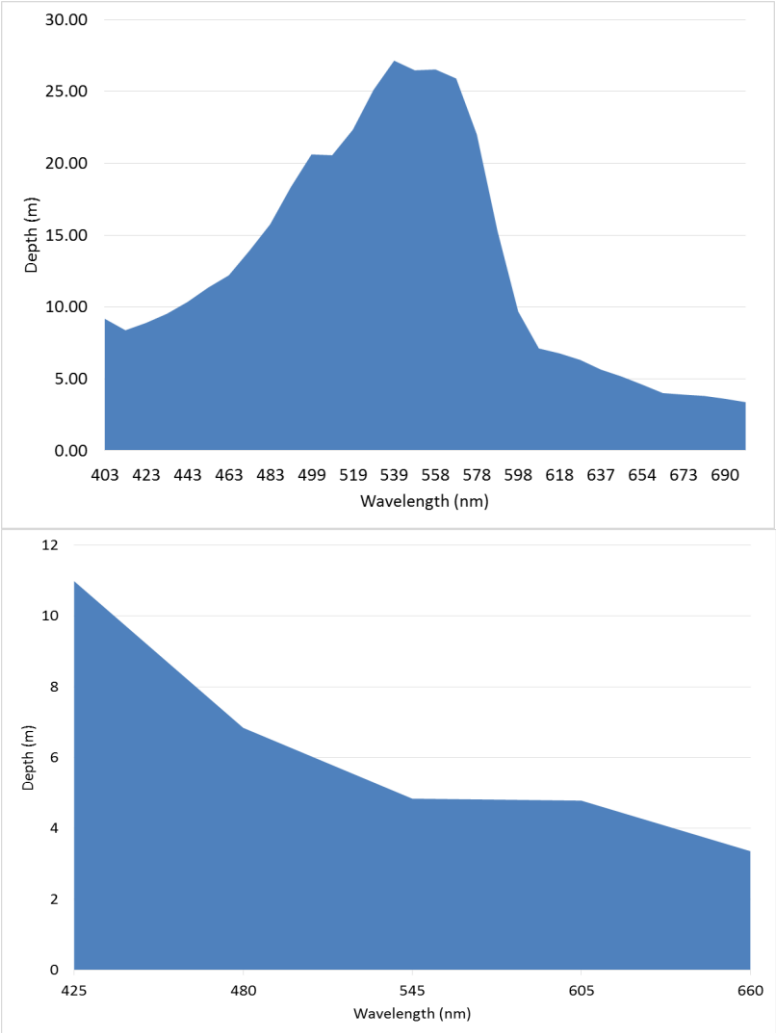

Figure 8: Spectral first optical depth (Z90=2.3/Kd) as calculated by Kirk (1994), for the AVIRIS image (top) and the WV2 images (bottom).

3.2.4 Bottom reflectance (albedo)

The values of bottom reflectance were estimated based on the methods described by Purkis (2005). The values for the reflectance for optically deep water (R_w) were estimated from the AVIRIS and WV2 images using the 100 x 100 pixel window that represented deep water pixels (Figure 9); the values for absorption *(λ)* and backscattering *(λ)* were obtained from Table 1, and the values for K_d *(λ)* were modeled from the AVIRIS image for the scene (*3.2.2 K_d)*. The results of the water column correction was evaluated for different bottom substrates (i.e. sand, seagrass, coral) and compared with above water Rrs before the correction of the water column for the AVIRIS image (Figure 9) and WV2 image (Figure 10).

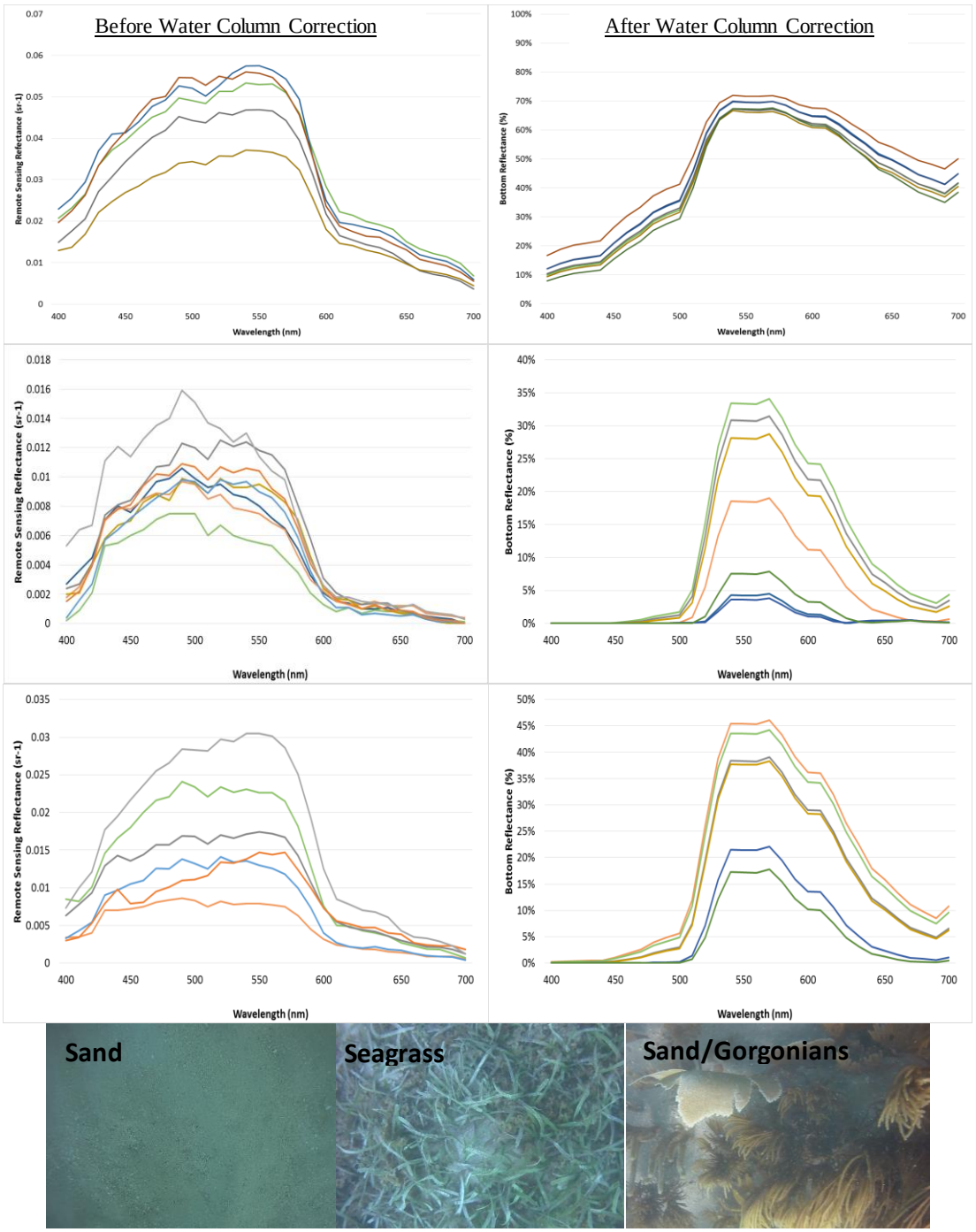

Figure 9: Water column correction of AVIRIS for sand (top), seagrass (middle), and coral/gorgonians (bottom). The spectral curve for each site was evaluated for above water remote sensing reflectance (Rrs) (before water column correction) and bottom reflectance (albedo) (after the water column correction). Colored lines represent different sites. Depth ranges for Sand (1.8-2.2 meters), Seagrass (5.6-14.3 meters), and Coral-Gorgonians (2.5-4.7 meters).

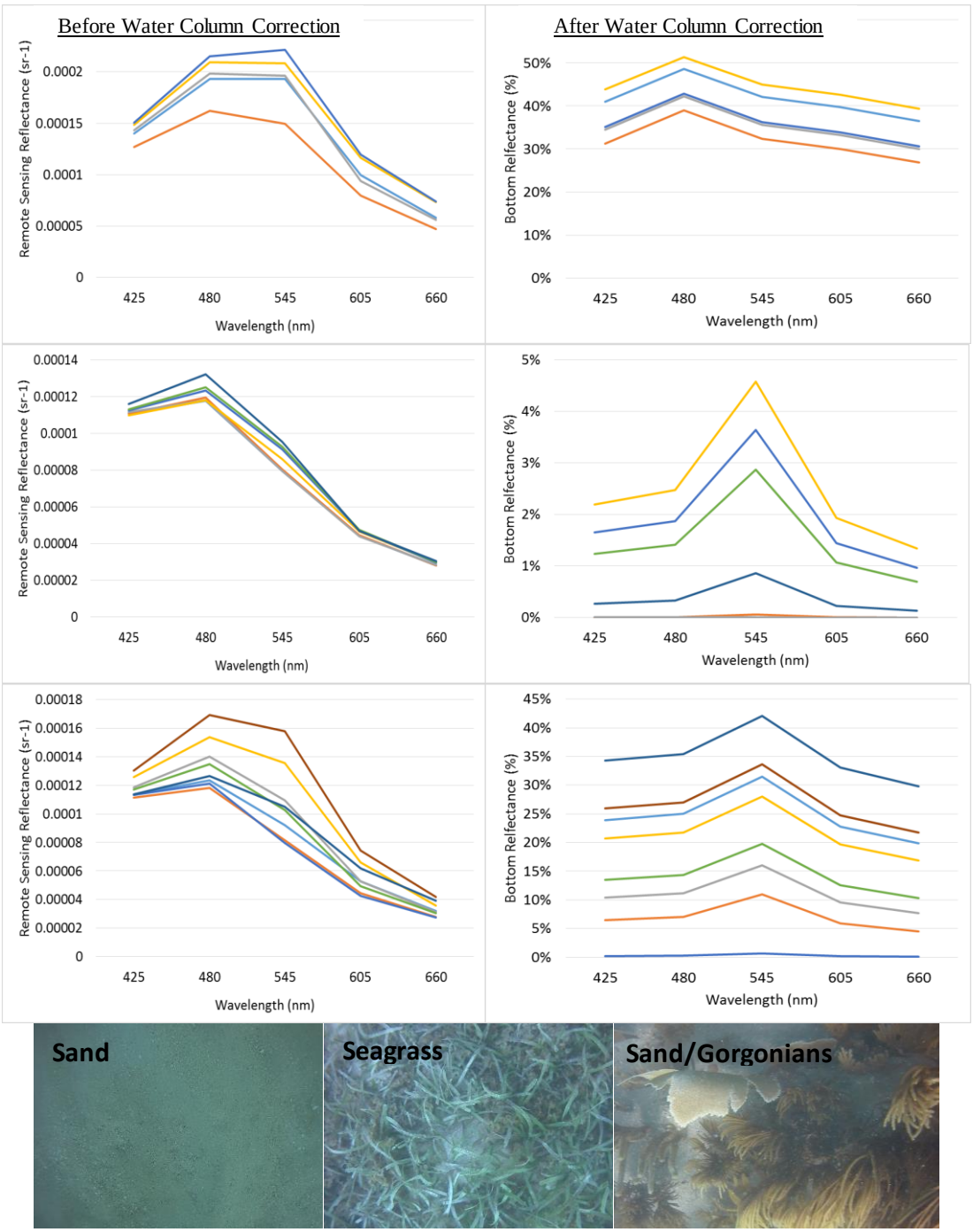

Figure 10: Water column correction of WV2 for sand (top), seagrass (middle), and coral/gorgonians (bottom). The spectral curve for each site was evaluated for above water remote sensing reflectance (Rrs) (before water column correction)and bottom reflectance (albedo) (after the water column correction). Colored lines represent different sites. Images of sites representative of each bottom type (sand, seagrass, sand/gorgonians). Depth ranges for Sand (1.8-2.2 meters), Seagrass (5.6-14.3 meters), and Coral-Gorgonians (2.5-4.7 meters).

The bottom albedo images were obtained from both the AVIRIS and WV2 sensors after the water column correction (Figure 11).

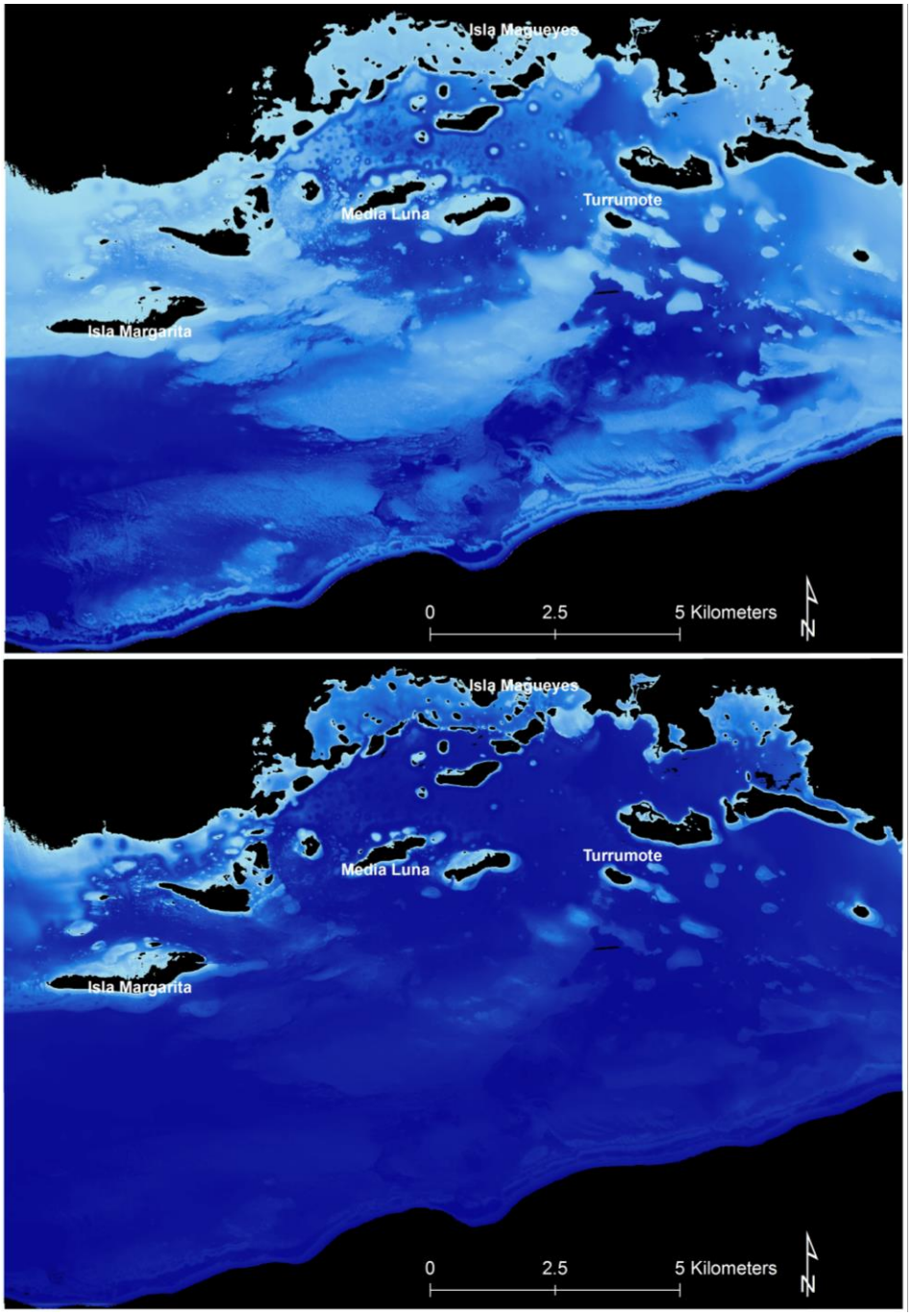

Figure 11: Bottom albedo images for AVIRIS Band 17 (559nm) (top) and WV2 Band 3 (bottom). Lighter blue areas depicts areas of high albedo and dark blue areas depicts areas of lower albedo. Land area have been masked (white).

The LiDAR reflectivity was analyzed with AVIRIS and WV2 bottom albedo images to determine the bands that better correlated after a water column correction (Figure 12).

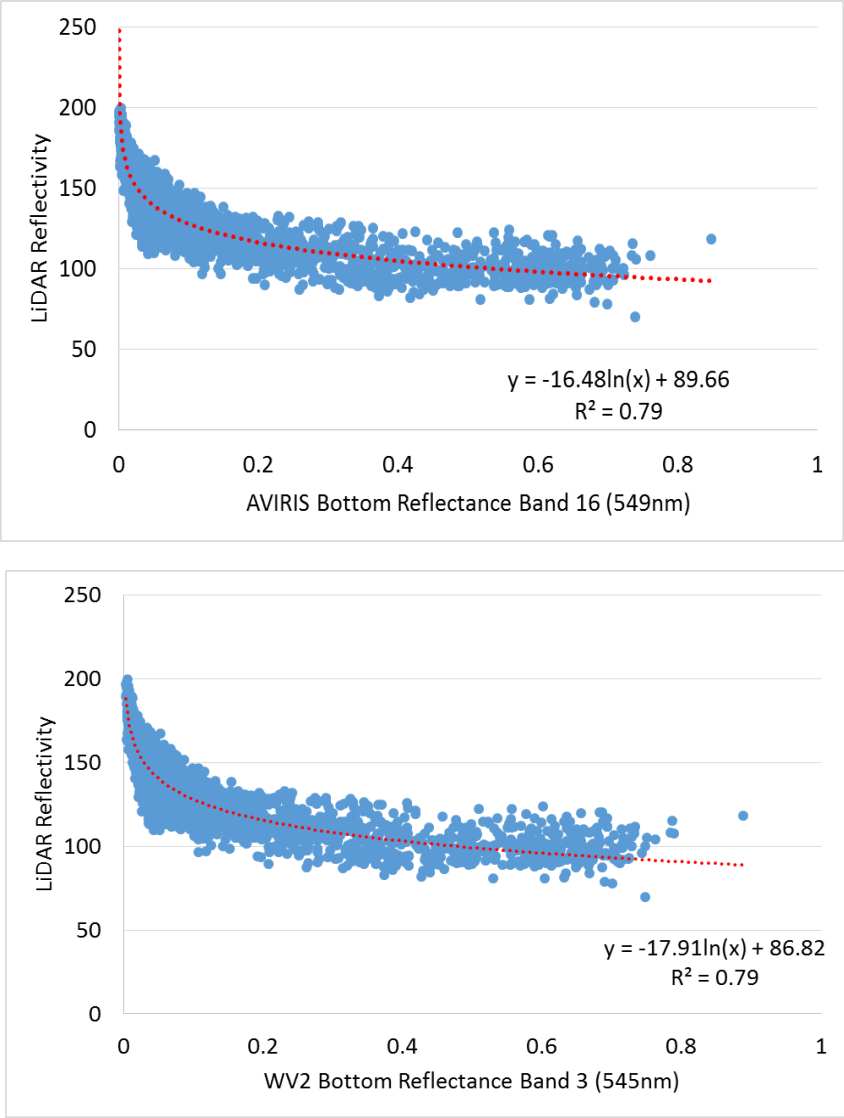

Figure 12: Correlation between bottom albedo bands from AVIRIS (band 16, 549nm) and WV2 (band 3, 545nm) (top). These bottom albedo bands from AVIRIS (middle) and WV2 (bottom) were highly correlated to the LiDAR reflectivity band. This correlation was based on random points (n=4694) selected for La Parguera Reserve.

Since the values of LiDAR reflectivity can be influenced by depth, it was normalized by depth and compared again with the bottom albedo values from AVIRIS and WV2 (Figure 13).

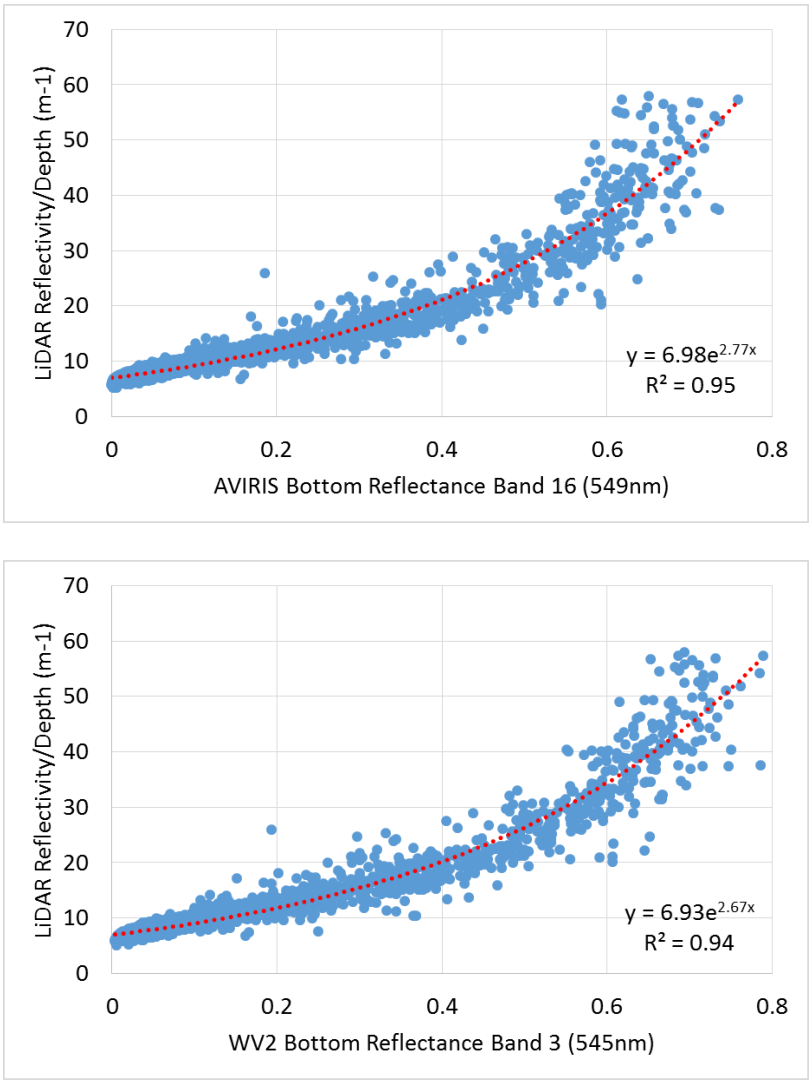

Figure 13: Correlation of bottom albedo bands from AVIRIS (top) and WV2 (bottom) with the LiDAR reflectivity band after the removal of the influence of depth. This correlation was based on random points (n=4694) selected for La Parguera Reserve.

4. Discussion

The images were evaluated after an atmospheric correction to extract values of IOP and AOP using different models. Values of absorption, scattering, backscattering and attenuation were measured, correlated with image derived values and used in the water column corrections.

4.1 Image derived AOP/IOP

4.1.1 Absorption (a)

The absorption and backscattering parameters were derived from both the WV2 image and the AVIRIS image (Table 1). The values of absorption present a significant increase when compared with values of absorption of pure water (Pope and Fry 1997) indicating that the waters of La Parguera are dominated by absorption. This absorption is related to the presence of chlorophyll present in the phytoplankton cells, which absorbs in the blue and red region, with very little absorption in the green, characteristic of Case 1 waters (Mishra, et al. 2007 and 2005; Kirk 2011). The waters around La Parguera Reserve show a concentration of chlorophyll-a that can range from 0.171 to 1.122 µg/L (Otero and Carbery 2005). Also, as noted by Armstrong et al. (2012) these median absorption values increase as distance from shore decreases, and the total absorption (a) at 443 nm ranged from 0.26 to 0.32 m^{-1} (Figure 3 and Figure 4). This gradient can also be related to the presence of phytoplankton in La Parguera Reserve, where Otero and Carbery (2005) found that a general land-ocean gradient of chlorophyll-a concentration exists due to the closer coupling of terrestrial, coastal, and bottom-derived materials in the water column in shallower regions, and the presence of anthropogenic input sources very near the coast.

These image-derived values were also within the range of the *in situ* values of absorption measured from the field campaign using the ac-9 instrument (Figure 4). These values of absorption measured *in situ* were compared with absorption values derived from the AVIRIS and WV2 images and a good correlation was found between the values (r^2=0.90). The values of absorption were selected from the nearest spectral channel of AVIRIS and WV2 to match the ac-9 instrument. This supports the efficiency of the models by Lee et al. (1999) to obtain total absorption values from imagery, even when *in situ* values and imagery were not collected simultaneously. The values of total absorption at 443 nm for AVIRIS and WV2 were 0.3107 m^{-1} and 0.3011 m^{-1} respectively, and these values are within the range of 0.2251 m^{-1} to 0.3475 m^{-1} for all stations and dates sampled. Cardona-Maldonado (2008) found that the average absorption at 443 nm for various sites in La Parguera Reserve ranged from 0.04 to 0.10 m^{-1} which are relatively low when compared with our sites. These low values can be related to the majority of the stations being farther away from the coastline than our stations. CARICOOS (pers.comm.) sampled absorption using an ac-9 instrument in La Parguera Reserve for various dates in 2011 and the median values at 443 nm were 0.2380 m^{-1} for Station 6, an intermediate station from our stations and Cardona-Maldonado (2008) stations.

4.1.2 Backscattering (b_b)

The backscattering values also present a significant increase when compared with values of backscattering of pure water (Morel 1974; Buiteveld et al. 1994; Twardowski et al. 2007) (Table 1). However, the image-derived values were lower when compared with *in situ* values of backscattering measured from the field campaign using the HydroScat-6 instrument. The backscattering at 442 nm for all stations ranged from 0.041 m^{-1} at Station 1 (Media Luna) to 0.064 m^{-1} at Station 6 (Enrique East) (Figures 3 and 4). Rodriguez-Guzman (2009) reported

similar total backscattering values from approximately 0.007 to 0.060 m^{-1} for the Mayaguez Bay from offshore waters to inshore waters, respectively. The backscattering values evaluated by Kutser et al. (2003, 2009) from the Great Barrier Reef (0.01 to 0.18 m^{-1}) in Australia and from the Baltic Sea (0.005 to 0.2 m^{-1}) are within the range of the *in situ* values collected for La Parguera.

The backscattering coefficient is generally inversely proportional to wavelength (Mishra et al. 2007), were higher values are observed in the blue region continuously decreasing with longer wavelengths (Morel et al. 2007) In all the stations evaluated, higher values were observed in the blue region (425 nm), and remained in a narrow range of values though the 470, 510 589 and 620 spectral channels, and were higher again in red region (675nm) (Figure 4). Assuming the instrument was performing correctly, the higher values can be likely attributed to chlorophyll-*a* fluorescence excited at 676 nm and emitted at 681-nm from the Hydroscat-6 spectral channel (Boss et al. 2003).

The difference in the backscattering values between the stations sampled can be attributed mainly to the distance from shoreline and bottom substrate. The lower values of backscattering were present in Station 1 (Media Luna) at 3.9 kilometers from the shore, while the higher values of backscattering were present at Station 6 (Enrique East) at 2.1 kilometers. This offshore/inshore variation in the values of total backscattering has been reported by Rodriguez-Guzman (2008) in Mayaguez Bay, Puerto Rico and by D'Sa and Miller (2003) in the Mississippi River.

Another factor that influences the backscattering value is the presence of inorganic particles and CDOM from re-suspension of bottom sediments, nutrient input and wave action (Morel 1974;

Boss et al. 2003; Twardowski et. al. 2007). The total backscattering is a summary of the backscattering by particles (b_{bp}) and pure water (b_{bw}) (Equation 2-4) (Morel, 1974). The Hydroscat-6 provided both (b_{bp}) and (b_{bw}) so each component was evaluated individually to quantify the contribution of particles for each station based on distance from shore, depth and bottom type (Figure 5). Conversely to what can be found in turbid waters, where high values b_{bp} values can be found in inshore waters (Rodríguez-Guzman 2008), the contribution of the backscattering particles for our stations was always within a range of 50% ±5% of the total backscattering for the distance from shoreline, depth of stations, and similar benthic cover. Also, the relative constant contribution of particles to the backscattered signal indicated that the molecular contribution (backscattering of seawater) is the dominant term in the total backscattering signal, especially at low chlorophyll concentrations (Twardowski et al. 2007)

For the stations analysis in distance from shoreline, for the farthest station (Station 1: Media Luna = 3.9 km) and the closest station (Station 6: Enrique East = 2.1 km), the median difference was 60% in the total backscattering. This indicates the importance of the distance from shoreline to the total backscattering signal, considering that the depth range for these stations was very close (1 meter) and the substrate for both stations was mainly sand. For the analysis of depth of stations, the median difference was 49% from the deepest station (Station 4: Mario Deep = 18 m), and the shallower station (Station 6: Enrique East = 1.5 m). For the stations with the benthic cover of seagrass (Station 2: Laurel and Station 5: Enrique West), the median difference was 26%, which indicated that even with the same bottom type, differences in the backscattering values were present. An important factor was that the depths for these stations was very similar (2.0 meters), but the distance from shoreline was 1 kilometer between stations, indicating that

this later factor can contribute to the median difference value. Also, the presence of sand in the seagrass habitat could be re-suspended affecting the backscattering signal. The lowest median difference values were found for the stations with the benthic cover of sand/coral (Station 1: Media Luna and Station 3: Mario Shallow), with 22%. The difference in depths for these stations was 1.5 meters, while the difference in distance from shoreline was 1.6 kilometers; again, the later can contribute to median difference value.

Some additional factors can also influence the difference of the image and *in situ* backscattering values: no IOP's were collected at the time of the imagery collection so water column conditions can be only inferred from the *in situ* values collected from the field campaign from other dates, the waters of La Parguera can be considered Case-1 waters, dominated by absorption of phytoplankton, so most of the photons are absorbed and there is less backscatter signal (Kirk, 2011), and the modeled backscattering values from WV2 and AVIRIS were derived from deep water pixels where no influence from the bottom is present in the backscattered signal while the *in situ* values were influenced by the bottom type via re-suspension since values were obtained close to the bottom (Armstrong et al. 2012).

4.1.3 Attenuation (c)

The values of beam attenuation coefficient were measured *in situ* using the ac-9 instrument and ranged at 443 nm from 0.56 to 0.35 m^{-1} (Figure 3). These values presented a more defined trend of increasing values as distance from shore decreases (Armstrong et al. 2012). Cardona-Maldonado (2008) reported the highest average attenuation values of ~0.60 m^{-1} at Enrique Reef, and the lowest value of ~0.25 m^{-1} at El Palo for sites in La Parguera Reserve. Also values of

beam attenuation include the contribution of the absorption and backscattering (a + b = c), so it can related to the attenuation coefficient at a discrete wavelengths (Kirk 2011).

4.1.4 Scattering (b)

Scattering is caused in natural waters by molecular scattering of water itself (inversely with the fourth power of wavelength) and particles, including phytoplankton and suspended sediments (Kirk 2011). Phytoplankton can also make a significant contribution to the scattering of light but due to their low refractive index relative to water, phytoplankton cells are weak backward scatters compared to inorganic particles (Kirk 2011). The values of scattering were not measured directly but were derived using the established relationship b = c-a, where b is the scattering coefficient, c is the beam attenuation coefficient, and a is the attenuation coefficient (Kirk 2011) (Figure 3). These scattering values followed the same trend as the absorption values where they increased as distance from shore decreased.

4.1.5 Statistical significance

Several statistical tests were conducted to evaluate the variation of IOP's in La Parguera and their environmental drivers. An ordination analysis, such as non-metric multidimensional scaling (nMDS) procedure was run to examine the difference and similarities in the optical properties (absorption, attenuation, backscattering) between the sites (Figure 14). The farther away the points were, the more different they are, where in this case all sites were the same from each other except Station 5 (Enrique East) and Station 6 (Enrique West). These two sites were very similar to each other and very different from the other sites.

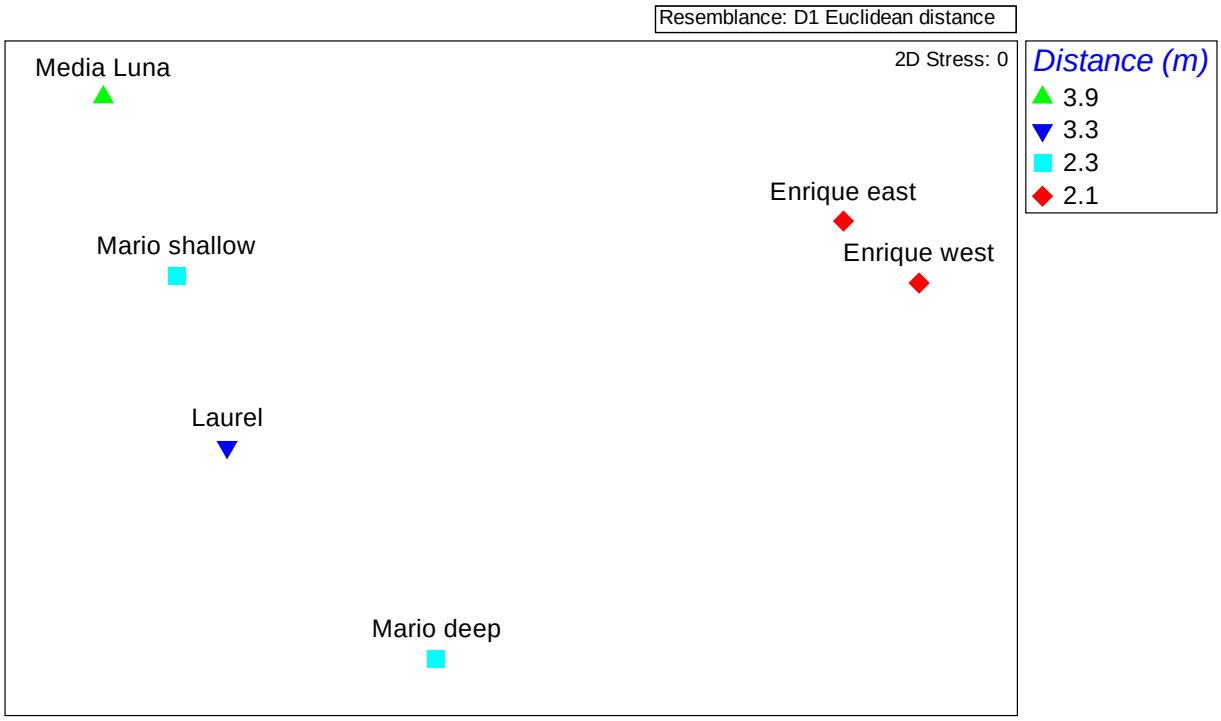

Figure 14: An Ordination analysis-non metric multidimensional scaling (nMDS) for the sites of the bio-optical field campaign to evaluate the difference and similarities in the optical properties.

To test these differences between sites we ran a one-way repeated measure ANOVAs. All values for absorption, attenuation and backscattering were log-transformed (log based 10) to agree with the assumptions of normality. The fixed variable for these analyses was site and the repeated random variables were years and months.

Absorption varied significantly between sites in La Parguera Reserve (Table 3). A post hoc test was done to establish the significant variability between sites (Appendix A). As confirmed with nMDS test, the sites significantly differed from each other in absorption values. The sites Enrique West and Enrique East were very different from the other sites (Appendix A). This difference could be attributed to factors like distance from shoreline, depth of stations or precipitation.

Factor	numDF	denDF	F-value	p-value
Intercept	1	105	567.69	<0.0001
Site	5	105	20.62	<0.0001

Table 3: One way ANOVA for absorption for sites in La Parguera Reserve.

The attenuation significantly varied between sites (Table 4). The post-hoc test confirmed that attenuation at Enrique East and Enrique West was unique and varied from the other the sites. Also, attenuation at Media Luna was different from Laurel and Mario deep (Appendix A).

Factor	numDF	denDF	F-value	p-value
(Intercept)	1	101	406.0301	<.0001
Site	5	101	18.5579	<.0001

Table 4: One way ANOVA for attenuation for sites in La Parguera Reserve.

The backscattering variations were significantly between sites (Table 5). As confirmed with the post-hoc test, the backscattering at Enrique East and Enrique West sites were unique and varied significantly from the other the sites (Appendix A). All the other sites had similar backscattering.

Factor	numDF	denDF	F-value	p-value
(Intercept)	1	98	39.31877	<.0001
Site	5	98	13.61564	<.0001

Table 5: One way ANOVA for attenuation for sites in La Parguera Reserve.

A multiple regression test analysis was completed to evaluate the relationships between depth/distance of sites and the optical properties. The values of absorption were positively associated with distance to shoreline ($p=0.07$, $r^2=0.7148$) and this factor explained close to 72% of the variation in absorption values sampled in La Parguera Reserve (Table 6). There was no association found between absorption and depth of the sites.

For the values of attenuation a positively weak relationship was found between attenuation values and distance from shoreline ($p=0.16$, $r^2=0.51$). There was no association found between attenuation and depth of the sites (Table 6).

For the values of backscattering a positively weak relationship was found between backscattering values and distance from shoreline ($p=0.19$, $r^2=0.45$). There was no association found between backscattering and depth of the sites (Table 6).

		Estimate	**Std. Error**	**t-value**	**p-value**	
Absorption	(Intercept)	-0.39368	0.039819	-9.887	0.0022	*
	Depth	-0.00309	0.001599	-1.933	0.1487	
	Distance	-0.04915	0.013542	-3.63	0.036	*
Attenuation		**Estimate**	**Std. Error**	**t-value**	**p-value**	
	(Intercept)	-0.16202	0.094279	-1.718	0.1842	
	Depth	-0.00193	0.003785	-0.51	0.6453	
	Distance	-0.08621	0.032063	-2.689	0.0745	
Backscattering		**Estimate**	**Std. Error**	**t-value**	**p-value**	
	(Intercept)	-1.07002	0.112183	-9.538	0.00244	*
	Depth	-0.00842	0.004504	-1.869	0.15844	
	Distance	-0.0753	0.038151	-1.974	0.14293	

Table 6: Multiple regressions for absorption, attenuation and backscattering for sites in La Parguera Reserve to evaluate the relationships between depth/distance of sites and the optical properties. Asterisks show significance of relationship.

A multiple regression tests analysis was completed to evaluate the relationships between rainfall amounts and the optical properties (Appendix B). Since the sites were different, they were grouped into Laurel, Mario Shallow, Mario Deep and Media Luna (Group 1), and another group with Enrique West and Enrique East sites (Group 2). For the Group 1, absorption was positively influence by rainfall but this only explained close to 20% variability ($r^2=0.20$). For the Group 2, absorption was also positively influenced by rainfall, but only explained 41% of the variability ($r^2=0.41$). For both Group1 and Group 2, the rainfall did not influence the attenuation of the sites

during the study. For Group 1, backscattering was positively influence by rainfall but only explained the 26% of the variance at these sites (r^2=0.26). For the Group 2, backscattering was also positively influenced by rainfall, but only explained 31% of the variability (r^2=0.31). The rainfall better explained the variance in backscattering and absorption, mainly at the closest site from shore at Enrique West and Enrique East (Group 2).

Overall, the absorption was positively associated with distance to shoreline (p=0.07, r^2=0.71) and rainfall also explained the variation in absorption values sampled in La Parguera Reserve, especially in stations closest to shore. This relationships could be associated to the runoff and input of terrestrial, coastal, and bottom-derived materials enhancing phytoplankton biomass production (Otero and Carbery 2005).

4.2 Attenuation coefficient of downwelling irradiance (Kd)

The values for the attenuation coefficient were compared between modeled Kd (Lee et al. 2005) from the AVIRIS image and the *in situ* values of Kd measured at the time of the image collection from various sites in La Parguera Reserve. The correlation between these values was explained by a second order polynomial (r^2= 0.96) and provides further validation that Kd values can be derived efficiently from imagery. Additional values of K_d were derived from the WV2 image and these presented higher values when compared with the *in situ* values and AVIRIS (Figure 6). The disagreement of WV2 Kd values was expected, because Kd, being an apparent optical property (AOP) (Kirk 2011), can be affected by changes in the light field. Also, no *in situ* Kd values were collected during the WV2 image collection for comparison. Additionally, the derivation of Kd using Lee's Model requires the values of absorption and backscattering. These values were derived using Lee's semi-analytical model (Equation 3-3 and 3-6) and required specific spectral

channels that were not available for WV2 multispectral sensor, they were matched to the nearest spectral channel.

A strong relationship (r^2= 0.96) was found between the AVIRIS-derived Kd and the deepest station (Mario 2, 18m deepest station). These results were important, since the absorption and backscattering required for the image-derived Kd was based on deep pixels (Figure 7).

Cardona-Maldonado (2008) calculated Kd values for various sites in the south-southwest Puerto Rico including La Parguera Reserve. The averaged Kd values for the study sites after averaging all the visits between December 2000 and February 2006 ranged from an average maximum of 0.319 m^{-1} for Boya Verde at Guayanilla to an average minimum of 0.142 m^{-1} for Turrumote III. The maximum Kd value for La Parguera was El Corral station with 0.22 m^{-1} and the minimum Kd value was Turrumote III with 0.142 m^{-1}. Additional experiments were conducted in La Parguera but only evaluated Kd (PAR) (Bejarano Rodríguez 2006; Torres et al. 2007) or measured turbidity (Otero and Carbery 2005) on various sites. The values from Kd derived from imagery and collected *in situ* were within the range of expected values without extreme weather events.

The Z90 factor was analyzed to establish the limits of detection for the imagery. The Kd values were derived from the imagery, so Z90 provided the effective penetration depth of the signal spectrally for each band in the AVIRIS image (Figure 8). This also provided the limits of the water column corrections depending on the depth of the substrate. The maximum depth at which a substrate can be detected increases as Kd decreases (Kirk 2011). Only in the narrow spectral

range of 500 nm to 578 nm does the maximum depth exceed 20 meters. This limitation is relevant in the identification of substrates considering that 38% of the benthic habitats of La Parguera Reserve are deeper than 20 meters depth. In the blue bands the depth limit ranges from 8-15 meters, while the red band depth limits ranges from 4-8 meters. For the WV2 the maximum depth decreased from 11.98 meters in the blue region, to 3.35 meters in the red region. According to Gordon and McClunney (1975), these limitations in the optical depth impose limits in the detection of a target that is below the Z90 limit, thus impairing the efficiency of the water column corrections.

4.3 Water Column Correction

The above water Rrs spectra in shallow waters contains information of the interactions of photons with the water column constituents and the bottom (Maritorena 1994; Mishra et al. 2007). The imagery products were evaluated to obtain images that contain only information from the bottom substrate, after a water column correction for both AVIRIS and WV2.

4.3.1 AVIRIS

The above water Rrs spectral signal for submerged sand had the maximum Rrs values, while the coral-gorgonians substrate had lower Rrs values, and seagrass had the lowest Rrs values (Figure 11). However, the spectral shape of above water Rrs was very similar for all evaluated substrates with no specific absorption features of different benthic bottom types identified because of the water column attenuation on the bottom reflectance spectra.

The bottom reflectance was also evaluated for different bottom substrates (Figure 9). For submerged sand the spectra presented a narrow range of values with a gradual increase in reflectance with increasing wavelength, which is a typical sand reflectance characteristic. The

reflectance values for sand were also the highest observed and when compared with similar sand spectra measured *in situ* by other researchers, it is within the range of magnitude and spectral shape (Hochberg et al. 2003). The seagrass spectra exhibited a very low reflectance values at blue region characteristics of both chlorophyll and carotenoid absorption in blue band, a reflectance peak at around 550 nm, and chlorophyll absorption features at 675 nm (Kirk 2011). Also the maximum reflectance peak was at approximately 32% (550 nm) and again this corresponded with similar spectra presented by Hochberg et al. (2003) in both shape and magnitude of seagrass spectra. The broad range of bottom reflectance at the reflectance peak (5-35%) could be related to different percent of coverage and composition of seagrass habitats and was not evaluated in this study. Also, seagrass appear as dark features with low reflectance values, which can affect the retrieve signal due to low signal/noise ratio after an atmospheric and water column correction (Mishra et al. 2005 and 2007). For the coral/gorgonian substrate, the bottom albedos ranged from 18% to 45% with very low reflectance between 400 to 500 nm, a peak of reflectance around 550 nm, and a narrow chlorophyll absorption feature at 675 nm. This presented a higher range of reflectance values when compared with values for soft corals/gorgonians presented by Hochberg et al. (2003) (approximately 5% to 28% at 550 nm) that can be attributed to the presence of sand and other high reflectance substrates present in the bottom signal from the image-derived albedo (Lee et al. 2001; Purkis 2005; Mishra et al. 2007). The similarity of the spectral shape of albedo for corals/gorgonians with seagrass, indicated the presence of pigments determined by spectral absorption properties of each substrate. Additional similarities in the spectral shape can be attributed to the limitations of the water column correction to differentiate between dark objects with low albedo due to low signal/noise ratio.

However, these bottom albedos are important in developing a benthic habitat map without the influence of the water column in the spectral signal.

4.3.2 WV2

Bottom albedo images were also generated from the WV2 image (Figure 10). The limitations of WV2 being a multispectral sensor did not provided the required spectral resolution to compare with benthic spectra based from field measurements (i.e. Ocean Optics S2000 portable spectrometer, Hochberg et al. 2003). However, bottom albedo values were used to compare if the reflectance were within the range of values for that substrate and some general reflectance features could be evaluated. The evaluated sites were the same ones used in the AVIRIS reflectance image.

The above water Rrs spectral signal for submerged sand had the maximum Rrs values, while the coral-gorgonians substrate had lower Rrs values, and seagrass had the lowest Rrs values. The spectral shape of above water Rrs was very similar for the sand and the coral-gorgonian substrates, while the seagrass sites presented a close spectral range. However, no specific absorption features of different benthic bottom types identified because of the water column attenuation on the bottom reflectance spectra.

The bottom reflectance was also evaluated for different bottom substrates. For submerged sand, the spectra presented a higher range of values with a gradual increase in reflectance with a gradual decrease with increasing wavelength, which is not representative of sand reflectance. The spectral shapes were very different when compared with AVIRIS bottom albedo. The seagrass spectra exhibited low reflectance values at blue region characteristics of both

chlorophyll and carotenoid absorption in blue band, a reflectance peak at around 545 nm, but chlorophyll absorption features at 675 nm was not identified because the WV2 red band is centered at 660 nm (Kirk 2011). The maximum reflectance peak was at approximately 4.5% (550 nm), which was very low when compared with AVIRIS image bottom albedo. All the seagrass bottom albedo was very low (<4.5%) which were related to the model limitation application in WV2 in extracting values from dark objects. Also, seagrass appear as dark features with low reflectance values, which can affect the retrieve signal due to low signal/noise ratio after an atmospheric and water column correction (Mishra et al. 2005 and 2007).

For the coral/gorgonian substrate, the bottom albedos ranged from 1% to 43% with low reflectance between 400 to 500 nm, and a peak of reflectance around 550 nm. This presented a similar range of reflectance values when compared with AVIRIS reflectance values for soft corals/gorgonians, which again, can be attributed to the presence of sand and other high reflectance substrates present in the bottom signal from the image-derived albedo (Lee et al. 2001; Purkis 2005; Mishra et al. 2007). The similarity of the spectral shape of albedo for corals/gorgonians with seagrass, indicated by the presence of a reflectance peak at approximately 550 nm, which is dominated by the presence of pigments determined by spectral absorption properties of each substrate. Additional similarities in the spectral shape can be attributed to the limitations of the water column correction to differentiate among dark objects with low albedo due to low signal/noise ratio.

Additional limitations of the water column correction can be attributed to the first optical depth (Z90) imposed by the attenuation coefficient. The limitations of the retrieval of bottom albedo

were more apparent in the WV2 image than in the AVIRIS image (Figure 11) since deeper features were still visible in this image after the removal of the water column. All the substrates evaluated were within the maximum extent of the Z90 for the AVIRIS image, so the spectral identification of these substrates were available after the water column correction (Figure 11). For the WV2 image, the Z90 limits were shallower, but all the substrates were within this depth range. However, bright features that were present in the AVIRIS image in deeper areas were not identified in the WV2 image. Even with the limitations presented, a bottom albedo map for La Parguera Reserve was developed after a water column correction that can increase the accuracy of the mapping of benthic habitats.

4.3.3 LiDAR Reflectivity

The LiDAR reflectivity image was analyzed with bottom albedo bands from AVIRIS (32 bands) and WV2 (5 bands). The bands with the highest correlation from AVIRIS was band 16 at 549 nm (r^2 =0.79), and for the WV2 band 3 at 545 nm (r^2 =0.79) (Figure 12). An inverse relationship was found between the bottom reflectance and the LiDAR reflectivity. These bands also correspond to the highest penetration bands for the Z90 (first optical depth). Although the values between these bands differ, the bands were highly correlated in terms of bottom reflectance for AVIRIS and WV2 (Figure 12).

According to Costa et al. (2009) the LiDAR intensity surface was highly correlated with the LiDAR bathymetric surface at a broad spatial scale ($r=0.84$; $p\leq0.001$) that can be attributed to the fact that the Tenix LADS intensity algorithm has not sufficiently decorrelated the geometric and radiometric influence of LiDAR targets. To further evaluate the correlation between LiDAR

reflectivity and bottom albedo, the influence of depth was removed. The correlation of the LiDAR reflectance with bottom albedo improved significantly for both AVIRIS (r^2 =0.95) and WV2 (r^2 =0.95) after the removal of the depth influence (Figure 13). An exponential positive relationship between LiDAR reflectivity values and bottom reflectance was found between both passive and active reflectivity values.

Other projects have focused on comparing LiDAR reflectivity to other active sensors (i.e. multibeam) but no results were found that correlated LiDAR reflectivity to bottom albedo derived from a passive sensor.

The LiDAR reflectivity is a relative value rather than an absolute value for each point, the entire dataset is scaled to ensure the full dynamic range is used over it (Collins et al. 2007). Treating the values as relative allowed the removal of the depth influence and further correlation with passive bottom albedo, but the values and relationships established are unique for the study area. Nevertheless, this approach provides a multisensor highly correlated reflectivity product that can further enhance a classification of the benthic habitats.

5. Conclusions

The combinations of semi-analytical models and bio-optical data collection provided an effective methodology to analyze the bottom albedo and water optical parameters. These semi-analytical models are based on simple approximations of the remote sensing reflectance, where they use the relationship between the oceanic constituents and the IOP's upon which to base the inversion (Gordon 1989; Morel 1988). This study represented the first integration of these algorithms to high resolution hyperspectral and multispectral imagery, correlated to a comprehensive time series of bio-optical properties for La Parguera Reserve. The values of absorption and backscattering were retrieved successfully using semi analytical models and this information was also used to derive attenuation coefficient of downwelling irradiance. A baseline data for the inherent optical properties was established for La Parguera Reserve and the distance to shore was the most significant variable in the variation of these parameters. A strong inverse relationship was found between distances from shore to increasing values of absorption. The values of absorption were positively associated with distance to shoreline ($p=0.07$, $r^2=0.71$) and this factor explained about 71% of the variation in absorption values sampled in La Parguera Reserve. The values of image-derived absorption exhibited a strong correlation when compared with *in situ* values. The modeled values of Kd were also highly correlated to *in situ* values. These efforts of a time series *in situ* collection of AOP/IOP and validation are align with NASA's Pre-Aerosol, Clouds, and Ecosystem (PACE) satellite mission that were intended to create a high quality, diverse and extensive database of existing multi- and hyperspectral inherent and apparent optical properties (IOP/AOP) for the validation of remote sensing products and the development of algorithms (PACE, http://decadal.gsfc.nasa.gov/PACE.html).

The water column correction techniques were successfully applied to the AVIRIS and WV2 imagery. A baseline image of bottom albedo from passive sensors was developed for La Parguera Reserve. For the AVIRIS image, bottom albedo values for sand, seagrass, and coral-gorgonians were in good agreement with *in situ* values for these substrates in both spectral shape and magnitude. Additionally, spectral absorption and reflectance features were identified, and these features where absent in the above water remote sensing reflectance spectra, and only present after the water column correction. The limitations of the water column correction attributed to the first optical depth (Z90) were more apparent in the WV2 image than in the AVIRIS image, since deeper features were still visible in this image after the removal of the water column. According to Wang et al. (2005) semi-analytical algorithms are based on the assumptions that the absorption and backscattering coefficients with their spectral shapes are known, and the relationship of these factors to the Rrs is known. All of these three assumptions were completed, which allow the applicability of semi-analytical models to regional and local waters.

The LiDAR reflectivity was highly correlated to bottom albedo images from AVIRIS ($r^2 = 0.79$) and WV2 ($r^2 = 0.79$), and this correlation was further improved by removing the depth influence from the LiDAR reflectivity (AVIRIS, $r^2 = 0.95$; WV2, ($r^2 = 0.94$). This relationship between LiDAR reflectivity values and bottom reflectance could be used to enhance the development of benthic habitat maps by coupling the benefits of the active sensor to the passive sensors.

Even when the water column correction was successful in retrieving bottom albedo for selected benthic habitats, some spectral shapes and features were not distinguishable due to the spectral

resolution of AVIRIS (10 nm) when compared with underwater *in situ* measurements using a portable spectrometer (1.3 nm) (Hochberg et al. 2003).

Some limitations were related to the resampling of the images. The image resampling was necessary due to the different spatial resolutions of passive imagery and LiDAR, and the importance of bathymetry in the semi-analytical models that were used. These processes can alter the information contained in the pixels, and consequently the final derived products However, these effects were not evaluated in this study (Purkis and Klemas 2011).

Another source for discrepancies in the final remote sensing signal was the errors introduced by the atmospheric corrections. Since the product of obtaining bottom albedo from an airborne/satellite-derived reflectance is a subtractive process (modeled atmosphere and water column), final data may have excess or missing data, which can affect the final results.

The water column for this study was considered a well-mixed layer to the maximum penetration depth of imagery and the IOP and AOP were assumed constant though the water column. The known variations in the optical parameters variations though the water column were not considered in this study. Additionally, the measurements derived from imagery represent a water column weighted average (Gordon and Clark 1980; Zaneveld et al. 2005), while *in situ* measurements usually come from discrete depths and this mismatch in spatial scales introduces an uncertainty that is often hard to quantify.

Even considering all these limitations, the application of an appropriate algorithm for correcting the water column effects and accurately deriving important results increases the accuracy of mapping benthic habitats, including reef ecosystems.

6. References

Armstrong, Roy and Gilbes, Fernando. 2012. "Temporal and Spatial Trends in Water Optical Properties at Shallow Coral Reefs in Southwestern Puerto Rico." Glaskow, Scotland: HICO Second Users Meeting.

Arnone, Robert, Marcel Babin, Andrew H Barnard, Emmanuel Boss, Jennifer P Cannizzaro, Kendall L Carder, F Robert Chen, et al. 2006. "Reports of the International Ocean-Colour Coordinating Group Remote Sensing of Inherent Optical Properties : Fundamentals , Tests of Algorithms , and Applications." *IOCCG Report 5* 5 (5): 126. doi:10.1006/jmbi.1998.2073.

Austin, R W, and T J Petzold. 1986. "Spectral Dependence of the Diffuse Attenuation Coefficient of Light in Ocean Waters." *Optical Engineering* 25 (March 1986): 471–79. <Go to ISI>://WOS:A1986A431700017.

Bejarno Rodríguez, Ivonne. 2006. "Relationships Between Reef Fish Communities, Water and Habitat Quality on Coral Reefs," 61.

Boss, Emmanuel, Emmanuel Boss, J Ronald V Zaneveld, and J Ronald V Zaneveld. 2003. "The Effect of Bottom Substrate on Inherent Optical Properties: Evidence of Biogeochemical Processes." *North* 48: 346–54. doi:10.4319/lo.2003.48.1_part_2.0346.

Bramante, James F, Durairaju Kumaran Raju, and Sin Tsai Min. 2006. "Derivation of Bathymetry from Multispectral Imagery in the Highly Turbid Waters of Singapore ' S South Islands : A Comparative Study Background Atmospheric Correction." *Science*, 1–21.

Buiteveld, H., J.H.M. Haakvort, and M. Donze. 1994. "The Optical Properties of Pure Water." In *Proceedings of SPIE,* 2258:174–83.

Cardona-Maldonado, María a. 2008. "Assessment of Coral Reef Community Structure Using Water Optical Properties." *Unpublished Data Master Thesis*. University of Puerto Rico Mayaguez.

Collin, Antoine, and James L. Hench. 2012. "Towards Deeper Measurements of Tropical Reefscape Structure Using the WorldView-2 Spaceborne Sensor." *Remote Sensing* 4: 1425–47. doi:10.3390/rs4051425.

Collin, Antoine, Bernard Long, and Phillippe Archambault. 2011. "Benthic Classifications Using Bathymetric LIDAR Waveforms and Integration of Local Spatial Statistics and Textural Features." *Journal of Coastal Research*.

Collins, By Bill, Quester Tangent, and Mark Penley. 2007. "Lidar Seabed Classification." *Hydro International*, no. August: 19–21.

Costa, B. M., T. a. Battista, and S. J. Pittman. 2009. "Comparative Evaluation of Airborne LiDAR and Ship-Based Multibeam SoNAR Bathymetry and Intensity for Mapping Coral Reef Ecosystems." *Remote Sensing of Environment* 113 (5). Elsevier Inc.: 1082–1100. doi:10.1016/j.rse.2009.01.015.

D'Sa, Eurico J., and Richard L. Miller. 2003. "Bio-Optical Properties in Waters Influenced by the Mississippi River during Low Flow Conditions." *Remote Sensing of Environment* 84: 538–49. doi:10.1016/S0034-4257(02)00163-3.

Eakin, C. Mark, Carl Nim, Russell Brainard, Christoph Aubrecht, Chris Elvidge, Dwight Gledhill, Frank Muller-Karger, et al. 2010. "Monitoring Coral Reefs from Space." *Oceanography* 23 (4): 118–33. doi:10.5670/oceanog.2010.10.

Exelis Visual Information Solutions. 2011. "Case Study : NOAA Maps and Extracts Detailed Information about Sea Floor Habitats Using ENVI Image Analysis Software."

Gao, J. 2009. "Bathymetric Mapping by Means of Remote Sensing: Methods, Accuracy and Limitations." *Progress in Physical Geography* 33 (1): 103–16. doi:10.1177/0309133309105657.

Goodman, James a, ZhongPing Lee, and Susan L Ustin. 2008. "Influence of Atmospheric and Sea-Surface Corrections on Retrieval of Bottom Depth and Reflectance Using a Semi-Analytical Model: A Case Study in Kaneohe Bay, Hawaii." *Applied Optics* 47 (28): F1–11. doi:10.1364/AO.47.0000F1.

Gordon, H R, and O B Brown. 1974. "Influence of Bottom Depth and Albedo on the Diffuse Reflectance of a Flat Homogeneous Ocean." *Applied Optics* 13 (9): 2153–59. doi:10.1364/AO.13.002153.

Gordon, H R, and D K Clark. 1980. "Remote Sensing Optical Properties of a Stratified Ocean: An Improved Interpretation." *Applied Optics* 19 (3): 3428–30. doi:10.1364/AO.19.003428.

Gordon, H R, and W R McCluney. 1975. "Estimation of the Depth of Sunlight Penetration in the Sea for Remote Sensing." *Applied Optics* 14: 413–16. doi:10.1364/AO.14.000413.

Gordon, Howard R. 1989. "Theoretical Aspects of Hydrologic Optics." *Limonology And Oceanography* 34 (8): 1389–1409. http://www.jstor.org/stable/2837027.

Guild, L, B Lobitz, R Armstrong, F Gilbes, J Goodman, Y Detres, R Berthold, and J Kerr. 2008. "NASA Airborne AVIRIS and DCS Remote Sensing of Coral Reefs." *In Situ*, no. 17: 7–11.

Hall, D.L. David L, Senior Member, and James Llinas. 1997. "An Introduction to Multisensor Data Fusion." *Proceedings of the IEEE* 85 (1): 6–23. doi:10.1109/5.554205.

Hochberg, Eric J., Marlin J. Atkinson, and Serge Andréfouët. 2003. "Spectral Reflectance of Coral Reef Bottom-Types Worldwide and Implications for Coral Reef Remote Sensing." *Remote Sensing of Environment* 85: 159–73. doi:10.1016/S0034-4257(02)00201-8.

Holden, H., and E. LeDrew. 2000. "Accuracy Assessment of Hyperspectral Classification of Coral Reef Features." *Geocarto International* 15: 7–14. doi:10.1080/10106049908542147.

Island, Roatan, Deepak R Mishra, Sunil Narumalani, Donald Rundquist, and Merlin Lawson. 2005. "High-Resolution Ocean Color Remote Sensing of Benthic Habitats : A Case Study at the Roatan High-Resolution Ocean Color Remote Sensing of Benthic Habitats : A Case Study at."

Kirk, J.T.O. 2011. "Light and Photosynthesis in Aquatic Ecosystems" Book (Third Edition): 638.

Kutser, Tiit, Arnold G. Dekker, and William Skirving. 2003. "Modeling Spectral Discrimination of Great Barrier Reef Benthic Communities by Remote Sensing Instruments." *Limnology and Oceanography* 48: 497–510. doi:10.4319/lo.2003.48.1_part_2.0497.

Kutser, Tiit, Marian Hiire, Liisa Metsamaa, Ele Vahtmäe, Birgot Paavel, and Robert Aps. 2009. "Field Measurements of Spectral Backscattering Coefficient of the Baltic Sea and Boreal Lakes." *Boreal Environment Research* 14 (April): 305–12.

Lee, Mark. 2003. "Benthic Mapping of Coastal Waters Using Data Fusion of Hyperspectral Imagery and Airborne Laser Bathymetry." *Unpublished Data, Doctoral Thesis*.

Lee, Z, K L Carder, S K Hawes, R G Steward, T G Peacock, and C O Davis. 1994. "Model for the Interpretation of Hyperspectral Remote-Sensing Reflectance." *Applied Optics* 33 (24): 5721–32. doi:10.1364/AO.33.005721.

Lee, Z, K L Carder, C D Mobley, R G Steward, and J S Patch. 1998. "Hyperspectral Remote Sensing for Shallow Waters. I. A Semianalytical Model." *Applied Optics* 37 (27): 6329–38. doi:10.1364/AO.37.006329.

———. 1999. "Hyperspectral Remote Sensing for Shallow Waters. 2. Deriving Bottom Depths and Water Properties by Optimization." *Applied Optics* 38 (18): 3831–43. doi:10.1364/AO.38.003831.

Lee, Zhongping, Kendall L. Carder, Robert F. Chen, and Thomas G. Peacock. 2001. "Properties of the Water Column and Bottom Derived from Airborne Visible Infrared Imaging Spectrometer (AVIRIS) Data." *Journal of Geophysical Research* 106: 11639. doi:10.1029/2000JC000554.

Lee, Zhongping, Brandon Casey, Robert Arnone, Alan Weidemann, Rost Parsons, Marcos J. Montes, Bo-Cai Gao, Wesley Goode, Curtiss Davis, and Julie Dye. 2007. "Water and Bottom Properties of a Coastal Environment Derived from Hyperion Data Measured from

the EO-1 Spacecraft Platform." *Journal of Applied Remote Sensing* 1 (December): 011502. doi:10.1117/1.2822610.

Lobitz, B, L Guild, and R Armstrong. 2008. "Pre-Processing 2005 AVIRIS Data for Coral Reef Analysis." ... *International Coral Reef ...*, no. 17: 7–11. http://www.nova.edu/ncri/11icrs/proceedings/files/m17-10.pdf.

Maritorena, S. 1996. "Remote Sensing of the Water Attenuation in Coral Reefs: A Case Study in French Polynesia." *International Journal of Remote Sensing* 17 (780222585): 155–66. doi:10.1080/01431169608948992.

Maritorena, Stéphane, André Morel, and Bernard Gentili. 1994. "Diffuse Reflectance of Oceanic Shallow Waters: Influence of Water Depth and Bottom Albedo." *Limnology and Oceanography* 39 (7): 1689–1703. doi:10.4319/lo.1994.39.7.1689.

McManus, John W., and Johanna F. Polsenberg. 2004. "Coral-Algal Phase Shifts on Coral Reefs: Ecological and Environmental Aspects." *Progress in Oceanography*. doi:10.1016/j.pocean.2004.02.014.

Mishra, Deepak R., Sunil Narumalani, Donald Rundquist, Merlin Lawson, and R. Perk. 2007. "Enhancing the Detection and Classification of Coral Reef and Associated Benthic Habitats: A Hyperspectral Remote Sensing Approach." *Journal of Geophysical Research* 112. doi:10.1029/2006JC003892.

Morel, a, and B Gentili. 1993. "Diffuse-Reflectance of Oceanic Waters. 2. Bidirectional Aspects." *Applied Optics*. <Go to ISI>://A1993MH57500042.

Morel, Andre. 1974. "Optical Properties of Pure Water and Pure Sea Water." *Optical Aspects of Oceanography*. papers2://publication/uuid/B25019FC-9ED0-45D6-881A-6BE952393296.

Morel, André. 1988. "Optical Modeling of the Upper Ocean in Relation to Its Beiogenous Matter Content (case I Waters)." *Journal of Geophysical Research*.

Morel, André, Yannick Huot, Bernard Gentili, P. Jeremy Werdell, Stanford B. Hooker, and Bryan a. Franz. 2007. "Examining the Consistency of Products Derived from Various Ocean Color Sensors in Open Ocean (Case 1) Waters in the Perspective of a Multi-Sensor Approach." *Remote Sensing of Environment* 111: 69–88. doi:10.1016/j.rse.2007.03.012.

Morel, André, and Louis Prieur. 1977. "Analysis of Variations in Ocean Color." *Limnology and Oceanography* 22: 709–22. doi:10.4319/lo.1977.22.4.0709.

Mumby, P J, and a R Harborne. 1999. "Development of a Systematic Classification Scheme of Marine Habitats to Facilitate Regional …." *Biol Conserv* 88: 155–63. http://www.ncbi.nlm.nih.gov/entrez/query.fcgi?db=pubmed&cmd=Retrieve&dopt=AbstractPlus&list_uids=2005223094913786774related:luO-28f70xsJ\nhttp://linkinghub.elsevier.com/retrieve/pii/S0006320798001086.

Mumby, P. J., E. P. Green, a. J. Edwards, and C. D. Clark. 1997. "Coral Reef Habitat Mapping: How Much Detail Can Remote Sensing Provide?" *Marine Biology* 130: 193–202. doi:10.1007/s002270050238.

Otero, Ernesto, and Kelly K. Carbery. 2005. "Chlorophyll a and Turbidity Patterns over Coral Reefs Systems of La Parguera Natural Reserve, Puerto Rico." *Revista de Biologia Tropical* 53 (May): 25–32.

PACE Mission. 2015 website: http://decadal.gsfc.nasa.gov/PACE.html

Pope, R M, and E S Fry. 1997. "Absorption Spectrum (380-700 Nm) of Pure Water. II. Integrating Cavity Measurements." *Applied Optics* 36: 8710–23. doi:10.1364/AO.36.008710.

Purkis, Samuel J. 2005. "A 'Reef-up' Approach to Classifying Coral Habitats from IKONOS Imagery." *IEEE Transactions on Geoscience and Remote Sensing* 43 (6): 1375–90. doi:10.1109/TGRS.2005.845646.

Purkis, Samuel and Klemas, Victor. 2011. *Remote Sensing and Global Environmental Change*. First. Wiley-Blackwell.

Rodriguez-Guzman, Vilmaliz. 2009. "Remote Sensing of Suspended Sediment in Mayagüez Bay Associated with Inland Soil Erosion Rates." *Unpublished Data Master Thesis*. University of Puerto Rico Mayaguez.

Stephenson, Darren and Sinclair, Mark. 2006. "Hydrographic Lidar: Data Acquisition and Processing Report."

Torres, Juan L, Roy a Armstrong, Jorge E Corredor, and Fernando Gilbes. 2007. "Physiological Responses of Acropora Cervicornis to Increased Solar Irradiance." *Photochemistry and Photobiology* 83 (29): 839–50. doi:10.1562/2006-09-01-ra-1025.

Torres-Madronero, Maria C., Miguel Velez-Reyes, and James a. Goodman. 2009. "<title>Fusion of Hyperspectral Imagery and Bathymetry Information for Inversion of Bioptical Models</title>" 7473: 74730I – 74730I – 11. doi:10.1117/12.835896.

Tuell, G. H., J. Y. Park, J. Aitken, V. Ramnath, V. Feygels, and Y. Kopelivich. 2005. "Fusion of SHOALS Bathymetric Lidar and Passive Spectral Data for Shallow Water Rapid Environmental Assessment." *Oceans 2005 - Europe* 2: 1046–51. doi:10.1109/OCEANSE.2005.1513202.

Twardowski, M. S., H. Claustre, S. a. Freeman, D. Stramski, and Y. Huot. 2007. "Optical Backscattering Properties of the 'Clearest' Natural Waters." *Biogeosciences Discussions* 4: 2441–91. doi:10.5194/bgd-4-2441-2007.

Wang, Chi Kuei, and William D. Philpot. 2007. "Using Airborne Bathymetric Lidar to Detect Bottom Type Variation in Shallow Waters." *Remote Sensing of Environment* 106: 123–35. doi:10.1016/j.rse.2006.08.003.

Wang, Peng, Emmanuel S Boss, and Collin Roesler. 2005. "Uncertainties of Inherent Optical Properties Obtained from Semianalytical Inversions of Ocean Color." *Applied Optics* 44: 4074–85. doi:10.1364/AO.44.004074.

Zaneveld, J Ronald, Andrew Barnard, and Emmanuel Boss. 2005. "Theoretical Derivation of the Depth Average of Remotely Sensed Optical Parameters." *Optics Express* 13 (22): 9052–61. doi:10.1364/OPEX.13.009052.

Appendix A. Tukey HSD post hoc test for Absorption, Attenuation and Backscattering

- Tukey HSD post hoc test were the **bold** values indicate the stations that are significant different from each other.

Tukey HSD post hoc test for Absorption

Site1	Site2	Estimate	Std. Error	z value	p-value	
Enrique west	Enrique east	0.01	0.01	0.76	1	
Laurel	**Enrique east**	**-0.08**	**0.01**	**-5.79**	**1.05E-07**	*
Mario deep	**Enrique east**	**-0.08**	**0.01**	**-6.13**	**1.36E-08**	*
Mario shallow	**Enrique east**	**-0.07**	**0.01**	**-5.26**	**2.13E-06**	*
Media Luna	**Enrique east**	**-0.08**	**0.01**	**-6.01**	**2.81E-08**	*
Laurel	**Enrique west**	**-0.09**	**0.01**	**-6.55**	**8.88E-10**	*
Mario deep	**Enrique west**	**-0.09**	**0.01**	**-6.88**	**8.92E-11**	*
Mario shallow	**Enrique west**	**-0.08**	**0.01**	**-6.02**	**2.64E-08**	*
Media Luna	**Enrique west**	**-0.09**	**0.01**	**-6.76**	**2.02E-10**	*
Mario deep	Laurel	0.00	0.01	-0.34	1	
Mario shallow	Laurel	0.01	0.01	0.53	1	
Media Luna	Laurel	0.00	0.01	-0.22	1	
Mario shallow	Mario deep	0.01	0.01	0.86	1	
Media Luna	Mario deep	0.00	0.01	0.12	1	
Media Luna	Mario shallow	-0.01	0.01	-0.75	1	

Tukey HSD post hoc test for Attenuation

Site1	Site2	Estimate	Std. Error	z value	p-value	
Enrique west	Enrique east	0.00	0.02	0.13	1	
Laurel	**Enrique east**	**-0.09**	**0.02**	**-4.00**	**0.000938**	*
Mario deep	**Enrique east**	**-0.08**	**0.02**	**-3.50**	**0.006922**	*
Mario shallow	**Enrique east**	**-0.12**	**0.02**	**-5.18**	**3.42E-06**	*
Media Luna	**Enrique east**	**-0.18**	**0.02**	**-7.81**	**8.66E-14**	*
Laurel	**Enrique west**	**-0.10**	**0.02**	**-4.08**	**0.000691**	*
Mario deep	**Enrique west**	**-0.09**	**0.02**	**-3.58**	**0.005188**	*
Mario shallow	**Enrique west**	**-0.13**	**0.02**	**-5.23**	**2.54E-06**	*
Media Luna	**Enrique west**	**-0.18**	**0.02**	**-7.83**	**7.33E-14**	*
Mario deep	Laurel	0.01	0.02	0.39	1	
Mario shallow	Laurel	-0.03	0.02	-1.23	1	
Media Luna	**Laurel**	**-0.09**	**0.02**	**-3.80**	**0.002132**	*
Mario shallow	Mario deep	-0.04	0.02	-1.58	1	
Media Luna	**Mario deep**	**-0.10**	**0.02**	**-4.09**	**0.000658**	*
Media Luna	Mario shallow	-0.06	0.02	-2.53	0.17325	

Tukey HSD post hoc test for Backscattering

Site1	Site2	Estimate	Std. Error	z value	p-value	
Enrique west	Enrique east	-0.06	0.03	-1.66	1	
Laurel	**Enrique east**	**-0.18**	**0.03**	**-5.28**	**1.96E-06**	*
Mario deep	**Enrique east**	**-0.18**	**0.03**	**-5.36**	**1.24E-06**	*
Mario shallow	**Enrique east**	**-0.19**	**0.03**	**-5.46**	**7.28E-07**	*
Media Luna	**Enrique east**	**-0.23**	**0.03**	**-6.60**	**6.15E-10**	*
Laurel	**Enrique west**	**-0.13**	**0.03**	**-3.64**	**0.00405**	*
Mario deep	**Enrique west**	**-0.13**	**0.03**	**-3.70**	**0.00322**	*
Mario shallow	**Enrique west**	**-0.13**	**0.03**	**-3.82**	**0.00199**	*
Media Luna	**Enrique west**	**-0.17**	**0.03**	**-4.94**	**1.17E-05**	*
Mario deep	Laurel	0.00	0.03	0.00	1	
Mario shallow	Laurel	-0.01	0.04	-0.18	1	
Media Luna	Laurel	-0.04	0.03	-1.23	1	
Mario shallow	Mario deep	-0.01	0.03	-0.17	1	
Media Luna	Mario deep	-0.04	0.03	-1.24	1	
Media Luna	Mario shallow	-0.04	0.03	-1.05	1	

Appendix B. Multiple regressions for attenuation, attenuation and backscattering for sites in La Parguera Reserve to evaluate the relationships between rainfall of sites and the optical properties. Group 1 includes stations of Laurel, Mario Shallow, Mario Deep and Media Luna, and Group 2 includes Enrique West and Enrique East sites. Asterisk show significance of relationship.

			Estimate	**Std. Error**	**t-value**	**p-value**	
Absorption	**Group 1**	(Intercept)	-0.59595	0.01933	-30.831	2.31E-16	
		Rain	0.000516	0.000219	2.357	0.0307	*
			Estimate	**Std. Error**	**t-value**	**p-value**	
	Group 2	(Intercept)	-0.52692	0.016574	-31.793	< 2.00E-16	
		Rain	0.000683	0.000188	3.642	0.00201	*
			Estimate	**Std. Error**	**t-value**	**p-value**	
Attenuation	**Group 1**	(Intercept)	-0.42325	0.034186	-12.381	6.23E-10	
		Rain	-0.00019	0.000387	-0.479	0.638	
			Estimate	**Std. Error**	**t-value**	**p-value**	
	Group 2	(Intercept)	-0.33633	0.032624	-10.309	9.89E-09	
		Rain	0.000135	0.000369	0.367	0.718	
			Estimate	**Std. Error**	**t-value**	**p-value**	
Backscattering	**Group 1**	(Intercept)	-1.06261	0.134498	-7.901	6.52E-07	
		Rain	-0.0042	0.001582	-2.652	0.0174	*
			Estimate	**Std. Error**	**t-value**	**p-value**	
	Group 2	(Intercept)	-0.91725	0.114207	-8.031	5.27E-07	
		Rain	-0.00393	0.001343	-2.923	0.00996	*

Chapter 4: Benthic Habitat Map of La Parguera Reserve using Passive and Active Remote Sensing Data

Abstract

Knowledge of benthic habitats and their spatial distribution is vital for understanding complex coral reefs systems. The complexity and heterogeneity of shallow coastal waters over small spatial scales provides a challenging environment for mapping and monitoring benthic habitats using remote sensing imagery. High-resolution benthic habitat maps were developed from AVIRIS and WV2 modeled bottom albedo products from pre-processed imagery (atmospheric and water column corrected) for La Parguera Reserve. An ISODATA classification was performed with an initial high clustering that was gradually reduced to 10 clusters. The segmented images were converted to polygons and exported to ESRI ArcMap 10.3 where Spatial Join was performed with ground validation points to classify the polygons. The classes were: coral reefs, seagrass, hardbottom, mixed sand/hardbottom/coral, mud, sand, and sand with benthic algae. An accuracy assessment was performed were the overall accuracy (AVIRIS = 63.55%, WV2 = 64.81%), kappa coefficient (AVIRIS = 55 %, WV2 = 57%), and the tau coefficient (AVIRIS = 59%, WV2 = 60%) were evaluated. No major class differences were found between the AVIRIS and WV2 classification totals, except for coral reefs and sand classes' totals. The reduction in coral reefs class totals could be attributed to temporal differences of the images depicting changes in the coral reefs distribution within the reserve. The overall accuracies were lower when compared with other studies using similar object based methods. However, these areas were relatively small, with shallow clear waters, and not as optically complex as our study area. A major contribution of this study was the creation of the first benthic habitat map for La Parguera Reserve that: 1) provided multi/hyperspectral information at this

spatial scale (4 square meters), 2) covered the extent of the reserve, and 3) provided a baseline for future development of benthic habitat studies using an objective classification scheme.

1. Introduction

Coastal zones face significant threats from many factors, including sea level rise, increased hurricane intensity, coastal erosion, urbanization, loss of coastal wetlands and biodiversity, and marine pollution (UNEP 2006). Airborne and satellite remote sensing techniques have been employed by many researchers to map general benthic habitat types (e.g., sand, seagrass, coral reefs, hard substrate) in coral reef environments. Knowledge of benthic habitats and their spatial distribution is vital for understanding complex coral reefs systems. Benthic habitat maps are important for assessing patterns, identifying area of habitat diversity and determining habitat coverage. Also, coral reef habitat maps based on remotely sensed data are a fundamental tool for management because they summarize ecologically meaningful information across extensive geographic scales in a cost-effective manner (Mumby and Harborne 1999).

The complexity and heterogeneity of shallow coastal waters over small spatial scales provides a challenging environment for mapping and monitoring benthic habitats using remote sensing imagery (Lesser and Mobley 2007). Coral reef habitat maps, derived from remotely sensed data, play a role in decision-making, and is imperative for these maps to be produced both as accurately and cost effectively as possible (Bejarano et al. 2010).

Reef studies using satellite imagery have typically discerned several types of benthic cover in the shallow water marine environment in clear water conditions: corals and hard bottom,

unconsolidated sediments such as sand and mud, and submerged aquatic vegetation (SAV) (Green et al. 2000; Roelfsema et al. 2002; Hochberg et al. 2003). These habitats comprise the complex coral reef ecosystem. Habitat mapping efforts reported in the scientific literature have employed very similar methodological strategies overall; where the maps are produced by interpreting continuous coverage, environmental data layers, often derived from remote sensing data, and using biological information about habitats obtained from *in situ* sampling and observation of the seabed (ground-thruthing) (Brown et al. 2011). These approaches assumes that the final map is a prediction of the distribution of seabed habitats, with the complete coverage environmental data acting as a proxy for the habitat data (MESH 2008).

The use of classifications from digital imagery are generally divided into photo interpretation and approaches or object-oriented classification approaches, the latter consisting of supervised or unsupervised classifications (Green et al. 2000). Lillesand et al. (2004) stated that a supervised approach uses samples of known information classes (training sets) as a guide to automatically classify pixels of unknown identity. Jensen (1996) emphasized that the accuracy of a supervised classification depends largely on the quality of the training data. Sugumaran et al. (2003) discouraged using a supervised classification approach because this high spectral heterogeneity would increase the number of errors and the high heterogeneity would require a large number of training sets for a complete classification. The unsupervised classification approach is founded on the natural inherent grouping of spectral values within an image (Lillesand et al. 2004), where the image is segmented in spectral clusters, and then labeling of the clusters based on ground truth data or other sources. Lang (2007) stated that the classification accuracy dramatically

improved with higher numbers of initial cluster classes for an unsupervised classification approach on high-resolution imagery.

Several approaches and sensors have been used for developing benthic habitat maps or bottom composition. Kautsky et al. (2010) summarized some prevailing technologies in the developing of this habitat maps using: medium to very high spectral resolution satellite and airborne passive sensor, multispectral and hyperspectral sensors, active sensors, and fusion and of active and passive sensors. Brown et al. (2011) also presents that although the specific methods used to derive habitat maps vary considerably, these can be generally categorized into: abiotic surrogate mapping, assemble first, predict later (unsupervised classification), and predict first, assemble later (supervised classification).

Nevertheless, benthic habitat maps provide baseline data to effectively measure the results of restoration efforts and management and evaluate potential future changes, especially in MPA and other natural reserves (Bauer et al. 2012).

Landsat Thematic Mapper (TM) and Enhanced Thematic Mapper (ETM+) imagery for eastern Puerto Rico, collected January of 1985 and March of 2000, was used to perform a multi-temporal classification technique to identify and quantify the dynamics of submerged aquatic vegetation (seagrass and macroalgae) in a study area located in Vieques Sound, off the east coast of Puerto Rico (Shapiro and Rohman 2006).

The use of high-resolution imagery (AVIRIS and WV2) provides more visual information for interpretation and assessment than previously possible with lower resolution imagery such as Landsat (Sawaya et al. 2003). Mumby et al. (1998) reported an overall accuracy for CASI sensor

(81%) and Landsat TM (31%) for the thematic maps of reef habitats (nine classes) in South Caicos, Turks and Caicos. An overall accuracy of coarse-level habitat maps was achieved by Mumby and Edwards (2002) in the Turks and Caicos for IKONOS (75%), Landsat TM (73%), and SPOT XS (67%). Mishra et al. (2007) reported an overall accuracy of 83.6% for a hyperspectral AISA image and 80.6% for an IKONOS image in Roatan Islands, Honduras. The map classification produced an overall accuracy of 69% for seven classes for an IKONOS image for an area of approximately 10.5 Km^2 in the Arabian Gulf (Purkis 2005). Additionally, Bejarano et al. (2010) summarized overall accuracies obtained by other studies on coral reef areas using object base classification techniques.

These benthic habitat classification maps have been developed for areas within La Parguera Reserve, which included small cays and islands, but only some studies have covered the entire reserve. The most notable being the benthic habitat map for Puerto Rico and the US Virgin Islands developed by NOAA/NOS/Bio-geography Team, (Kendall et al. 2001). Unfortunately, these maps lacked information of important areas of the shelf that cover our study area and the development of these maps can be time consuming (aerial photo interpretation) and the accuracy of the map scale used (1 acre minimum map unit) limits the information that can be evaluated for habitat distribution.

An update to this benthic habitat was performed for some areas in southwestern of Puerto Rico. This mapping effort refined the existing NOAA benthic habitat maps for the study area where the two major improvements were: reduce the minimum mapping unit from one acre to 1000 square meters (~1/4 acre), and increased coverage into areas formerly classified as unknown

(Bauer et al. 2012). A new classification scheme was used where digital satellite imagery was visually interpreted and habitats were then delineated in a hierarchical classification scheme.

(Arce Arce 2005) developed a benthic habitat map for La Parguera insular shelf based on a comparison of two sensors with different spatial and spectral resolution, IKONOS (1 m, 4 bands) and Hyperion (30 m, 220 bands). The classification on the bottom types was limited to seagrass, sand and corals and presented some limitations in the overall accuracy of identifying areas of corals. Also this project was focused in the inner shelf area of La Parguera Reserve and does not include deeper areas were benthic habitat discrimination is using passive sensors is more complex.

Further improvements on the map scale and spatial resolution were achieved by (Prada, et al. 2008) when a map scale of 400 square meters and 4 square meters were achieved for areas on La Parguera shelf. These employed the use of an active sensor (Side Scan Sonar) to determine the benthic habitat based on visual interpretation and ground truth data. However, this approach did not provide important information of the optical properties of the water column or bottom albedo, and the maps product was based on image (photo) interpretation.

Bioptical models were used by (Torres-Madronero et al. 2009) in conjunction with hyperspectral imaging in inversion procedures for mapping benthic habitats. The results presented an improvement in obtaining accurate bottom abundances by fusing high-resolution bathymetry with both simulated hyperspectral and AVIRIS hyperspectral imagery. This improvement allowed bottom abundance estimates to be obtained from 5-10 meters beyond what can be

obtained from hyperspectral imaging alone in clear waters. This study was limited to some offshore cays around La Parguera Reserve.

(Zayas-Santiago 2011) developed two benthic habitat maps from an IKONOS image for two offshore cays within La Parguera Reserve (Cayo Enrique and Cayo Laurel). These maps were generated with seven classes using a supervised classification after applying a water column correction using depth-invariant bands (Lyzenga 1981).

A new approach was presented were Exelis ENVI software was used to extract and fuse information from sonar, LiDAR and optical imagery so that sea floor depths and habitats (Exelis Visual Information Solutions 2011). The data were used to calculate slope, rugosity and curvature in ArcGIS, which emphasize the differences between habitats on the sea floor. As part of their preprocessing work, Principle Component Analysis (PCA) was used to reduce redundancy in the data and to better understand the complexity on the sea floor. This information, along with ancillary data such as intensity information, was loaded into ENVI, allowing the researchers to draw distinctions between softer and harder sediments in flatter areas of the sea floor.

The purpose of this project was to present how methods and technology from passive sensors can be used to develop a high-resolution benthic habitat map. These benthic maps were derived from two sources: AVIRIS modeled bottom albedo and the WV2 modeled bottom albedo. Additional products based from the analysis of these benthic habitat maps included the quantification of changes in the coral reef and seagrass distribution in La Parguera Reserve.

1.2 Objectives

The specific objectives were:

- Development of benthic habitat maps based on:
    - AVIRIS-modeled bottom albedo
    - WV2-modeled bottom albedo
- Identify ecologically important habitats and changes in distribution of these habitats in La Parguera when compared to similar map products for the area. Additional identification of other areas of unconsolidated sediments (sand, mud) to be used for management and other recreational activities within the reserve.
- Quantify changes in the distribution of coral reefs in the reserve.
- Improve the methods for developing objective-based classifications from high-resolution satellite imagery products after applying corrections for the water and atmosphere.

2. Methods and Materials

2.1 Image Preprocessing

The imagery and data were preprocessed first to enable spatial correlations before further analysis. These corrections included data resampling, radiometric corrections to transform data from at sensor radiance to remote sensing reflectance, and atmospheric corrections to determine the contribution of the atmosphere to the signal.

2.1.1 AVIRIS

Data preprocessing was done using the Exelis ENVI 5.0 computer program. The AVIRIS image was evaluated for data gaps and a subset of the image was made based on the La Parguera Reserve polygon. The original spatial resolution of the AVIRIS image was 3.1 meters. The image was resampled to 4 meters to match the spatial resolution of the LiDAR bathymetry image. Data from the AVIRIS image was atmospherically corrected using TAFKAA (Lobitz, et al. 2008) and a water column correction was applied (Lee et al. 1999; Mishra et al. 2007). The final product used was an image of remote sensing reflectance of the bottom (Rrs_b).

2.1.1 WV2

The WorldView 2 (WV2) image was radiometrically corrected before any additional processing was performed. The radiometric correction used was the WorldView Radiance calibration routine in ENVI 5.0, which converts relative radiance into absolute radiance in units of ($\mu W / cm^2$ *nm*sr) based on the calibration factor for each band. The WV2 image was evaluated for data gaps and a subset of the image was made based on the La Parguera Reserve polygon. The original spatial resolution of the WV2 image was 1.86 meters, but the image was resampled to 4

meters to match the spatial resolution of the LiDAR image. The WV2 image was warped for the co-registration with the LiDAR image and both were set to the coordinate system World Geodetic Survey 84 (WGS-84). A total of 40 points were used as ground control points for the registration and the total RMSE for the co-registration was 0.5 meters. Data from the WV2 image was atmospherically corrected using Cloud Shadow Approach (CSA) (Lee et al. 2007) and a water column correction was applied (Lee et al. 1999; Mishra et al. 2007). The final product used was image of remote sensing reflectance of the bottom (Rrs_b).

2.1.3 LiDAR SHOALS reflectivity image

Data processing for the LiDAR reflectivity image was done using Exelis ENVI 5.0 computer program. A subset of the image was created using the La Parguera Reserve polygon. The AVIRIS image was used as the base image for the co-registration with the LiDAR reflectivity image and both were set to the coordinate system NAD 1983 State Plane Puerto Rico USVI (FIPS 5200). A total of 40 points were used as ground control points for the registration and the LiDAR reflectivity image was warped to match the AVIRIS image. The total RMSE for the co-registration was 0.5 meters. A final LiDAR reflectivity image was obtained and was used in the development of the benthic map from the active sensor.

2.2 Ancillary data

The images were corrected for fluctuations in tide readings and these were measured at the Magueyes Island Tide Station (Station ID 9759110) in La Parguera, Lajas, Puerto Rico (NOAA, Tide and Currents 2005). The WV2 imagery was acquired in December 4, 2011 (15:25 GMT) and tide reading for this station was 0.249 meters at MLLW (15:24 GMT) (NOAA Tide and

Currents 2011). The LiDAR SHOALS bathymetry data was processed and corrected for errors in position and tidal changes (Stephenson and Sinclair 2006).

2.3 Benthic Habitat Mapping

The process of producing seafloor habitat maps cuts across the disciplines of marine biology, ecology, geology, hydrography, oceanography and geophysics, and involves the combining of disparate datasets from these disciplines to produce simplified spatial representations of the seafloor relating to the distribution of biological characteristics (Brown et al. 2011).

2.3.1 Benthic Habitat Classification

A classification scheme was developed prior to implementing any image segmentation or classification. These nine aquatic feature classes were selected on the basis of the availability of sufficient replication of ground control data to verify feature locations The following categories were included: (1) Coral Reefs, (2) Seagrass, (3) Hardbottom, (4) Mix: Sand/Hardbottom/Coral, (5) Mud, (6) Sand, (7) Sand with Benthic Algae. This classification was based on the sites that could be obtained by field data, and limitations presented by other research in obtaining benthic classification from passive and active sensors (Tulldahl 2013; Cedeira-Estrada, 2011; Mishra et al. 2007 and 2005; Mumby and Edwards 2002). A detailed description of the categories for classification is included in Appendix A.

The Iterative Self Organizing Data (ISODATA) algorithm is an unsupervised classification and was used on the AVIRIS-modeled bottom albedo (passive sensor), WV2-modeled bottom albedo (passive sensor), and the LiDAR reflectivity image to derive spectral clusters or classes (Purkis

and Klemas 2011; Jensen 2006). According to Lang (2007), an increase in the number of clusters, increases the accuracy in an ISODATA classification in high-resolution imagery. Various iterations and combinations of maximum clusters were evaluated. All bands from the AVIRIS albedo image (32 bands) and the WV2 image (5 bands) were used in the ISODATA classification process. A total of 150 clusters with 5 iterations were selected as the maximum for the ISODATA classification to evaluate a complete distribution of the pixels in the image. This approach accounted for the considerable spectral heterogeneity of the classes from the ISODATA and effectively identified the heterogeneous pixels belonging within each specific class / benthic habitat. Some spectral clusters that appeared to belong to multiple class / benthic habitat (confused pixels) were also identified. Additionally, the ISODATA classifier was performed to the AVIRIS image and WV2 images without the water column correction. An evaluation of the images was done to compare the influence of the water column correction in the classification of the images.

2.3.2 Field Data for Ground Validation and Accuracy Assessment

A total of 550 points were used for the ground validation and accuracy assessment of the images. This point data was obtained from different sources that included *insitu* data collected by (Bauer et al. 2012) for this area during 2011 and included 207 ground validation sites and 223 accuracy assessment sites for La Parguera Reserve. The points were mainly collected using dropcamera techniques and the recorded video or images were analyzed for our classification in terms of accuracy of our classes. Additional sites were collected in 2014 and some previous sites were revisited to evaluate any temporal changes in the original data. A total of 135 new sites were sampled and the surveying techniques included drop camera (Delta Vision HD camera with

digital video recorder (DVR) and visual inspection from boat for very shallow sites. A Trimble Juno 3D GPS receiver was used to collect the locations of the drop camera sites. The GPS was set to record a 10 second average point that coincided with the 10 second high definition video recorded for each site. A total of 225 sites were selected for the ground validation and 325 sites were selected for the accuracy assessment.

2.3.3 Ground Validation

Once the images were divided into clusters from the ISODATA classification, the images were converted to polygons and processed in ESRI ArcMap 10.3. These clusters were assigned to a class using a Spatial Join Tool were the polygon acquired the class attribute from the point data collected for ground validation. The Spatial Join Tool based the joining of classes on spatial location, that is, that the polygon obtains the class attribute from the point within that polygon. Additionally, if no point data is available within the polygon, the attribute of the nearest point is collected and a distance value is recorded. This procedure ensured that all polygons were aggregated and assigned to a specific benthic habitat category, even when ground validation point data was limited. The final polygon layer were aggregated based on the benthic class using the Dissolve Tool from ESRI ArcMap 10.3.

2.3.4 Accuracy Assessment

An accuracy assessment was performed to the classified polygon data using the point data selected for the accuracy assessment. A Spatial Join Tool was used where the point data extracted the class attribute from the polygon layer data based on location.

To verify the accuracy of the benthic map an error matrix was made to ensure the reliability of the results. This matrix was calculated by the comparison of the location and class of each ground truth point with the corresponding location and class in the classified image and provided metrics of overall accuracy, producer accuracy and user accuracy for each class, and the kappa coefficient. The overall accuracy is calculated by the sum of the number of polygons classified correctly divided by the sum of all the polygons in the entire ground truth classes. Producer accuracy is the probability that a pixel in the classification image is put into class x given the ground truth class is x. User Accuracy is the probability that the ground truth class is x given a pixel is put into class x in the classification image (Jensen 1996). The kappa coefficient is a measure of the proportional (or percentage) improvement by the classifier over a purely random assignment to classes and defines the extent to which the correct values of an error matrix are due to "true" versus "chance" agreement. This coefficient can also account for the proportionate reduction in error generated by a classification process, compared with a completely random classification (Sim and Wright 2005).

A final benthic habitat classification maps were produced for the AVIRIS-modeled bottom albedo (passive sensor) and WV2-modeled bottom albedo (passive sensor). These products were evaluated for accuracy and also compared with other benthic maps produced for the study area.
A summary of the methods used for the development of the benthic habitat map is included in Figure 1.

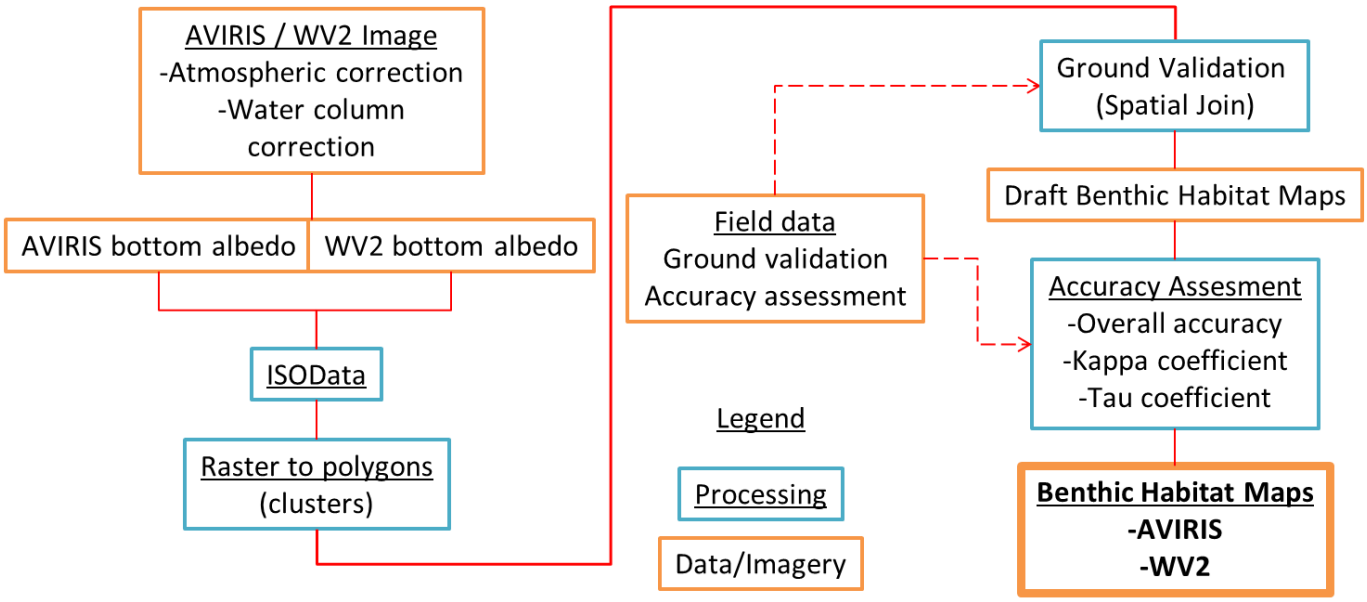

Figure 1: Flow chart of the processing (blue) and data (orange) used in the development of the benthic habitat map for la Parguera Reserve.

3. Results

3.1 ISODATA

The images were evaluated with the unsupervised ISODATA classifier. For the AVIRIS and the WV2 a total of 150 clusters were determined from the ISODATA classifier (Figure 2). Additionally, the ISODATA classifier was applied to the AVIRIS and WV2 images without the water column correction (Figure 3). The raster images were transformed to polygons in ESRI ArcMap to be classified and verified using the field data points (Figure 4).

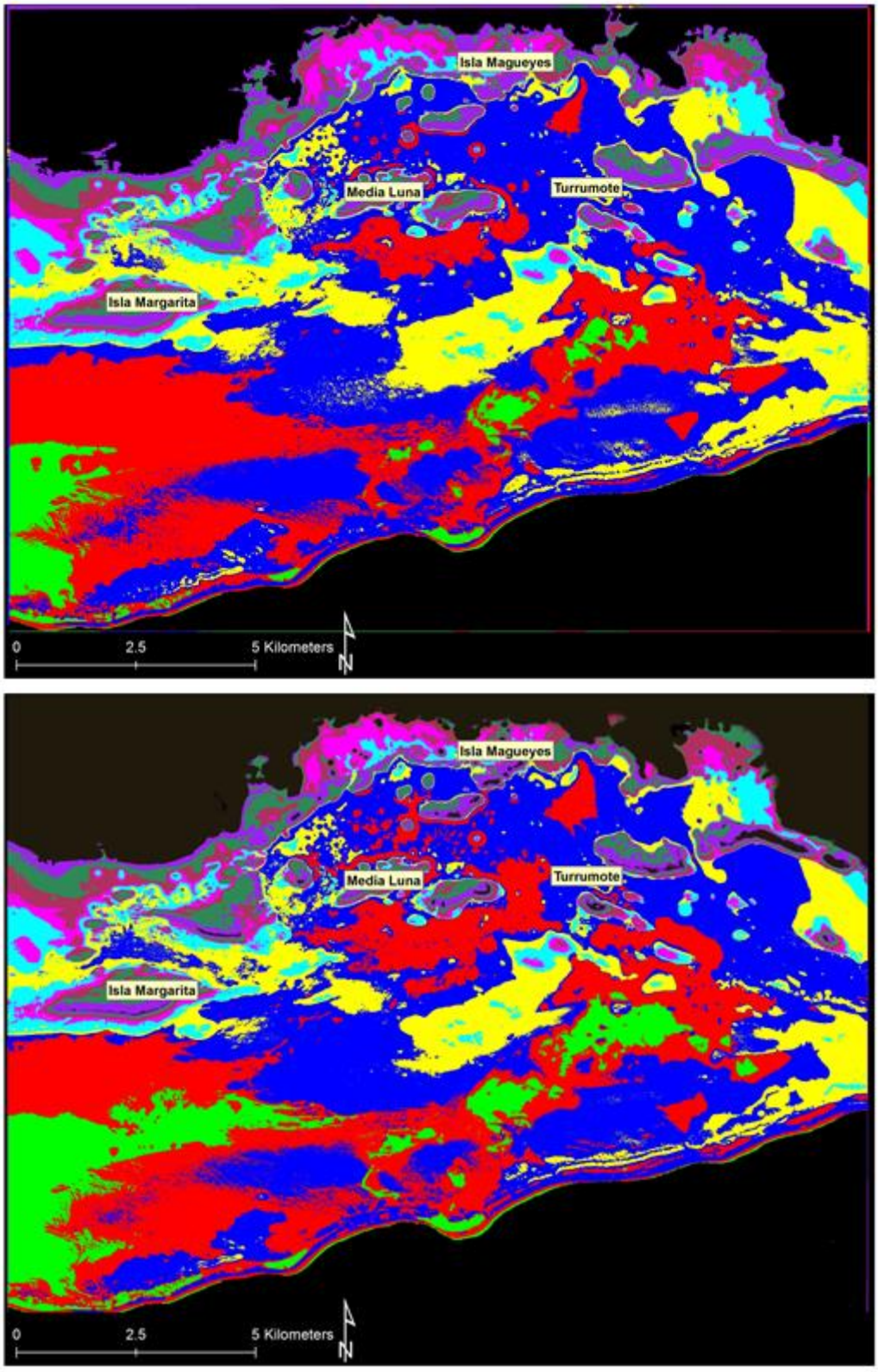

Figure 2: ISODATA unsupervised classification for AVIRIS (top) and WV2 (bottom) bottom albedo images after water column correction. The colors only represent different clusters.

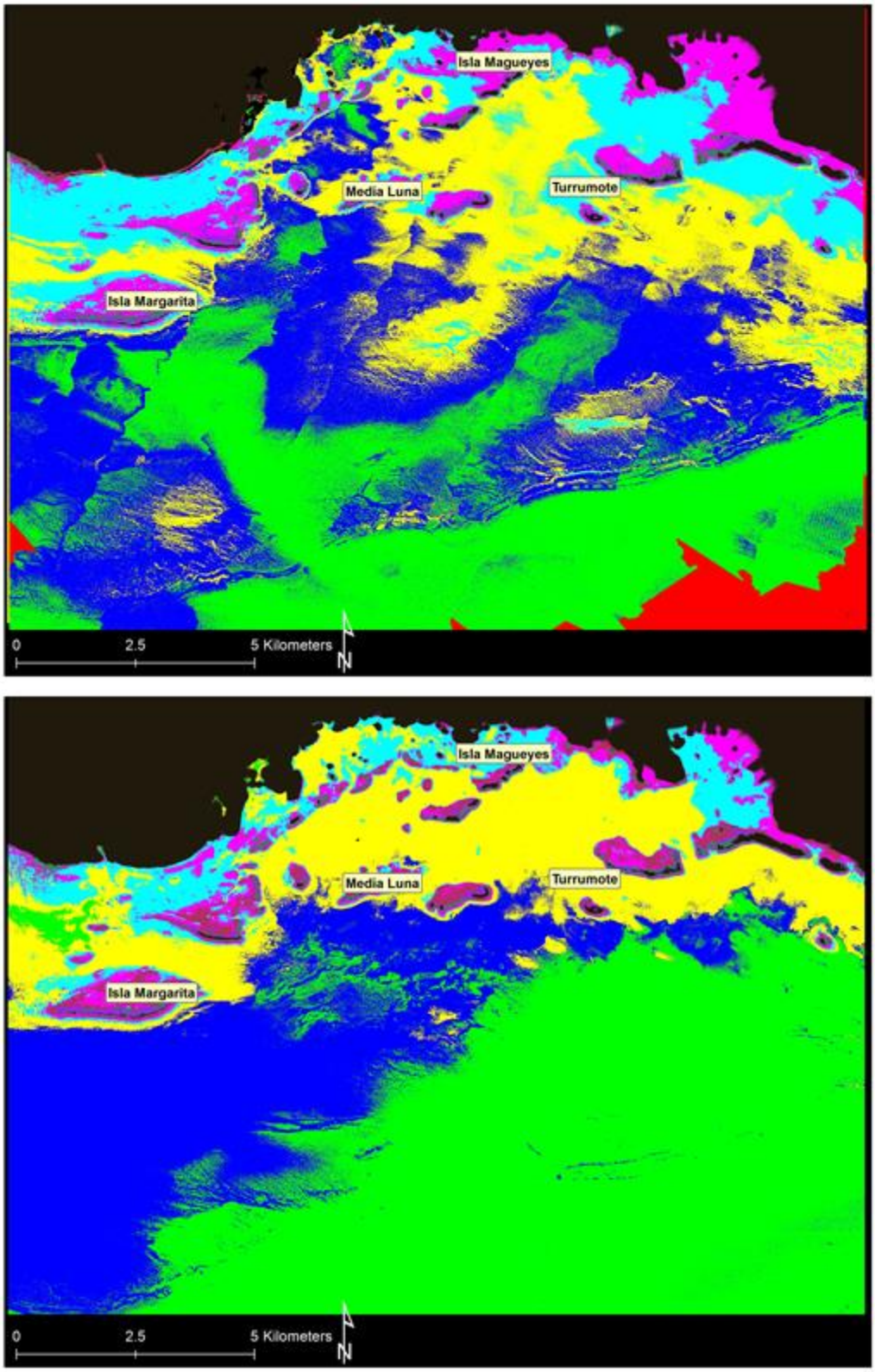

Figure 3: ISODATA unsupervised classification for AVIRIS (top) and WV2 (bottom) above water remote sensing reflectance. The colors only represent different clusters.

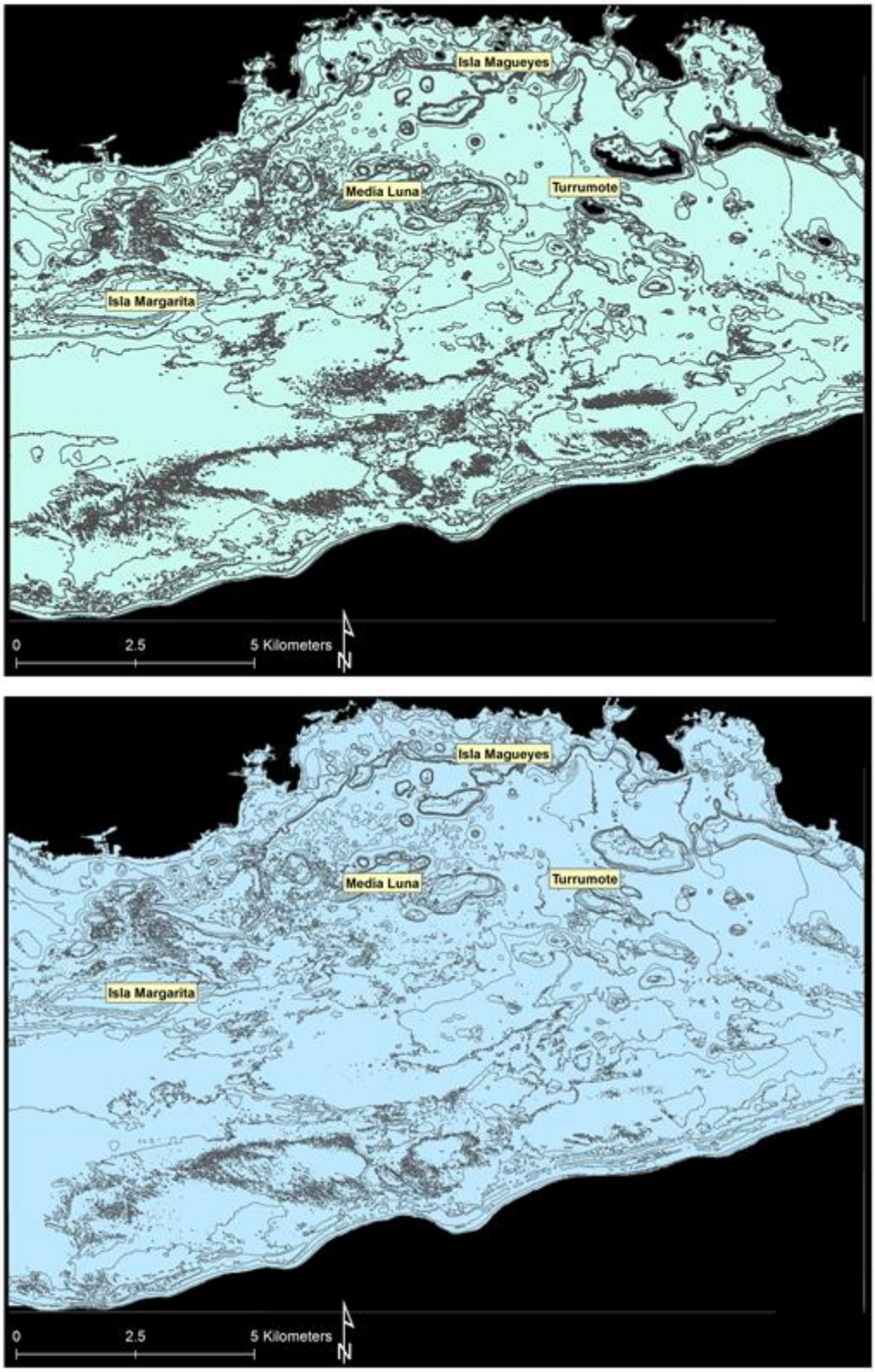

Figure 4: Polygon clusters transformed from the ISODATA for AVIRIS (top) and WV2 (bottom).

A total of 550 field points were available that included 225 for ground validation and 325 for accuracy assessment (Figure 5). For a complete list of ground validation and accuracy assessment points with coordinates and habitat description see Appendix B.

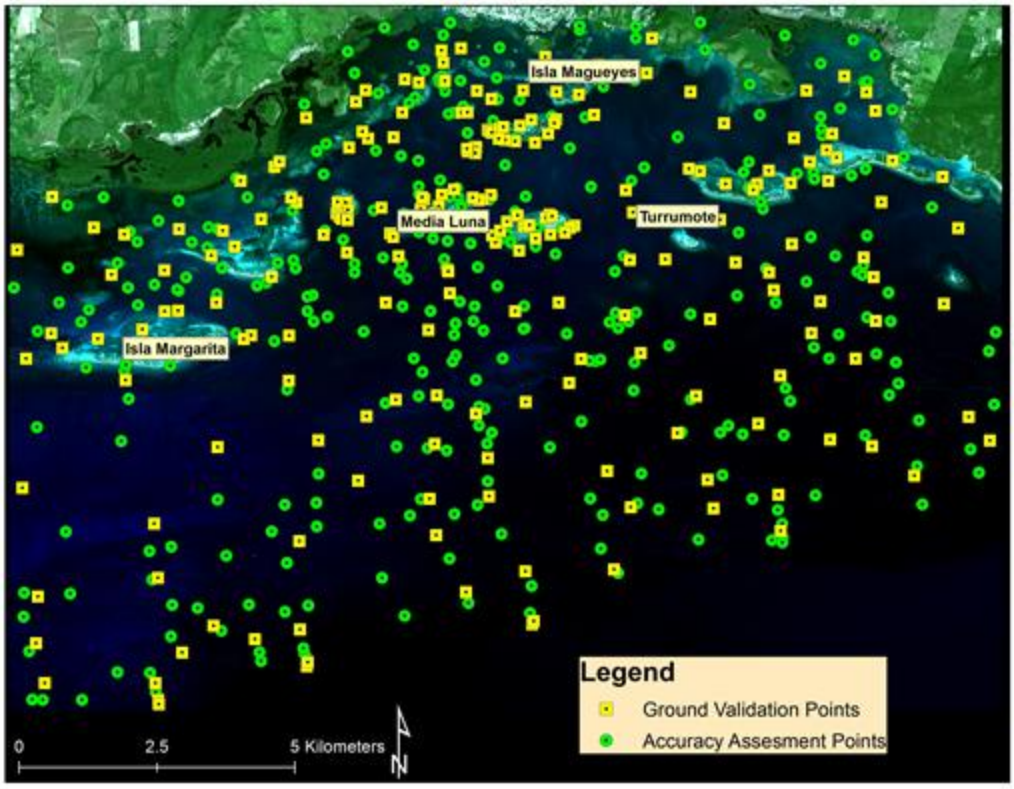

Figure 5: Field ground validation (yellow-box) and accuracy assessment (green-circle) points.

The polygons were classified using the Spatial Join Tool using the ground validation data and classes selected (Figure 6).

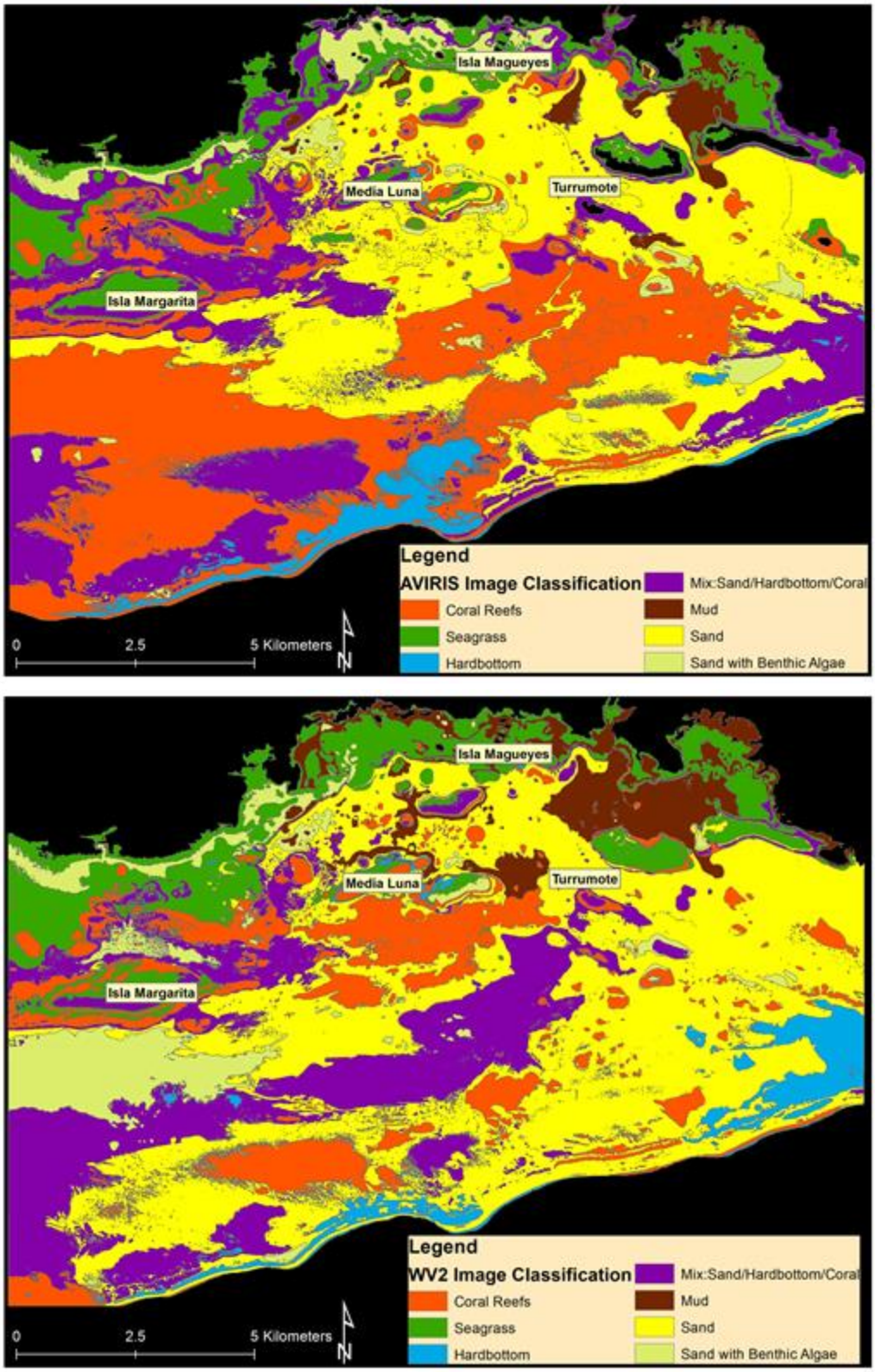

Figure 6: Image classification for AVIRIS (top) and WV2 (bottom) for 7 classes.

These polygons were classified to produce a benthic class map. A summary of the class distribution and coverage was included for each classified image (Table 1).

AVIRIS Image					
Benthic Class	**Total polygons**	**Total Area (Km^2)**	**Percentage Class**	**Average Depth of Class (m)**	**Ground Validation Points**
Coral Reefs	10,822	50.32	30%	18.73 (min. 0, max. 45)	68
Seagrass	2,169	15.44	9%	7.14 (min. 0, max. 22)	40
Hardbottom	883	4.95	3%	21.29 (min. 0, max. 43)	14
Mix: Sand/Hardbottom/Coral	5,153	33.92	20%	15.52 (min. 0, max. 41)	42
Mud	917	3.50	2%	9.26 (min. 0, max. 22)	11
Sand	1,539	53.50	32%	16.19 (min. 0, max. 46)	27
Sand with Benthic Algae	1,885	6.61	4%	12.86 (min. 0, max. 34)	23
TOTAL	**23,368**	**168.24**	**100%**	**14.42**	**225**
WV2 Image					
Benthic Class	**Total polygons**	**Total Area (Km^2)**	**Percentage Class**	**Average Depth of Class (m)**	**Ground Validation Points**
Coral Reefs	11,652	22.89	14%	17.02 (min. 0, max. 43)	68
Seagrass	2,268	18.24	11%	6.91 (min. 0, max. 22)	40
Hardbottom	1,226	6.28	4%	21.27 (min. 0, max. 43)	14
Mix: Sand/Hardbottom/Coral	4,447	30.95	18%	16.91 (min. 0, max. 40)	42
Mud	864	10.56	6%	8.76 (min. 0, max. 23)	11
Sand	1,452	67.27	40%	18.56 (min. 0, max. 46)	27
Sand with Benthic Algae	1,953	12.20	7%	13.21 (min. 0, max. 34)	23
TOTAL	**23,862**	**168.39**	**100%**	**14.66**	**225**

Table 1: A summary of the classification for AVIRIS and WV2 images. These include the total polygons, total area, percentage of class, average of class, and ground validation points.

An accuracy assessment was performed to the classified images using the Spatial Join Tool with the field validation data selected for accuracy assessment. An error matrix was developed to provide metrics of overall accuracy, producer accuracy and user accuracy for each class, and the kappa coefficient (Table 2).

AVIRIS Image Classification

Classified Data	Truth Data: Coral Reefs	Seagrass	Hardbottom	Mix: Sand/Hardbottom/Coral	Mud	Sand	Sand with Benthic Algae	TOTAL	PRODUCER ACCURACY
Coral Reefs	62	5	6	13	0	0	6	**92**	**67.39%**
Seagrass	4	33	1	4	0	0	2	**44**	**75.00%**
Hard Bottom	2	0	12	1	0	0	1	**16**	**75.00%**
Mix: Sand/Hardbottom/Coral	13	13	2	40	0	0	7	**75**	**53.33%**
Mud	0	4	0	0	13	0	1	**18**	**72.22%**
Sand	11	4	0	4	7	25	1	**52**	**48.08%**
Sand with Benthic Algae	0	2	0	0	0	3	19	**24**	**79.17%**
TOTAL	**92**	**61**	**21**	**62**	**20**	**28**	**37**	**321**	
USER ACCURACY	**67.39%**	**54.10%**	**57.14%**	**64.52%**	**65.00%**	**89.29%**	**51.35%**		

Overall Accuracy	Kappa Coefficient	Tau Coefficient
63.55%	**0.55**	**0.59**

WV2 Image Classification

Classified Data	Truth Data: Coral Reefs	Seagrass	Hardbottom	Mix: Sand/Hardbottom/Coral	Mud	Sand	Sand with Benthic Algae	TOTAL	PRODUCER ACCURACY
Coral Reefs	65	5	2	13	0	2	2	**89**	**73.03%**
Seagrass	6	36	0	2	0	1	5	**50**	**72.00%**
Hard Bottom	1	0	12	1	0	2	0	**16**	**75.00%**
Mix: Sand/Hardbottom/Coral	9	7	2	40	0	0	5	**63**	**63.49%**
Mud	0	5	0	0	15	0	2	**22**	**68.18%**
Sand	9	5	5	6	5	23	4	**57**	**40.35%**
Sand with Benthic Algae	1	7	0	0	0	0	19	**27**	**70.37%**
TOTAL	**91**	**65**	**21**	**62**	**20**	**28**	**37**	**324**	
USER ACCURACY	**71.43%**	**55.38%**	**57.14%**	**64.52%**	**75.00%**	**82.14%**	**51.35%**		

Overall Accuracy	Kappa Coefficient	Tau Coefficient
64.81%	**0.57**	**0.60**

Table 2: An accuracy assessment for the image classification of the AVIRIS and WV2 bottom albedo images. This summary includes an error matrix, user and producer accuracy, overall, accuracy, kappa coefficient and tau coefficients for the selected classes.

4. Discussion

4.1 ISODATA

The selected bottom albedo images from the AVIRIS and WV2 data provided the required information for a benthic habitat classification. The ISODATA classification was selected, because this approach accounted for the considerable spectral heterogeneity in the images (Lang et al. 2007). An initial 150 clusters and 5 iterations were used, where the spectral clusters that appeared to belong to multiple class / benthic habitat (confused pixels) were also identified and removed, the homogenous segmented pixels were preserved. These confused clusters were reprocessed and combined until a final image of 10 clusters was produced. This method reduced the processing time of confused pixels and provided a manageable classification of clusters.

The removal of the atmospheric and water column influence improved the retrieval and segmentation of clusters. The AVIRIS image without the water column correction (Figure 3) presented very poor discrimination of bottom features, especially in deeper areas when compared to the AVIRIS bottom albedo image (Figure 2). Also, cross-track illumination and water column constituents (ie. CDOM, phytoplankton) were present and separated in the uncorrected image. The bottom features were not distinguishable in deeper areas of the WV2 image without the water column correction (Figure 3), compared to the WV2 bottom albedo image (Figure 2). Shallow water features in the offshore cays were identified and segmented and a “dark water” area was also segmented from the ISODATA routine. The application of water column correction improved the retrieval of bottom features in both high-resolution images (Green et al. 2000).

4.2 Ground Validation

The images were converted from raster to polygons and later classified using the ground validation points (Figure 4). A total of 225 points were used for the ground validation. The Spatial Join allowed for all points to be classified regardless of distance from the ground validation point (Figure 5). Also, this technique allowed an objective identification of the closest ground validation point, removing the classification bias from the supervised classification and maintaining the objective based approach in the image segmentation of the unsupervised classification. The image classification was completed to the AVIRIS and WV2 bottom albedo images with 7 benthic classes (Figure 6)

The classified images cover an area from 168.24 square kilometers (AVIRIS) to 168.39 (WV2) square kilometers. These minor discrepancies in the total area were due to the different land masked areas in both images. When comparing the total area for individual classes, most of the classes were relatively close in terms of total area per class. The seagrass class in AVIRIS was 9%, while the WV2 was 11%; the hardbottom class in AVIRIS was 3%, while the WV2 was 4%; the mix:sand/hardbottom/coral class in AVIRIS was 20%, while the WV2 was 18%; the mud class in AVIRIS was 2%, while the WV2 was 6%; the sand with benthic algae class in AVIRIS was 4%, while the WV2 was 7% (Table 1).

The most predominant classes exhibited major difference in the total area of coverage for class for each sensor. The coral reefs class total area for AVIRIS was 30%, while for the WV2 was only 14%. Also, the sand class total area exhibited a major difference from the AVIRIS (32%) to the WV2 sand class (40%). These differences were attributes to the segmentation process of the ISODATA clusters. Although the total area for both images (all classes) were very similar, the

total area for the coral class decrease significantly from the AVIRIS image (50.32 km^2) to the WV2 image (22.89 km^2). However, there was an increase in the total polygons from the AVIRIS image (10,822) to the WV2 image (11,652), indicating that the size of the polygons for this class were larger in the AVIRIS image (Table 1). A different process occurred with the sand class, were the total area was increase from 53.50 km^2 in the AVIRIS classification to 67.27 km^2 in the WV2, but the total polygons decreased from 1,539 in the AVIRIS classification to 1,452 in the WV2. Also, the availability of ground validation points did not affect the distribution of the total areas for each class, since the total areas do not correlated to the quantity of points available.

Higher values were expected from the mix: sand/hardbottom/coral class, since this class had features from sand, hardbottom, coral or a combination that could not be separated into different classes. However, this class total area of coverage was very similar in both images (AVIRIS = 20%; WV2 = 18%) indicating that both images were equally effective in detecting this mix class, and also indicated similarities in the bottom albedo image. This high value in this mix class was attributed to this class containing features of both coral reefs and sand, the two highest classes obtained from the classifications.

4.3 Accuracy Assessment

4.3.1 Overall Accuracy

To verify the accuracy of the classification of the benthic maps, an error matrix was developed. This matrix provided information of overall accuracy, producer accuracy and user accuracy for each class, and the kappa coefficient (Table 2).

The overall accuracy for the AVIRIS classification was 63.55%, whereas for the WV2 image was 64.81%. Mumby et al. (1998) reported an overall accuracy of for CASI sensor (81%) and Landsat TM (31%) for the thematic maps of reef habitats (nine classes). An overall accuracy of

coarse-level habitat maps was achieved by Mumby and Edwards (2002) in the Turks and Caicos for IKONOS (75%), Landsat TM (73%), and SPOT XS (67%). Mishra et al. (2007) reported an overall accuracy of 83.6% for a hyperspectral AISA image and 80.6% from IKONOS image in Roatan Islands, Honduras. The map classification produced an overall accuracy of 69% for seven classes for an IKONOS image for an area of approximately 10.5 Km^2 in the Arabian Gulf (Purkis 2005). Our reported overall accuracy coincides with the overall accuracy found by Purkis (2005), but was lower than the studies cited. The most comprehensive study that covered our study area was done by Bauer et al. (2012), but used photo interpretation for the classification with an overall accuracy of 95.4% for southwestern Puerto Rico, including La Parguera.

However, the cited areas that applied water column corrections were relatively smaller areas (Roatan Islands = 1.6 km^2, Mishra et al. 2007; South Caicos = 60 km^2 Mumby et al. 1998) or shallow clear waters (Mumby and Edwards 2002). Our study area was approximately 168 Km^2 with a depth range from 0-36 meters (average depth = ~18 meters). These physical factors limit the retrieval of bottom albedo signal from deeper areas that are required for the ISODATA segmentation process. The variations in the optical parameters in La Parguera Reserve were also relevant since the Kd and turbidity values can be higher that the compared areas due to the runoff and input of terrestrial, coastal, and bottom-derived materials (Otero and Carbery 2005). Also, the extent of the study are enhances these limitations by combining segments of similarly low signal from deeper areas, thus resulting in a reduced accuracy in the overall classification. Because of these limitations, other studies in La Parguera Reserve area that used similar objective-based approaches have only focused in shallow small offshore cays within the reserve, like Cayo Enrique and Cayo Laurel (Zayas-Santiago 2011, Torres-Madronero et al. 2009), San

Cristobal cay (Guild et al. 2008), and the inner shelf with relatively shallow waters (< 6 meters)(Arce Arce 2005).

4.3.2 Producer Accuracy

The producer accuracy for AVIRIS classification was higher for the class sand with benthic algae with 79.17%, followed by 75% for seagrass and hardbottom classes, with lowest class being the sand class with 48.08%. The producer accuracy for WV2 classification was higher for the hardbottom class with 75.0%, followed by 73.03% for coral reefs and 72.0% for seagrass class, with lowest class being the sand class with 40.35% (Table 2). The producer's accuracy is important for the technician carrying out the classification, because it indicates that for that percent of the time, that benthic type was classified as such. The major differences between producer's accuracy from the classified images were in the mix:sand/harbottom/coral class (diff. 10.16%) and the sand with benthic algae (diff. 8.80%). Major differences in total area covered for the two dominant classes (ie. coral reefs and sand) did not had an effect in the producer's accuracy for this class. Mishra et al. (2007) reported producer's accuracy higher than 80% for all major classes except for the mixed sand/hardbottom/coral class (63.67%) and the sand with benthic algae (65.00%). Arce Arce (2005) reported a maximum producer's accuracy for the classification of the depth invariant bands from the IKONOS image of 72.73% for seagrass, 15.15% coral , and 100% for sand.

4.3.3 User Accuracy

The user accuracy for AVIRIS classification was higher for the sand class with 89.29%, followed by 67.39% for coral reefs and 65.00% for mud class, with lowest class being the sand class with

benthic algae with 51.35%. The user accuracy for WV2 classification was higher for the sand class with 82.14%, followed by 71.43% for coral reefs and 75.00% for mud class, with lowest class being the sand class with benthic algae with 51.35%. The user's accuracy is relevant in a management context, because for example, each time an area labelled as a sand on the map is visited, there is a 89.29% probability that it is actually sand. The user's accuracies were very similar for the AVIRIS and WV2 classifications, with the major differences being only the mud class (diff. 10.00%). Also, major differences in total area covered for the two dominant classes (ie. coral reefs and sand) did not had an effect in the user's accuracies for these classes.

Mishra et al. (2007) reported producer's accuracy higher than 80% for all major classes except for the mixed sand/hardbottom/coral class (63.67%) and the sand with benthic algae (65.0%). Arce Arce (2005) reported a maximum producer's accuracy for the classification of the depth invariant bands from the IKONOS image of 72.73% for seagrass, for 15.15% coral , and 100% for sand. Mumby and Edwards (2002) found that IKONOS data allowed seagrass beds to be mapped very accurately (89%), coral and sand habitats to be mapped with good accuracy (79% and 72%, respectively), but that the user accuracy for macroalgal habitats was lower at 60%. Mishra et al. (2007) reported user's accuracy higher than 80% for all major classes except for the hardbottom (76.62%) and the coral reefs (73.59%). Arce Arce (2005) reported a maximum producer's accuracy for the classification of the depth invariant bands from the IKONOS image of 60.61% for seagrass, 16.67% for coral, and 100% for sand. The higher user accuracies obtained in the sand class were very important, because they are comparable with the results found by other researchers for shallower and smaller areas and indicate that the model can correctly discriminate sand at various depth ranges. Additionally, the shallow and deep coral

reefs return high user's accuracies (i.e., there is a high probability that an area predicted to be dominated by these classes in the imagery would also be so within the reference data) and also obtained a high producer's accuracy, indicating that pixels of this class are equally well identified in the imagery (Purkis 2005).

4.3.4 Kappa Coefficient

The kappa coefficient was calculated for the AVIRIS classification image (55%) and the WV2 classification image (57%). The kappa coefficient also provides a basis for determining the statistical significance of any given classification matrix. Kappa can be thought of as the chance corrected proportional agreement, and possible values range from +1 (perfect agreement) via 0 (no agreement above that expected by chance) to -1 (complete disagreement) (Nichols 2012). Landis and Koch (1977) developed guidelines for interpretation of the kappa coefficient as a statistic "strength of agreement" where; <0 = Poor; 0.01 – 0.20 = Slight; 0.21 – 0.40 = Fair; 0.41 – 0.60 = Moderate; 0.61 – 0.80 = Substantial; 0.81 – 1.00 = Almost Perfect. Our results fall within the moderate category results. Mishra et al. (2005) obtained an overall kappa statistic of 77.4% for the IKONOS imagery and for the AISA Eagle hyperspectral imagery an overall kappa statistic 80.8% (Mishra et al. 2007) for seven classes. Arce Arce (2005) reported a kappa coefficient of 66.67% for IKONOS in La Parguera Reserve for 6 classes. A kappa coefficient of 55.30% in the Enrique Reef and a kappa coefficient of 66.62% was found for the Laurel Reef (Zayas-Santiago 2011) for seven classes. These cited study areas presented the ideal characteristics to apply these classifications (ie. shallow water, uniform bottom) when compared to the physical limitations and extent of our study area. After taking into account these factors,

the kappa coefficient obtained provides a moderate classification over the chance-corrected proportional agreement.

4.3.5 Tau Coefficient

The Tau coefficient was calculated and represents a measure of the improvement of classification accuracy over a random assignment of map categories (Greene et al. 2000). According to Ma and Redmond (2000), the main advantage of Tau is that the coefficient is readily interpretable, indicating that the percentage of polygons were classified correctly than would be expected by chance alone. The tau coefficient was calculated for the AVIRIS classification image (59%) and the WV2 classification image (60%). Bejarano et al. (2010) summarized overall accuracies obtained by other studies on coral reef areas using the tau coefficient. Purkis (2005), calculated a Tau coefficient of 65% for seven classes for an IKONOS image. Mumby and Edwards 2002 evaluated the tau coefficients at different classification levels for various sensors and found that the tau coefficient is reduced in IKONOS (67% to 47%) and Landsat TM (61% to 24%) when classification was increased from 4 classes to 13 classes. Also, this reduction in tau coefficient was less evident in the CASI hyperspectral image (85%-78%) for a classification increase of four to nine classes. In our case, the tau coefficients were similar for both AVIRIS and IKONOS image indicating that both images attained comparative classification accuracy for the classes selected from the studies cited, even when the physical limitations of our study site further limits these accuracies.

4.4 Overall Image Classification Comparison

The AVIRIS and WV2 images performed very similar for the image classification and benthic classes selected (Figure 6). The images collected by these sensors were mainly the spectral resolution of available visible bands (AVIRIS = 32; WV2 = 5) and the dynamic range (AVIRIS = 16-bit; WV2 =11-bit). However, after applying the Lee's (1999) algorithm to retrieve bottom albedo, only AVIRIS provided the spectral bands needed for the water column correction. To our surprise, the WV2 performed similarly to the AVIRIS when the classification scheme was applied. As noted by Mumby and Edwards (2002) the hyperspectral sensor should have performed better in the classification for the same study area and spectral resolution, due to the discriminating ability of having 32 bands in the visible range. Another explanation in that these advantages were balanced by; errors arising from the different atmospheric corrections (Collin and Hench 2012), different water column conditions when images were acquired (i.e. high CDOM or chlorophyll concentrations), water column corrections, or that the sensors indeed have a similar capacity to resolve benthic habitats and the optical model used to correct for submergence effects, performs equally well in deep and shallow environments.

There were some disparities in the image acquisition dates and field surveys, and these effects may have accounted for some differences in the classification of the image. Even considering that the habitats surveyed do not move tens of meters in 5 years (Mumby and Edwards 2002), the timespan between the AVIRIS image and the field data was from 6 to 9 years, while the difference from the WV2 image was 1 to 3 years. Also, a massive bleaching event occurred during the AVIRIS image acquisition followed by a coral reef mass-mortality (Eakin et al. 2010) This event was particularly detrimental to *Montastraea (Orbicella) annularis* complex resulting

in mortalities in the order of 50% (Garcia-Sais et al. 2008). These factors may explain the difference in the total area covered of the coral reef class between the AVIRIS image (50.32 km^2) and the WV2 (22.89 Km^2). Additionally, this indicated that although there were differences in the total area for coral reefs class, sufficient ground validation points were collected for the classification due to the similarity and high accuracy of the user's and producer's accuracy between both images.

The average depth for each of the classes was obtained (Table 1) but no major differences were found in average depth class, except for the sand class (diff. 2.37 meters). This difference, although small, indicated that deeper sand areas were identified in the WV2 classification when compared to the AVIRIS classification. Also, this could account for the increase of 8% in the sand class found in the WV2 classification.

Additional limitations of both sensors in separating clusters in very shallow areas, could be explained by estimation of the down-welling attenuation coefficient (Kd) used in the water column corrections (Purkis 2005). These estimates may be susceptible to error in optically shallow water where seafloor reflection, the propagation of diffuse incoming radiation may not follow a negative exponential with respect to depth (Maritorena et al. 1994). Also, Purkis (2005) found using IKONOS that a RMS error in bathymetry of 1.4 meters for a sandy bottom under 2 meters of water could be translated to an absolute error in retrieved albedo of 10% and 26% in bands 1 and 2, respectively.

The additive factor of such errors do not limit the production of a benthic habitat, but would drastically reduce the separability of the eight classes, and therefore map accuracy, unless errors are minimized or a reduction in the number of benthic classes was applied (Purkis 2005).

4.5 Object Based Classification vs. Photo-Interpretation

According to Green et al (2000), photo-interpretation is a method by which the user visually inspects an image and identifies habitats and object based classification is a computer-based method by which a number of wavebands are input to a statistical clustering algorithm, which organizes individual pixels into distinctive groups (classes) which are assumed to represent specific habitat types. Our data was processed using the object based approach were the bottom albedo image was classified from the AVIRIS and WV2 images after an atmospheric and water column correction.

The most comparable study that covered our study area was done by Bauer et al. (2012) and used photo interpretation for the classification with an overall accuracy of 95.4% for the southwest Puerto Rico area, including La Parguera. This study was also an improvement over the original benthic habitat map for La Parguera Reserve area by Kendall (2001) in terms of classification scheme, mapping accuracy, and extent covered. This overall accuracy was significantly higher that our results, however some limitations arise from using these methods. These methods are very subjective, time consuming and required highly skilled personnel. Additionally, there are difficulties comparing classified products at different dates (i.e. change detection) due to the subjectivity of the interpretation (Green et al. 2000). Our methods utilized the full spectral range of the imagery while providing comparable results that could be extrapolated to other study areas (Purkis 2005; Lesser and Mobley 2007), and provided a superior spatial resolution (4 m^2) to this study (1,000 m^2). The total area for coral reefs in La Parguera Reserve identified by this study was 44.07 km^2 (662 polygons) including aggregated reefs, aggregated patch reefs, patch reefs and spur and groove. The total area for AVIRIS was 50.32 km^2 and WV2 was 22.89 km^2 with over 10,000 polygons identified. These differences in the amount of polygons identify the

generalization produced by the photo interpretation and the limitation of a large mapping unit. The total overlapped areas between the study by Bauer et al. (2012) and AVIRIS was 19.10 km^2 (38%), and for WV2 was 12.40 km^2 (54%). This indicated a better correlation of the classification for coral reefs of the WV2 imagery with the photo interpretation study, even when the latter nearly doubled the amount of area reported. Also, as discussed earlier, the temporal difference between images may contribute to the difference in the coral reef class totals and may indicate that the spatial resolution was an important factor in identifying coral reefs, especially patch reefs areas when compared with this study.

5. Conclusions

The benthic habitat maps were developed successfully from the bottom albedo images of both AVIRIS and WV2 sensors. No major class differences were found between the AVIRIS and WV2 classification totals, except for coral reefs and sand classes' totals. The reduction in the coral reefs class total could be attributed to temporal differences of the images depicting the changes in the coral reefs distribution within the reserve. The overall accuracies were very similar for both images, but were lower when compared with other studies using similar object based methods. However, the cited areas were relatively smaller areas, with shallow clear waters, and optically simpler than our study area, so our results could be evaluated as acceptable based on these physical factors. An extensive comparison was done with the study of the reserve that used photo interpretation for the classification (Bauer et al. 2012) and important limitations were evaluated. These methods are very subjective, time consuming and required highly skilled personnel. Additionally, there are difficulties comparing classified products at different dates (i.e. change detection) due to the subjectivity of the interpretation (Green et al. 2000). Our methods utilized the full spectral range of the imagery while providing comparable results that could be extrapolated to other study areas (Purkis 2005; Lesser and Mobley 2007), and provided a superior spatial resolution (4 m^2) to this study (1,000 m^2). The total area for coral reefs in La Parguera Reserve identified by this study was 44.07 km^2 (662 polygons) including aggregated reefs, aggregated patch reefs, patch reefs and spur and groove. The total area for AVIRIS was 50.32 km^2 and WV2 was 22.89 km^2 with over 10,000 polygons identified. These differences in the amount of polygons identify the generalization produced by the photo interpretation and the limitation of a large mapping unit. The total overlapped areas between the study by Bauer et al. (2012) and AVIRIS was 19.10 km^2 (38%), and for WV2 was 12.40 km^2 (54%).

Previous studies in La Parguera Reserve area that used similar objective-based approaches have only focused in shallow small offshore cays within the reserve, like Cayo Enrique and Cayo Laurel (Zayas-Santiago 2011, Torres-Madronero et al. 2009), San Cristobal cay (Guild et al. 2008), and the inner shelf with relatively shallow waters (< 6 meters)(Arce Arce 2005). A major contribution of this study was that no previous benthic habitat map was available for La Parguera Reserve that provided: multi/hyper spectral information at this spatial scale (4 square meters), covered the extent of the reserve, and provided the baseline for future development of benthic habitat studies using an objective classification scheme.

This top-down approach, where the environmental data and *in situ* biological/geological data are organized before they are combined (unsupervised classification)(Brown et a., 2011) and later merging with data based on distance, provides a new approach into classifying information, while maintaining the objectivity in the classification. This analysis has also demonstrated the efficacy of using satellite and airborne imagery for benthic habitat mapping in identifying the baseline trends and anomalies, stratify ecosystems to focus on areas of particular concern for conservation of coral reef ecosystems (Rohman and Shapiro 2006). These techniques are a very effective tool for monitoring the spatial dynamics of habitats in Marine Protected Areas (Mumby and Edwards 2002). According to Green et al. (2000), the photo-interpretation and object based classification should be thought of as complementing each other, and a good classification can be achieved using a combination of approaches. Further improvements to this project could be attained by resolving data gaps or fine-tuned the classifier with additional ancillary information from photo-interpretation or contextual editing.

6. References

Arce-Arce, Jeannette. 2005. “Remote Sensing of Benthic Habitats in Southwestern Puerto Rico". Master Thesis-Unpublished Data. Department of Geology. University of Puerto Rico Mayaguez.

Bauer, Laurie J, Kimberly Edwards, Matthew S Kendall, Kimberly K W Roberson, Sam Tormey, and Timothy A Battista. 2012. “Shallow-Water Benthic Habitats of Southwest Puerto Rico.”

Bejarano, Sonia, Peter J. Mumby, John D. Hedley, and Ian Sotheran. 2010. “Combining Optical and Acoustic Data to Enhance the Detection of Caribbean Forereef Habitats.” Remote Sensing of Environment 114 (11). Elsevier Inc.: 2768–78. doi:10.1016/j.rse.2010.06.012.

Brown, Craig J., Stephen J. Smith, Peter Lawton, and John T. Anderson. 2011. “Benthic Habitat Mapping: A Review of Progress towards Improved Understanding of the Spatial Ecology of the Seafloor Using Acoustic Techniques.” Estuarine, Coastal and Shelf Science 92 (3). Elsevier Ltd: 502–20. doi:10.1016/j.ecss.2011.02.007.

Cardona-Maldonado, María a. 2008. “Assessment of Coral Reef Community Structure Using Water Optical Properties.” Unpublished Data Master Thesis. University of Puerto Rico Mayaguez.

Cedeira-Estrada S, Heege T, Kolb M, Ohlendorf S, Uribe A, Muller A, Garza R, Ressl R, Aguirre R, Marino I, Silva R, Martell R (2012) Benthic habitat and bathymetry mapping of shallow waters in Puerto Morelos reefs using remote sensing with a physics based data processing. In: 2012 I.E. International Geoscience and Remote Sensing Symposium (IGARSS), Munich, pp 4383–4386.

Eakin, Mark Morgan, Jessica A. Heron, Scott F. Smith, Tyler B. Liu, Gang Alvarez-Filip, Bart Baca, Lorenzo Bartels, Erich Bastidas, Carolina Bouchon, Claude Brandt, Marilyn Andrew W. Bruckner,Lucy Bunkley-Williams,Yusri Yusuf. 2005 Caribbean Corals in Crisis: Record Thermal Stress, Bleaching, and Mortality in 2005.

Exelis Visual Information Solutions. 2011. “Case Study : NOAA Maps and Extracts Detailed Information about Sea Floor Habitats Using ENVI Image Analysis Software.”

García-Sais JR, Appeldoorn R, Batista T, Bauer L, Bruckner A, Caldow C, Carrubba, Corredor J, Díaz E Lilyestrom C, García-Moliner G, Hernández-Delgado E, Menza E, Morell J, Pait A, Sabater-Clavell J, Weil E, Williams E, (2008). The State of Coral Reef Ecosystems of the Commonwealth of Puerto Rico. pp. 75-116. In Waddell J, Clarke AM (eds.). The State of Coral Reef Ecosystems of the United States and Pacific Freely Associated States. NOAA Technical Memorandum NOS NCCOS 73. NOAA/NOS/NCCOS. Center for Coastal
http://www.jstor.org/discover/10.2307/2529310?uid=820536&uid=3738864&uid=811000&uid=2&uid=3&uid=67&uid=62&sid=21106103631631

Jensen, J R. 2006. Remote Sensing of the Environment: An Earth Resource Perspective. Prentice Hall, Upper Saddle River, NJ. 2nd edition. Prentice Hall.

Jensen, J. R. 1996. Introductory Digital Image Processing: A Remote Sensing Perspective. Second Edition. Introductory Digital Image Processing: A Remote Sensing Perspective. Second Edition.

Kendall, M.S., M.E. Monaco, K.R. Buja, J.D. Christensen, C.R. Kruer, M. Finkbeiner, and R.A. Warner. 2001. "Methods Used to Map the Benthic Habitats of Puerto Rico and the U.S. Virgin Islands," http://biogeo.nos.noaa.gov/projects/mapping/caribb.

Landis JR, Koch GG. 1977. The measurement of observer agreement for categorical data. Biometrics. 1977 Mar;33 (1):159-74.

Lang, R., 2007. Optimizing unsupervised classifications of remotely sensed imagery with a data-assisted labeling approach, Computers and Geosciences, 34, 1877-1885.

Lee, Z, K L Carder, C D Mobley, R G Steward, and J S Patch. 1999. "Hyperspectral Remote Sensing for Shallow Waters. 2. Deriving Bottom Depths and Water Properties by Optimization." Applied Optics 38 (18): 3831–43. doi:10.1364/AO.38.003831.

Lee, Zhongping, Brandon Casey, Robert Arnone, Alan Weidemann, Rost Parsons, Marcos J. Montes, Bo-Cai Gao, Wesley Goode, Curtiss Davis, and Julie Dye. 2007. "Water and Bottom Properties of a Coastal Environment Derived from Hyperion Data Measured from the EO-1 Spacecraft Platform." Journal of Applied Remote Sensing 1 (December): 011502. doi:10.1117/1.2822610.

Lesser, M. P., and C. D. Mobley. 2007. "Bathymetry, Water Optical Properties, and Benthic Classification of Coral Reefs Using Hyperspectral Remote Sensing Imagery." Coral Reefs 26: 819–29. doi:10.1007/s00338-007-0271-5.

Lillesand, T., Kiefer, R., and Chipman, J., 2004. Remote Sensing and Image Interpretation, 5th Edition: Wiley, New York, NY. 763pp.

Lobitz, B, L Guild, and R Armstrong. 2008. "Pre-Processing 2005 AVIRIS Data for Coral Reef Analysis." … International Coral Reef …, no. 17: 7–11. http://www.nova.edu/ncri/11icrs/proceedings/files/m17-10.pdf.

Lyzenga, David R. 1981. "Remote Sensing of Bottom Reflectance and Water Attenuation Parameters in Shallow Water Using Aircraft and Landsat Data." International Journal of Remote Sensing. doi:10.1080/01431168108948342.

Mapping European Seabed Habitats, MESH. 2008. MESH Guide to Habitat Mapping. Peterborough, UK. http://www.emodnet-seabedhabitats.eu/pdf/MESH Guide Synopsis (web).pdf.

Matthew, M. W., S. M. Adler-Golden, A. Berk, G. Felde, G. P. Anderson, D. Gorodestzky, S. Paswaters, and M. Shippert (2003), Atmospheric correction of spectral imagery: Evaluation of the FLAASH algorithm with AVIRIS data, Proc. SPIE, IX(5093), 474– 482.

Mishra, D. R., S. Narumalani, D. Rundquist, and M. Lawson (2005), High-Resolution Ocean Color Remote Sensing Of Benthic Habitats: A Case Study at The Roatan Island, Honduras, IEEE Trans. Geosci. Remote Sens., 43(7), 1592– 1604.

Mishra, Deepak R., Sunil Narumalani, Donald Rundquist, Merlin Lawson, and R. Perk. 2007. "Enhancing the Detection and Classification of Coral Reef and Associated Benthic Habitats: A Hyperspectral Remote Sensing Approach." Journal of Geophysical Research 112. doi:10.1029/2006JC003892.

Mumby, P J, and A R Harborne. 1999. "Development of a Systematic Classification Scheme of Marine Habitats to Facilitate Regional Managment and Mapping of Caribbean Coral Reefs." Biololgical Conservation 88: 155–63.

Mumby, P.J., C.D. Clark, E.P. Green, A.J. Edwards. 1998. The practical benefits of water column correction and contextual editing for mapping coral reefs. International Journal of Remote Sensing, 19 (1998), pp. 203–210

Mumby, P.J., E.P. Green, C.D. Clark, A.J. Edwards. 1998. Digital analysis of multispectral airborne imagery of coral reefs. Coral Reefs, 17 (1998), pp. 59–69.

Nichols, Charles T. 2012. Land Use / Land Cover Classification: Methods to Overcome Pixel Confusion and the Effects of Tree Shadows in Very High Resolution Multispectral Imagery. Master Thesis (Unpublished Data). Department of Humanities and Social Sciences. Northwest Missouri State University

Otero, Ernesto, and Kelly K. Carbery. 2005. "Chlorophyll a and Turbidity Patterns over Coral Reefs Systems of La Parguera Natural Reserve, Puerto Rico." Revista de Biologia Tropical 53 (May): 25–32.

Prada, M. C., R. S. Appeldoorn, and J. a. Rivera. 2008. "The Effects of Minimum Map Unit in Coral Reefs Maps Generated from High Resolution Side Scan Sonar Mosaics." Coral Reefs 27: 297–310. doi:10.1007/s00338-007-0328-5.

Purkis, Samuel and Klemas, Victor. 2011. Remote Sensing and Global Environmental Change. First Edition. Wiley-Blackwell.

Roelfsema C.M., Phinn, S.R., Dennison, W.C. 2002. Spatial distribution of benthic microalgae on coral reefs determined by remote sensing. Coral Reefs (2002) 21: 264–274 DOI 10.1007/s00338-002-0242-9.

Sugumaran, R., Pavuluri M., and Zerr, D., 2003. The use of high-resolution imagery for identification of urban climax forest species using traditional and rule-based classification approach. IEEE Transactions on Geoscience and Remote Sensing. 41(9), 1933-1939.

Torres-Madronero, Maria C., Miguel Velez-Reyes, and James a. Goodman. 2009. "Fusion of Hyperspectral Imagery and Bathymetry Information for Inversion of Bioptical Models." Proceedings of SPIE 7473: 74730I – 74730I – 11. doi:10.1117/12.835896.

United Nations Environment (UNEP). 2006. "Marine and Coastal Ecosystems and Human Well-Being: A Synthesis Report Based on the Findings of the Millennium Ecosystem Assessment." Russell The Journal Of The Bertrand Russell Archives, 76. http://www.vliz.be/imisdocs/publications/120064.pdf.

Zayas-Santiago, Carmen C. 2011. "Landscape Structure in Two Reefs in La Parguera and the Distribution of the Lytechinus Variegatus". Master Thesis-Unpublished Data". Department of Marine Sciences. University fo Puerto Rico Mayaguez.

Appendix A: Benthic Classification Classes and Description

Seven classes were mapped that refers to the predominant physical composition of features that could be resolve using bottom albedo derived at different depths.

Class 1: Coral Reefs

A high relief coral formation of variable shapes in both shallow and deep-water that typically lack a thick sediment covering the seafloor. May include patch reefs and spur and groove coral, if spatial resolution is not sufficient to separate other bottom types. Includes both solid and soft corals. No percentage of cover was calculated.


Class 2: Seagrass

Primarily sand or mud bottom dominated by any single species of seagrass (e.g., *Syringodium sp*., *Thalassia sp*. and *Halophila sp*.) or a combination of several species. Substrate may be sand, mud or hardbottom cover. No percentage of cover was calculated.

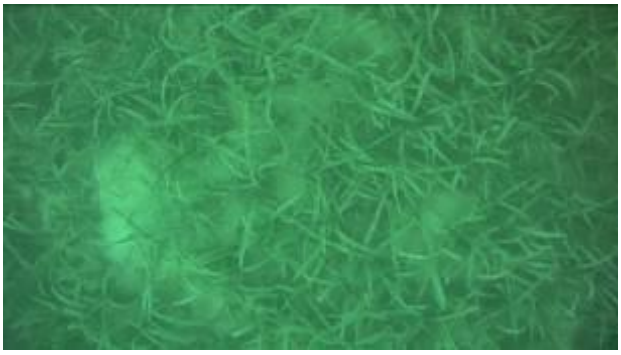


Class 3: Hardbottom

Consolidated materials that consist of solid structure (mainly carbonate) that may contain coral rubble or a thin veneer of sand. This class includes hardbottom with no additional coverage biological cover (algae, seagrass).

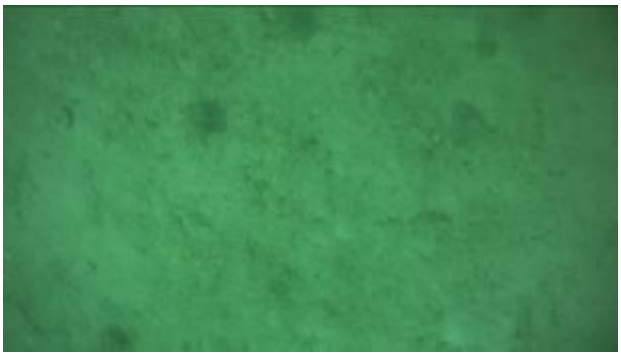

Class 4: Mix: Sand/Hardbottom/Coral

A mixture of unconsolidated sediments (mainly sand) in combination with solid structures or coral that cannot be separated by due to spatial resolution by image classification or field validation methods. No percentage of cover was calculated.

Class 5: Mud

Fine unconsolidated sediment associated with river discharge, land discharge and build-up of organic material in sheltered areas. This class includes mud with no additional coverage.

Class 6: Sand

Coarse unconsolidated sediment typically found in areas exposed to currents or wave energy. This class includes sand with no additional coverage.

Class 7: Sand with Benthic Algae

Primarily sand bottom with distribution of any combination of species of red, green or brown algae that can be turf, fleshy, coralline or filamentous species. No percentage of cover was calculated.

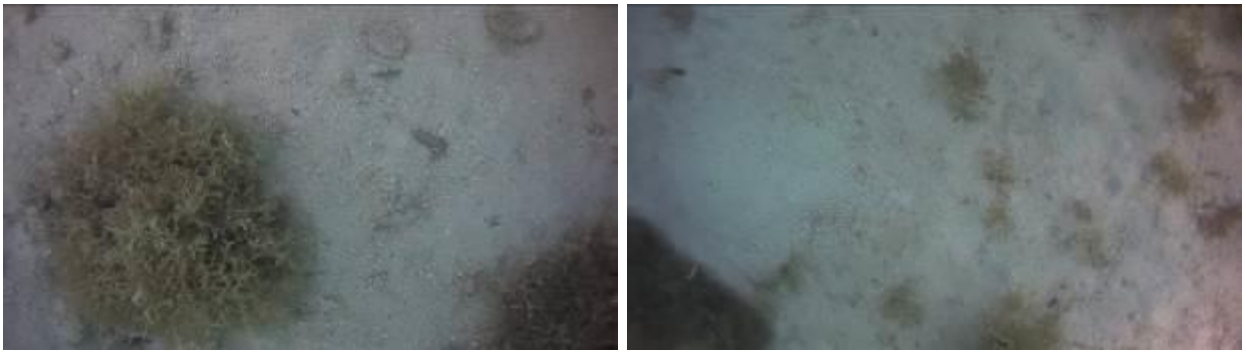

Appendix B: Ground Validation and Accuracy Assessment Points

Ground Validation Points			
ID	Longitude	Latitude	Class Description
1	-67.01	17.94	Sand
2	-67.04	17.95	Coral Reefs
3	-67.08	17.94	Coral Reefs
4	-67.08	17.94	Sand
5	-67.08	17.94	Sand with Benthic Algae
6	-67.08	17.94	Sand with Benthic Algae
7	-67.08	17.94	Mix:Sand/Hardbottom/Coral
8	-67.08	17.94	Coral Reefs
9	-67.08	17.94	Coral Reefs
10	-67.08	17.94	Coral Reefs
11	-67.08	17.94	Coral Reefs
12	-67.08	17.94	Coral Reefs
13	-67.08	17.95	Mud
14	-67.07	17.96	Dense Seagrass
15	-67.05	17.96	Mud
16	-67.01	17.93	Mix:Sand/Hardbottom/Coral
17	-67.01	17.93	Mud
18	-67.03	17.93	Sand
19	-67.03	17.94	Mud
20	-67.05	17.94	Coral Reefs
21	-67.05	17.94	Hardbottom
22	-67.05	17.94	Hardbottom
23	-67.07	17.94	Mix:Sand/Hardbottom/Coral
24	-67.07	17.94	Coral Reefs
25	-67.07	17.94	Mix:Sand/Hardbottom/Coral
26	-67.08	17.94	Mix:Sand/Hardbottom/Coral
27	-67.10	17.94	Seagrass with Sand
28	-67.07	17.95	Mud
29	-67.00	17.93	Sand
30	-67.06	17.91	Sand
31	-67.07	17.91	Sand with Benthic Algae
32	-67.07	17.91	Sand
33	-67.09	17.92	Mix:Sand/Hardbottom/Coral
34	-67.10	17.92	Coral Reefs
35	-67.10	17.93	Sand with Benthic Algae
36	-67.11	17.93	Coral Reefs with Sand
37	-67.11	17.93	Coral Reefs with Sand
38	-67.13	17.92	Dense Seagrass
39	-67.13	17.92	Mix:Sand/Hardbottom/Coral
40	-67.06	17.92	Coral Reefs
41	-67.02	17.91	Coral Reefs
42	-66.99	17.95	Coral Reefs
43	-67.07	17.93	Coral Reefs
44	-67.03	17.92	Coral Reefs
45	-67.08	17.94	Coral Reefs
46	-67.07	17.93	Coral Reefs
47	-67.03	17.95	Coral Reefs
48	-67.00	17.92	Coral Reefs
49	-66.99	17.93	Coral Reefs
50	-67.13	17.94	Coral Reefs
51	-67.12	17.94	Coral Reefs
52	-66.99	17.92	Coral Reefs
53	-67.06	17.93	Coral Reefs
54	-67.05	17.93	Coral Reefs
55	-67.13	17.92	Coral Reefs
56	-67.04	17.93	Seagrass with Sand
57	-67.09	17.93	Sand with Benthic Algae
58	-67.13	17.88	Mix:Sand/Hardbottom/Coral
59	-67.03	17.90	Coral Reefs
60	-67.05	17.87	Hardbottom
61	-67.05	17.88	Mix:Sand/Hardbottom/Coral
62	-67.05	17.90	Mix:Sand/Hardbottom/Coral
63	-67.06	17.93	Sand
64	-67.06	17.93	Coral Reefs
65	-66.99	17.93	Sand
66	-67.00	17.91	Sand
67	-66.99	17.94	Sand
68	-67.02	17.96	Mud
69	-67.08	17.90	Coral Reefs
70	-67.06	17.90	Coral Reefs
71	-67.06	17.89	Coral Reefs with Sand
72	-67.08	17.87	Mix:Sand/Hardbottom/Coral
73	-67.10	17.87	Coral Reefs
74	-67.10	17.90	Hardbottom

75	-67.11	17.89	Sand with Benthic Algae
76	-67.11	17.88	Coral Reefs
77	-67.11	17.86	Coral Reefs
78	-67.13	17.87	Coral Reefs with Sand
79	-67.13	17.87	Coral Reefs
80	-67.12	17.93	Coral Reefs
81	-67.11	17.93	Coral Reefs
82	-67.13	17.90	Sand with Benthic Algae
83	-67.00	17.95	Mud
84	-67.01	17.91	Coral Reefs with Sand
85	-66.98	17.93	Coral Reefs with Sand
86	-67.02	17.91	Coral Reefs with Sand
87	-67.02	17.90	Coral Reefs
88	-66.99	17.90	Sand with Benthic Algae
89	-67.02	17.89	Coral Reefs with Sand
90	-67.00	17.90	Coral Reefs
91	-67.00	17.89	Coral Reefs with Sand
92	-67.01	17.96	Coral Reefs with Sand
93	-67.06	17.88	Hardbottom
94	-67.08	17.87	Hardbottom
95	-67.09	17.89	Coral Reefs with Sand
96	-67.11	17.86	Hardbottom
97	-67.08	17.96	Dense Seagrass
98	-67.06	17.96	Dense Seagrass
99	-67.07	17.96	Sand with Benthic Algae
100	-67.06	17.96	Seagrass with Sand
101	-67.06	17.97	Seagrass with Sand
102	-67.06	17.97	Seagrass with Sand
103	-67.05	17.96	Mud
104	-67.03	17.97	Dense Seagrass
105	-66.99	17.95	Mud
106	-67.00	17.95	Seagrass with Sand
107	-67.01	17.95	Seagrass with Sand
108	-67.01	17.95	Sand
109	-67.01	17.95	Sand
110	-67.02	17.95	Sand
111	-67.02	17.95	Mix:Sand/Hardbottom/Coral
112	-67.06	17.94	Sand
113	-67.06	17.94	Seagrass with Sand
114	-67.06	17.94	Seagrass with Sand
115	-67.09	17.94	Mix:Sand/Hardbottom/Coral
116	-67.09	17.94	Seagrass with Sand
117	-67.09	17.95	Sand with Benthic Algae
118	-67.10	17.94	Seagrass with Sand
119	-67.10	17.95	Dense Seagrass
120	-67.09	17.95	Dense Seagrass
121	-67.06	17.96	Coral Reefs
122	-67.06	17.96	Mix:Sand/Hardbottom/Coral
123	-67.00	17.96	Dense Seagrass
124	-67.12	17.94	Dense Seagrass
125	-67.13	17.95	Seagrass with Sand
126	-67.08	17.96	Dense Seagrass
127	-67.05	17.96	Sand
128	-67.05	17.96	Sand with Benthic Algae
129	-67.05	17.96	Sand with Benthic Algae
130	-67.04	17.96	Seagrass with Sand
131	-67.09	17.94	Sand
132	-67.05	17.91	Sand with Benthic Algae
133	-66.98	17.90	Hardbottom
134	-67.05	17.87	Hardbottom
135	-66.99	17.90	Hardbottom
136	-66.97	17.91	Hardbottom
137	-67.12	17.92	Hardbottom
138	-67.04	17.94	Seagrass with Sand
139	-67.05	17.94	Sand with Benthic Algae
140	-67.05	17.94	Mix:Sand/Hardbottom/Coral
141	-67.04	17.94	Mix:Sand/Hardbottom/Coral
142	-67.06	17.95	Mix:Sand/Hardbottom/Coral
143	-67.06	17.94	Mix:Sand/Hardbottom/Coral
144	-67.06	17.94	Sand
145	-67.10	17.94	Dense Seagrass
146	-67.05	17.96	Seagrass with Sand
147	-67.00	17.93	Sand with Benthic Algae
148	-67.03	17.92	Mix:Sand/Hardbottom/Coral
149	-67.04	17.92	Mix:Sand/Hardbottom/Coral
150	-67.04	17.91	Mix:Sand/Hardbottom/Coral
151	-67.09	17.91	Coral Reefs
152	-67.09	17.92	Coral Reefs
153	-67.03	17.96	Mix:Sand/Hardbottom/Coral
154	-67.06	17.91	Mix:Sand/Hardbottom/Coral

155	-67.03	17.89	Mix:Sand/Hardbottom/Coral
156	-67.06	17.90	Mix:Sand/Hardbottom/Coral
157	-67.08	17.90	Sand with Benthic Algae
158	-66.97	17.90	Mix:Sand/Hardbottom/Coral
159	-67.03	17.88	Mix:Sand/Hardbottom/Coral
160	-67.05	17.90	Mix:Sand/Hardbottom/Coral
161	-67.03	17.96	Mix:Sand/Hardbottom/Coral
162	-67.00	17.94	Mix:Sand/Hardbottom/Coral
163	-67.09	17.87	Mix:Sand/Hardbottom/Coral
164	-67.11	17.94	Mix:Sand/Hardbottom/Coral
165	-67.00	17.95	Seagrass with Sand
166	-67.05	17.94	Mix:Sand/Hardbottom/Coral
167	-67.05	17.94	Sand
168	-66.99	17.96	Mud
169	-67.00	17.95	Mud
170	-67.00	17.95	Seagrass with Sand
171	-66.99	17.95	Seagrass with Sand
172	-67.06	17.94	Mix:Sand/Hardbottom/Coral
173	-66.97	17.94	Sand
174	-66.98	17.95	Dense Seagrass
175	-67.07	17.95	Sand with Benthic Algae
176	-67.07	17.96	Mix:Sand/Hardbottom/Coral
177	-67.03	17.96	Coral Reefs
178	-67.04	17.94	Coral Reefs
179	-67.04	17.94	Sand
180	-67.04	17.94	Sand
181	-67.04	17.94	Coral Reefs
182	-67.04	17.94	Coral Reefs with Sand
183	-67.05	17.94	Mix:Sand/Hardbottom/Coral
184	-67.05	17.94	Coral Reefs with Sand
185	-67.05	17.94	Hardbottom
186	-67.05	17.94	Coral Reefs
187	-67.05	17.94	Mix:Sand/Hardbottom/Coral
188	-67.04	17.94	Sand
189	-67.06	17.94	Sand
190	-67.06	17.94	Seagrass with Sand
191	-67.06	17.94	Sand with Benthic Algae
192	-67.06	17.94	Sand with Benthic Algae
193	-67.11	17.87	Mix:Sand/Hardbottom/Coral
194	-67.04	17.97	Sand with Benthic Algae
195	-67.09	17.87	Hardbottom
196	-67.11	17.87	Sand with Benthic Algae
197	-67.05	17.96	Seagrass with Sand
198	-67.05	17.95	Seagrass with Sand
199	-67.05	17.96	Sand with Benthic Algae
200	-67.05	17.96	Seagrass with Sand
201	-67.04	17.96	Sand
202	-67.04	17.96	Coral Reefs
203	-67.04	17.96	Coral Reefs with Sand
204	-67.04	17.95	Coral Reefs
205	-67.05	17.95	Coral Reefs
206	-67.05	17.95	Coral Reefs
207	-67.05	17.95	Coral Reefs with Sand
208	-67.06	17.95	Coral Reefs
209	-67.05	17.95	Coral Reefs
210	-67.06	17.95	Mix:Sand/Hardbottom/Coral
211	-67.06	17.95	Mix:Sand/Hardbottom/Coral
212	-67.06	17.95	Coral Reefs with Sand
213	-67.07	17.96	Seagrass with Sand
214	-67.06	17.97	Dense Seagrass
215	-67.04	17.96	Sand
216	-66.98	17.95	Mix:Sand/Hardbottom/Coral
217	-67.02	17.93	Mix:Sand/Hardbottom/Coral
218	-66.99	17.92	Sand with Benthic Algae
219	-67.02	17.92	Coral Reefs
220	-67.11	17.92	Sand
221	-67.12	17.92	Sand
222	-67.02	17.97	Seagrass with Sand
223	-66.99	17.96	Seagrass with Sand
224	-67.10	17.92	Dense Seagrass
225	-66.99	17.96	Seagrass with Sand

Accuracy Assessment Points			
ID	Longitude	Latitude	Class Description
1	-67.01	17.89	Coral Reefs
2	-67.01	17.89	Hardbottom
3	-67.00	17.89	Hardbottom
4	-67.00	17.89	Mix:Sand/Hardbottom/Coral
5	-66.98	17.92	Coral Reefs
6	-67.06	17.93	Coral Reefs

7	-67.08	17.93	Coral Reefs	47	-67.04	17.95	Mud
8	-67.03	17.92	Mix:Sand/Hardbottom/Coral	48	-67.06	17.95	Mud
9	-67.02	17.91	Coral Reefs	49	-67.06	17.94	Sand
10	-66.99	17.92	Coral Reefs	50	-67.06	17.95	Mud
11	-67.08	17.93	Mix:Sand/Hardbottom/Coral	51	-67.05	17.94	Mud
12	-66.99	17.92	Coral Reefs	52	-66.99	17.92	Seagrass
13	-67.05	17.93	Coral Reefs	53	-67.01	17.90	Coral Reefs
14	-67.13	17.93	Coral Reefs	54	-67.06	17.94	Sand
15	-67.04	17.94	Coral Reefs	55	-66.98	17.91	Sand
16	-67.11	17.94	Coral Reefs	56	-67.00	17.94	Sand
17	-67.07	17.93	Coral Reefs	57	-67.01	17.91	Mix:Sand/Hardbottom/Coral
18	-66.99	17.94	Coral Reefs	58	-66.97	17.92	Sand
19	-67.07	17.93	Coral Reefs	59	-66.98	17.92	Sand
20	-67.10	17.92	Coral Reefs	60	-67.04	17.90	Mix:Sand/Hardbottom/Coral
21	-67.05	17.91	Mix:Sand/Hardbottom/Coral	61	-66.97	17.90	Mix:Sand/Hardbottom/Coral
22	-67.05	17.91	Hardbottom	62	-67.02	17.89	Sand with Benthic Algae
23	-67.04	17.91	Coral Reefs	63	-67.06	17.91	Sand with Benthic Algae
24	-67.04	17.89	Coral Reefs	64	-67.05	17.96	Sand
25	-67.05	17.91	Sand with Benthic Algae	65	-67.05	17.95	Seagrass
26	-67.05	17.91	Sand with Benthic Algae	66	-67.04	17.95	Mud
27	-67.06	17.91	Mix:Sand/Hardbottom/Coral	67	-67.06	17.92	Sand with Benthic Algae
28	-67.06	17.92	Coral Reefs	68	-67.04	17.92	Sand with Benthic Algae
29	-67.06	17.92	Coral Reefs	69	-67.07	17.94	Sand
30	-67.08	17.93	Coral Reefs	70	-67.06	17.95	Sand
31	-67.00	17.89	Coral Reefs	71	-67.03	17.96	Sand
32	-67.12	17.92	Coral Reefs	72	-67.00	17.90	Mix:Sand/Hardbottom/Coral
33	-67.09	17.92	Mix:Sand/Hardbottom/Coral	73	-66.99	17.92	Seagrass
34	-67.09	17.93	Coral Reefs	74	-66.98	17.91	Sand with Benthic Algae
35	-67.12	17.93	Mix:Sand/Hardbottom/Coral	75	-67.01	17.95	Mud
36	-67.13	17.93	Seagrass	76	-67.03	17.95	Mud
37	-67.06	17.92	Coral Reefs	77	-67.06	17.92	Sand
38	-67.06	17.95	Sand	78	-67.07	17.91	Sand
39	-67.06	17.94	Sand	79	-67.07	17.91	Sand
40	-67.03	17.93	Coral Reefs	80	-67.11	17.91	Sand
41	-66.99	17.93	Sand	81	-67.09	17.93	Mix:Sand/Hardbottom/Coral
42	-66.99	17.93	Sand	82	-66.97	17.92	Mix:Sand/Hardbottom/Coral
43	-67.06	17.92	Coral Reefs	83	-67.06	17.90	Mix:Sand/Hardbottom/Coral
44	-67.07	17.93	Coral Reefs	84	-67.07	17.92	Mix:Sand/Hardbottom/Coral
45	-67.03	17.95	Sand	85	-67.03	17.92	Mix:Sand/Hardbottom/Coral
46	-67.04	17.96	Sand	86	-67.03	17.92	Mix:Sand/Hardbottom/Coral

87	-67.07	17.90	Mix:Sand/Hardbottom/Coral	128	-67.09	17.94	Hardbottom
88	-67.01	17.91	Mix:Sand/Hardbottom/Coral	129	-67.08	17.96	Seagrass
89	-67.05	17.90	Mix:Sand/Hardbottom/Coral	130	-67.06	17.96	Seagrass
90	-67.03	17.92	Mix:Sand/Hardbottom/Coral	131	-67.08	17.95	Coral Reefs
91	-67.03	17.92	Mix:Sand/Hardbottom/Coral	132	-67.06	17.96	Seagrass
92	-67.03	17.89	Mix:Sand/Hardbottom/Coral	133	-67.06	17.96	Mix:Sand/Hardbottom/Coral
93	-67.03	17.89	Mix:Sand/Hardbottom/Coral	134	-67.10	17.94	Mix:Sand/Hardbottom/Coral
94	-67.06	17.90	Sand with Benthic Algae	135	-67.10	17.94	Mix:Sand/Hardbottom/Coral
95	-67.09	17.91	Mix:Sand/Hardbottom/Coral	136	-67.07	17.96	Seagrass
96	-67.09	17.93	Coral Reefs	137	-67.07	17.96	Seagrass
97	-67.05	17.92	Sand	138	-67.12	17.95	Seagrass
98	-67.07	17.95	Sand with Benthic Algae	139	-67.06	17.96	Mix:Sand/Hardbottom/Coral
99	-67.07	17.95	Mud	140	-67.00	17.97	Mud
100	-67.06	17.96	Mud	141	-67.08	17.87	Sand with Benthic Algae
101	-67.06	17.96	Mud	142	-67.05	17.88	Hardbottom
102	-67.06	17.96	Mud	143	-67.00	17.90	Hardbottom
103	-67.00	17.95	Mud	144	-66.98	17.90	Hardbottom
104	-67.01	17.96	Mud	145	-66.98	17.89	Coral Reefs
105	-67.02	17.91	Coral Reefs	146	-67.07	17.88	Hardbottom
106	-67.09	17.93	Hardbottom	147	-67.06	17.88	Hardbottom
107	-67.02	17.89	Mix:Sand/Hardbottom/Coral	148	-67.09	17.87	Hardbottom
108	-67.10	17.94	Mix:Sand/Hardbottom/Coral	149	-66.98	17.91	Mix:Sand/Hardbottom/Coral
109	-67.08	17.89	Coral Reefs	150	-66.97	17.91	Hardbottom
110	-67.06	17.89	Coral Reefs	151	-67.08	17.90	Seagrass
111	-67.00	17.89	Mix:Sand/Hardbottom/Coral	152	-67.13	17.89	Coral Reefs
112	-67.07	17.88	Coral Reefs	153	-67.10	17.90	Hardbottom
113	-67.13	17.86	Hardbottom	154	-67.05	17.89	Sand with Benthic Algae
114	-67.08	17.93	Coral Reefs	155	-66.97	17.90	Hardbottom
115	-67.06	17.89	Coral Reefs	156	-66.99	17.95	Coral Reefs
116	-67.11	17.94	Seagrass	157	-67.11	17.93	Coral Reefs
117	-67.09	17.93	Coral Reefs	158	-67.10	17.93	Coral Reefs
118	-67.10	17.93	Sand with Benthic Algae	159	-66.99	17.95	Coral Reefs
119	-67.07	17.89	Mix:Sand/Hardbottom/Coral	160	-67.08	17.93	Coral Reefs
120	-67.09	17.88	Mix:Sand/Hardbottom/Coral	161	-67.10	17.92	Seagrass
121	-67.01	17.91	Mix:Sand/Hardbottom/Coral	162	-67.03	17.97	Sand with Benthic Algae
122	-67.05	17.94	Coral Reefs	163	-67.11	17.92	Coral Reefs
123	-67.05	17.94	Coral Reefs	164	-67.07	17.96	Seagrass
124	-67.01	17.95	Seagrass	165	-67.08	17.96	Seagrass
125	-67.08	17.97	Seagrass	166	-67.03	17.96	Seagrass
126	-67.01	17.95	Seagrass	167	-67.03	17.97	Seagrass

168	-67.13	17.92	Coral Reefs	208	-66.98	17.96	Seagrass
169	-67.09	17.94	Seagrass	209	-66.99	17.96	Seagrass
170	-67.08	17.94	Mix:Sand/Hardbottom/Coral	210	-67.00	17.96	Seagrass
171	-67.06	17.94	Coral Reefs	211	-67.00	17.96	Mud
172	-67.08	17.93	Mix:Sand/Hardbottom/Coral	212	-67.02	17.95	Mud
173	-67.01	17.95	Seagrass	213	-67.01	17.94	Coral Reefs
174	-67.10	17.93	Coral Reefs	214	-67.08	17.89	Coral Reefs
175	-67.12	17.92	Seagrass	215	-67.06	17.89	Coral Reefs
176	-67.11	17.93	Seagrass	216	-67.00	17.91	Coral Reefs
177	-67.12	17.93	Mix:Sand/Hardbottom/Coral	217	-67.12	17.86	Coral Reefs
178	-67.05	17.95	Seagrass	218	-67.09	17.89	Coral Reefs
179	-67.10	17.92	Mix:Sand/Hardbottom/Coral	219	-67.11	17.89	Coral Reefs
180	-67.04	17.96	Hardbottom	220	-67.07	17.90	Coral Reefs
181	-67.03	17.92	Mix:Sand/Hardbottom/Coral	221	-67.03	17.88	Hardbottom
182	-67.03	17.93	Mix:Sand/Hardbottom/Coral	222	-67.05	17.90	Coral Reefs
183	-67.08	17.88	Mix:Sand/Hardbottom/Coral	223	-67.09	17.87	Mix:Sand/Hardbottom/Coral
184	-67.03	17.93	Mix:Sand/Hardbottom/Coral	224	-67.09	17.89	Coral Reefs
185	-67.04	17.92	Mix:Sand/Hardbottom/Coral	225	-67.12	17.91	Sand with Benthic Algae
186	-67.03	17.89	Mix:Sand/Hardbottom/Coral	226	-67.11	17.89	Coral Reefs
187	-67.06	17.94	Coral Reefs	227	-67.11	17.87	Hardbottom
188	-67.07	17.94	Coral Reefs	228	-67.11	17.86	Mix:Sand/Hardbottom/Coral
189	-67.07	17.92	Mix:Sand/Hardbottom/Coral	229	-67.13	17.86	Coral Reefs
190	-67.09	17.87	Sand with Benthic Algae	230	-67.13	17.91	Sand with Benthic Algae
191	-67.09	17.88	Mix:Sand/Hardbottom/Coral	231	-67.05	17.88	Hardbottom
192	-67.11	17.87	Sand with Benthic Algae	232	-67.09	17.88	Hardbottom
193	-67.13	17.87	Mix:Sand/Hardbottom/Coral	233	-66.99	17.93	Coral Reefs
194	-67.13	17.88	Coral Reefs	234	-67.10	17.88	Coral Reefs
195	-67.13	17.88	Mix:Sand/Hardbottom/Coral	235	-67.05	17.93	Coral Reefs
196	-67.13	17.88	Mix:Sand/Hardbottom/Coral	236	-67.02	17.92	Seagrass
197	-67.08	17.92	Mix:Sand/Hardbottom/Coral	237	-67.00	17.91	Seagrass
198	-67.08	17.94	Coral Reefs	238	-67.00	17.92	Sand with Benthic Algae
199	-67.12	17.92	Seagrass	239	-67.03	17.91	Coral Reefs
200	-67.12	17.92	Sand with Benthic Algae	240	-66.99	17.93	Coral Reefs
201	-67.06	17.97	Mud	241	-67.10	17.87	Coral Reefs
202	-67.06	17.96	Sand with Benthic Algae	242	-67.03	17.90	Coral Reefs
203	-67.00	17.95	Seagrass	243	-67.05	17.92	Coral Reefs
204	-67.00	17.95	Sand with Benthic Algae	244	-67.05	17.92	Coral Reefs
205	-67.00	17.95	Sand with Benthic Algae	245	-67.11	17.88	Mix:Sand/Hardbottom/Coral
206	-66.99	17.96	Seagrass	246	-67.05	17.92	Coral Reefs
207	-67.00	17.95	Seagrass	247	-66.99	17.92	Sand

248	-67.11	17.88	Coral Reefs	288	-67.11	17.94	Seagrass
249	-67.00	17.93	Sand	289	-67.01	17.93	Sand with Benthic Algae
250	-67.02	17.92	Coral Reefs	290	-67.08	17.95	Sand with Benthic Algae
251	-67.05	17.94	Sand with Benthic Algae	291	-67.10	17.95	Seagrass
252	-67.05	17.96	Sand with Benthic Algae	292	-67.07	17.97	Mud
253	-66.98	17.93	Coral Reefs	293	-67.12	17.92	Coral Reefs
254	-67.05	17.93	Sand with Benthic Algae	294	-67.11	17.94	Coral Reefs
255	-67.06	17.93	Coral Reefs	295	-66.99	17.96	Seagrass
256	-67.06	17.93	Coral Reefs	296	-67.04	17.96	Seagrass
257	-67.07	17.93	Sand with Benthic Algae	297	-66.99	17.95	Sand
258	-67.05	17.94	Sand with Benthic Algae	298	-67.01	17.94	Seagrass
259	-67.03	17.93	Seagrass	299	-67.01	17.94	Seagrass
260	-67.06	17.93	Coral Reefs	300	-67.13	17.94	Seagrass
261	-67.06	17.93	Sand	301	-67.07	17.94	Coral Reefs
262	-67.07	17.93	Seagrass	302	-67.06	17.96	Seagrass
263	-67.06	17.94	Sand	303	-67.10	17.94	Seagrass
264	-67.01	17.93	Sand	304	-67.06	17.94	Seagrass
265	-66.98	17.94	Sand	305	-67.05	17.96	Mix:Sand/Hardbottom/Coral
266	-67.02	17.94	Coral Reefs	306	-66.98	17.95	Seagrass
267	-67.04	17.94	Mix:Sand/Hardbottom/Coral	307	-67.13	17.93	Seagrass
268	-67.06	17.95	Mix:Sand/Hardbottom/Coral	308	-67.07	17.94	Coral Reefs
269	-67.10	17.89	Mix:Sand/Hardbottom/Coral	309	-67.06	17.97	Seagrass
270	-67.07	17.89	Mix:Sand/Hardbottom/Coral	310	-67.04	17.97	Seagrass
271	-67.12	17.87	Sand with Benthic Algae	311	-67.05	17.96	Seagrass
272	-67.09	17.87	Coral Reefs	312	-67.05	17.97	Seagrass
273	-67.05	17.94	Sand with Benthic Algae	313	-67.05	17.97	Seagrass
274	-67.04	17.94	Sand with Benthic Algae	314	-67.06	17.94	Mix:Sand/Hardbottom/Coral
275	-67.05	17.94	Sand with Benthic Algae	315	-67.01	17.94	Coral Reefs
276	-67.04	17.94	Sand with Benthic Algae	316	-66.99	17.97	Sand with Benthic Algae
277	-67.05	17.94	Sand with Benthic Algae	317	-66.99	17.97	Seagrass
278	-67.01	17.96	Mud	318	-67.07	17.94	Coral Reefs
279	-67.11	17.93	Coral Reefs	319	-67.07	17.94	Coral Reefs
280	-67.00	17.93	Mix:Sand/Hardbottom/Coral	320	-67.06	17.94	Seagrass
281	-67.11	17.93	Seagrass	321	-67.06	17.94	Seagrass
282	-66.99	17.90	Hardbottom	322	-67.04	17.97	Seagrass
283	-67.11	17.93	Seagrass	323	-67.02	17.97	Mud
284	-67.04	17.96	Seagrass	324	-67.03	17.97	Seagrass
285	-67.07	17.97	Seagrass	325	-67.02	17.97	Sand with Benthic Algae
286	-67.06	17.97	Seagrass				
287	-67.08	17.95	Seagrass				